

Copyright
by
Hernan Javier Quevedo
2006

The Dissertation Committee for Hernan Javier Quevedo
certifies that this is the approved version of the following dissertation:

**Rotating Mirror Plasmas in the quest of
Magnetofluid States**

Committee:

Roger D. Bengtson, Supervisor

Swadesh M. Mahajan, Supervisor

Prashant M. Valanju

Richard D. Hazeltine

Kenneth W. Gentle

Pawan Kumar

**Rotating Mirror Plasmas in the quest of
Magnetofluid States**

by

Hernan Javier Quevedo, B.S.

DISSERTATION

Presented to the Faculty of the Graduate School of
The University of Texas at Austin
in Partial Fulfillment
of the Requirements
for the Degree of

DOCTOR OF PHILOSOPHY

THE UNIVERSITY OF TEXAS AT AUSTIN

August 2006

Dedicated to my daughter Veronika and my wife Valeria.

Acknowledgments

I would like to thank my supervisor Roger Bengtson who directed my work all these years. He has always made me focus on the big picture and encouraged me enormously to finish writing this dissertation. I would also like to express my gratitude to Prashant Valanju for our long discussions on the theoretical side of the experiment and his teachings on how to simplify problems. Many thanks to Keith Carter for his help building, and repairing the machine all these years. I am also grateful to Swadesh Mahajan for our discussions on the theory of Magnetofluid States and to Richard Hazeltine for his contribution in Rotating Mirror Plasmas. I also want to thank James Wiley for his help in Linux related issues and Perry Phillips for the hand provided in setting up the archive system.

The laboratory has always been a friendly place to work thanks to the good lab mates I have had. In particular, I want to thank Martin Panevsky for all the good talks and fun moments shared, and Charles Lee and Ella Sciamma for their friendship in these last years. My gratitude goes also to Rainer Hörlein and Jeremy Murphy for their contribution to the experiment and good humor.

I would like to thank deeply my parents Susana and Miguel and my sister Mariana who have been always supporting my work despite the distance

that separate us. And last but not least, I want to thank the two women in my life, my wife Valeria for sharing and supporting every single day of the week, and my daughter Veronika for enriching my life in the past two years and let me sleep during those nights.

Rotating Mirror Plasmas in the quest of Magnetofluid States

Publication No. _____

Hernan Javier Quevedo, Ph.D.
The University of Texas at Austin, 2006

Supervisors: Roger D. Bengtson
Swadesh M. Mahajan

The goal of this dissertation is to describe and discuss the first steps taken by the Magneto Bernoulli eXperiment (MBX) to create magnetofluid states in the laboratory using a rotating plasma in an external mirror magnetic field. The terminology magnetofluid has been introduced to characterize a plasma model, based on 2-fluid theory, that treats the flow and the magnetic field in a symmetrical way. Many interesting astrophysical and laboratory problems involve large flows and fall in this category.

Based on the set of parameters where MBX should run, we set up the experiment, and added different probes to diagnose the rotating plasma. We have also installed a data acquisition system, and set up an archive system (to store the data) that can be accessed worldwide.

Experimental results demonstrate that supersonic flows can be generated with biasing electrodes at the throat of the mirror magnetic field. Alfvénic

flows needed for a transition to magnetofluid states could not be reached because the initial plasma density was too low. At low bias (slow rotational speed) the plasma has $\mathbf{E} \times \mathbf{B}/B^2$ drift rotation and the magnetic fields lines are equipotentials. With a higher bias, we observed large potential drops along the field lines. We also observed an asymmetry in the polarity of the bias which leads to constraints in the control of the sheared plasma flow. We present a model that captures many of these features.

In conjunction with experimental efforts we develop a theory for a rotating plasma embedded in an external mirror magnetic field. An analytic solution that involves rigid rotation of the plasma shows important differences between a 2-fluid system and ideal MHD. We find high non equipotential magnetic lines and asymmetry to compare with the experimental results.

Table of Contents

Acknowledgments	v
Abstract	vii
List of Tables	xi
List of Figures	xii
Chapter 1. Introduction	1
Chapter 2. Theory	7
2.1 Model	8
2.1.1 Basic Equations	8
2.1.2 Dimensionless Form	9
2.1.3 Assumptions	12
2.1.4 Simplified Equations	14
2.1.5 Plasma Parameters	15
2.2 Dissipationless Electron-Ion equations	17
2.2.1 Validity Region	20
2.2.2 Magnetofluid States	22
2.2.3 Externally Driven Rotating Plasma Solutions	30
2.3 Dissipation equations	47
Chapter 3. Experimental Setup	54
3.1 Vacuum Chamber	55
3.2 Gas	58
3.3 Magnetic Field	60
3.4 Microwaves	64
3.5 Electric Field	69

Chapter 4. Plasma Measurements	75
4.1 Diagnostics	76
4.1.1 Langmuir/Mach Probe	76
4.1.2 Floating Probes	86
4.1.3 Camera	90
4.1.4 Biasing Electrodes	91
4.2 Signal Conditioning	92
4.3 Data Acquisition	92
4.4 Data Archiving	97
Chapter 5. Experimental Results	100
5.1 Target Plasma	100
5.2 Plasma Speed and Electric Drift	107
5.3 Electrode Configurations	110
5.4 Current Asymmetry	118
5.5 Throat Potential Asymmetry	122
5.6 Asymmetry Model	126
5.7 Potential at the Equatorial Plane and Centrifugal Confinement	131
5.8 Ionization	137
Chapter 6. Summary	141
Bibliography	145
Vita	152

List of Tables

2.1	Typical parameters, associated frequencies and corresponding substitutions to normalize the set of equations in Section 2.1.1.	10
2.2	Dimensionless coefficients.	11
2.3	Typical plasma parameters for the present and future conditions in MBX as well as for MCX [7, 12].	16
4.1	Main characteristics of the National Instruments acquisition boards used to digitize the signals.	93

List of Figures

1.1	Initial plasma confinement and rotation.	3
1.2	Centrifugal forces provide significant axial confinement.	4
1.3	Possible relaxation process to a nearby axially detached magnetofluid state.	5
2.1	Region in parameter space where dissipationless equations apply and strongly coupled magnetofluid states can exist.	21
2.2	1-D cylindrical solution for a double curl Beltrami system.	28
2.3	Decoupling of the fields representing a rotating plasma in a poloidal magnetic field.	31
2.4	Rigid rotation solution for $E_r > 0$ at the mirror throat and present conditions in MBX.	40
2.5	Rigid rotation solution for $E_r < 0$ at the mirror throat and present conditions in MBX.	41
2.6	Asymmetry in the penetration of the electric potential from the throat to the equatorial plane.	42
2.7	Rigid rotation solution for $E_r > 0$ at the mirror throat and future conditions in MBX.	44
2.8	Rigid rotation solution for $E_r > 0$ and $\epsilon \sim 1$, $M_A \sim 1$	45
2.9	Cylindrical solution for a rotating plasma with dissipation in MBX present conditions.	50
2.10	Cylindrical solution for a rotating plasma with dissipation in MBX future conditions.	53
3.1	Steps followed to create a supersonic rotating plasma.	54
3.2	Vacuum chamber dimensions, symmetric around the z axis.	56
3.3	Vacuum pump system diagram.	57
3.4	Schematic of the gas injection system.	59
3.5	Mirror magnetic field configuration.	62
3.6	Fluctuations in the plasma due to microwaves power ripple.	66
3.7	Schematic of the microwave power system.	67

3.8	Schematic of the $\frac{\mathbf{E} \times \mathbf{B}}{B^2}$ mechanism to rotate plasma.	70
3.9	Schematic of one type of electrode configuration.	71
3.10	Comparison of aluminum and stainless steel electrodes.	73
3.11	Different electrode configurations used in MBX.	74
4.1	Steps followed to characterize the state of the plasma.	75
4.2	Typical Langmuir probe $I - V_0$ characteristic curve for non rotating MBX plasma.	79
4.3	Typical Mach probe $I - V_0$ characteristic curve for rotating MBX plasma.	80
4.4	Schematic of Langmuir/Mach probe biasing system.	82
4.5	Langmuir/Mach probe head.	83
4.6	Hysteresis in the Langmuir probe measurements as the sweeping frequency is increased.	84
4.7	Positions of the floating probes.	88
4.8	Loading effect of the plasma due to different input impedances used at the floating probes.	89
4.9	Qualitative features captured with the mounted camera.	91
4.10	Screenshot of part of the control panel written in Labview.	94
4.11	“Wire code“ that runs behind Labview interfaces.	95
4.12	Sequence used by the code written in Labview to control the experiment, acquire data and transfer it to an archive server.	96
4.13	MDSplus tree showing its hierarchical structure.	98
4.14	Scope application to easily view the data stored in an MDSplus shot locally or remotely.	99
5.1	Density radial scan at the midplane for different magnetic field intensities and neutral pressures.	102
5.2	Temperature radial scan at the midplane for different magnetic field intensities and neutral pressures.	105
5.3	Difference in density profiles measured by the Langmuir probe facing the plasma source (Lang_A) and the electrodes (Lang_B).	106
5.4	Velocity measured with the Mach probe compared to the electric drift V_E	108
5.5	Non rotating plasma density profile affected by the rotation.	110

5.6	Potential measured at the equatorial plane for the center rod electrode.	112
5.7	Comparison of the penetration of the potential when the electrodes or the limiter are used as the return path.	114
5.8	Ability to control the potential profile.	115
5.9	Potential measured at the equatorial plane for the plate and ring electrodes biased at ± 400 V.	117
5.10	Asymmetry in the inner ring electrode current as function of the potential applied to it.	119
5.11	Asymmetry but no saturation of the current.	120
5.12	Asymmetry in the current collected by two biased rings. . . .	121
5.13	Asymmetry in the plasma potential facing the biased inner ring electrode as a function of its potential.	123
5.14	Asymmetry in the potential that penetrates the plasma biasing two rings.	125
5.15	Diagram to model the plasma bulk, sheaths and electrodes. . .	126
5.16	Asymmetry in current and floating potentials <i>vs.</i> applied electrode voltage described by the model.	128
5.17	Operating points for different applied potentials.	130
5.18	Floating potential measured at the equatorial plane and the mirror throat for low positive voltage on the electrodes. . . .	132
5.19	Floating potential measured at the equatorial plane and the mirror throat for high positive voltage on the electrodes. . . .	134
5.20	Floating potential measured at the equatorial plane and the mirror throat for negative voltage on the electrodes.	135
5.21	High speed rotation but no extra ionization.	140

Chapter 1

Introduction

This dissertation covers the first steps taken by the Magneto Bernoulli eXperiment (MBX) to create magnetofluid states in the lab using a rotating plasma in an external mirror magnetic field. The terminology magnetofluid has been introduced to characterize a plasma model, based on 2-fluid theory, that treats the flow and the magnetic field in a symmetrical way. The goal of the dissertation is to show the experimental work done in the methodology chosen to create such states in the lab and to contribute in the theoretical understanding of the importance of 2-fluid effects applied to rotating plasmas in connection with magnetofluid states.

The motivation to create magnetofluid states is based on a number of interesting and unsolved problems in nature as well as in the laboratory environment that involve large plasma flows. One of the best known astrophysical examples is the heating of the solar corona, possibly mediated by the interaction of sub coronal flows with the coronal magnetic field [37]. The increase in plasma confinement when a tokamak plasma makes a transition from a low confinement mode to a high confinement mode (H-mode) is a particularly interesting laboratory phenomena. At the transition to H-mode a highly sheared

flow appears in the region of steep density gradients [45]. Other characteristics that these unexplained problems have in common, apart from high plasma flows, are: 1) good confinement, 2) no requirement of high symmetry, and 3) existence of multiple intrinsic scale lengths. Despite considerable effort there is not a general understanding of confinement and flows.

In order to study the structures in plasmas with high speed flows strongly coupled to the magnetic field, the recent theory of magnetofluid states (MFS) introduced by Mahajan and Yoshida [27] provides a new theoretical framework. This theory has been applied both to the solar corona and to the H-mode transitions. In the first case, magnetofluid equilibria allows, for example, the existence of a smooth magnetic field with a highly varying velocity field; the latter can enhance the viscous dissipation leading to heating and sustainment of the solar corona [26]. When applied to the H-mode, the theory predicts the possible emergence of a singular layer (after a self organization process) on the ion skin depth scale length endowed with high shear flows and a strong drop in pressure for high confinement [28].

A variety of interesting features of magnetofluid states have not been observed in the lab, primarily because of difficulties in creating fast magnetized plasma flows (of the order of the Alfvén speed V_A) in the laboratory environment. The Magneto Bernoulli eXperiment (MBX) [4] was designed to explore possible paths to magnetofluid states. The main idea is to create an initial rotation by applying a radial electric field to a magnetized plasma [24] that can relax to a magnetofluid state in which the final configuration depends

only on the initial values of the two conserved helicities. The proposed path to obtain magnetofluids is the following. The initial confinement in the parallel direction is obtained by embedding the plasma in an axisymmetric magnetic mirror configuration (Fig. 1.1 - left hand side). Concentric rings located at

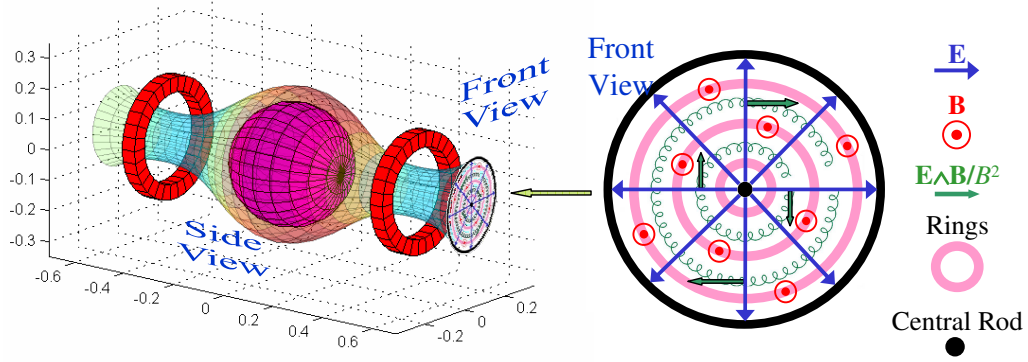


Figure 1.1: Initial plasma confinement in a magnetic mirror field (left hand side) where concentric rings at the throat bias the plasma to create an azimuthal rotation (right hand side).

one throat of the mirror, biased with respect to a limiter and grounded walls, set up a radial electric field \mathbf{E} that, in combination with the magnetic field \mathbf{B} , creates an azimuthal electric drift $\mathbf{V}_E = \mathbf{E} \times \mathbf{B} / B^2$ (Fig. 1.1 - right hand side) [1, 3, 24]. The rotational flow in combination with the mirror field, creates an inertial (centrifugal) force parallel to \mathbf{B} that acts mostly on the ions and pushes the plasma towards the equatorial plane providing significant axial confinement (Fig. 1.2 - left hand side) [8, 9, 24]. This effect tends to reduce the usual loss cone in mirror machines everywhere except on the axis of symmetry; a spatial loss cone and consequently a toroidal plasma ring gets created

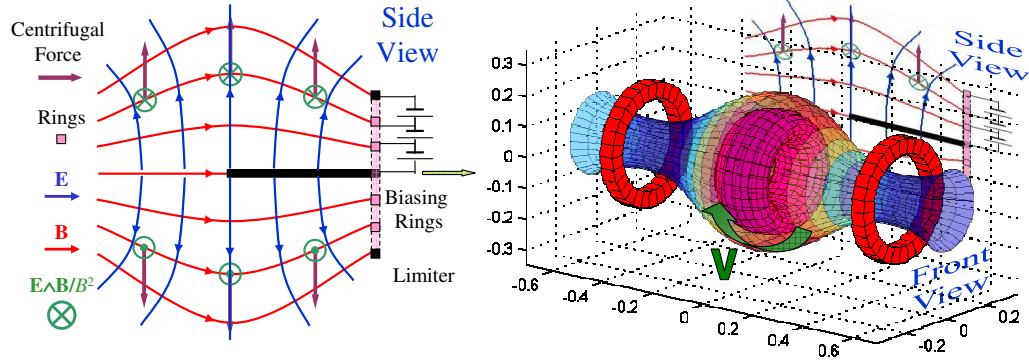


Figure 1.2: Centrifugal forces due to plasma rotation provide significant axial confinement (left hand side). The absence of centrifugal force at the axis creates an spatial loss cone and a plasma ring (right hand side).

(Fig. 1.2 - right hand side) [16]. The radial centrifugal force causes the ions to have an extra drift resulting in a diamagnetic current \mathbf{J}_d (and also a self magnetic field) (Fig. 1.3 - left hand side) [9]. When the rotation is fast enough the self magnetic field can strongly couple with the external one. The weakest point in this configuration is at the inner equator where the total magnetic field is weakest. We expect the plasma to evolve from this confinement by using the free energy in the flow with a reconnection in the magnetic field to form a toroid, and then relax through a turbulent process to a nearby axially detached magnetofluid state (Fig. 1.3 - right hand side) [4]. The final state will only depend on the initial values of the two helicity invariants set by the initial flows and currents independent of the details of the turbulent process of field line breaking and rejoining. We can also assist this formation inducing poloidal seed currents.

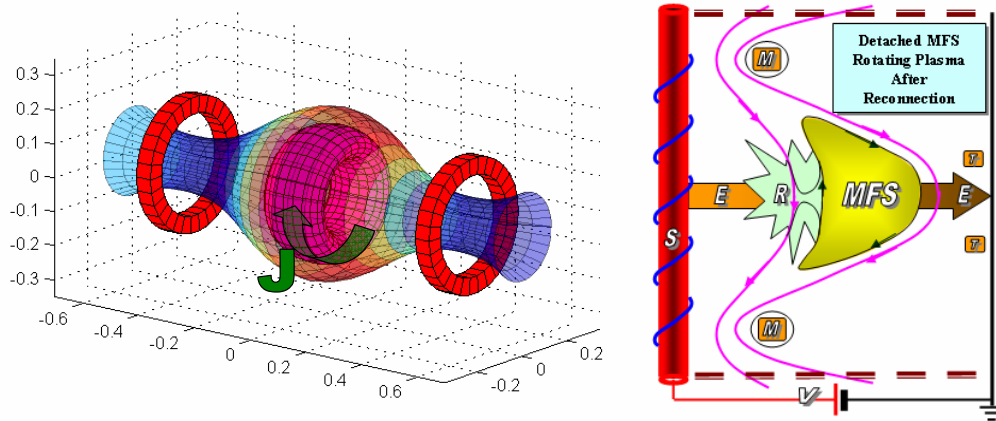


Figure 1.3: The radial centrifugal force causes the ions to have an extra drift creating a diamagnetic current \mathbf{J}_d and a self magnetic field (left hand side) where the plasma could probably relax to a nearby axially detached magnetofluid state (right hand side).

This work is divided in 6 chapters. The second chapter contains a review of the theory of magnetofluids and its most important features. We also add a theoretical study of rotating plasmas that compares the predictions of a two fluid model with those of ideal magnetohydrodynamics (MHD). This treatment is also relevant to the Maryland Centrifugal eXperiment (MCX) [8]. We retain dissipative terms that allow the understanding of the external inputs such as currents, needed to drive the system in the present configuration and the possible requirements for magnetofluid states.

The third chapter explains in detail the experimental set up that follows the proposed path into magnetofluids. Details about the generation of the

external mirror field, the initial plasma creation as well as the plasma biasing scheme used to achieve fast, supersonic rotation, are also given.

In Chapter four, are described the diagnostics used to measure different plasma properties of the rotating plasma: the plasma density, temperature, potential and rotational velocity. The set up for signal conditioning, data acquisition and archiving is also presented.

In Chapter 5, the experimental progress towards creating magnetofluid states is discussed. We find that supersonic low density plasmas can be achieved using the present technique, but some details have to be taken into consideration. To reach Alfvenic speeds and possible magnetofluid states the density has to increase by two orders of magnitude from its present value.

Based on the experience gained from this investigation, we propose in the sixth and final chapter possible directions to be taken in the quest of magnetofluid states.

Chapter 2

Theory

The main purpose of the Magneto Bernoulli eXperiment is to achieve magnetofluids states in the lab. MBX plans to reach these states in an external mirror magnetic field. While we have not reached the conditions needed for magnetofluid states to exist, we have made significant progress in understanding the conditions for creating them. In this chapter then, we review the magnetofluid state formalism and some of the characteristics that make them distinct. We also present some characteristics of the proposed path and compare them to ideal MHD conditions where previous and present rotating plasma experiments have operated. Finally, we investigate the role that dissipation plays in the present system, and compare the findings to the experimental results.

In order to reach a system of equations to study all the points mentioned previously we analyze a two fluid system. We start with the first 2 moments of the fluid equations including dissipative terms combined with Maxwell's equations. We write the system in dimensionless form to analyze the contribution of each term so that simplifications can be made and to find a region in parameter space where the dissipationless set is valid. Typical plasma pa-

rameters for MBX present and future conditions are shown and compared to MCX. We then present the dissipationless system, both in connection with magnetofluid states as well as with rotating plasmas in an external mirror magnetic field. Finally we study the set of equations keeping the dissipative terms in a simple cylindrical geometry to understand our present and future external requirements.

2.1 Model

2.1.1 Basic Equations

The study starts by considering a plasma containing electrons (e), single ionized atoms (i), and neutrals (n). To simplify the system we take only the first two moments of the kinetic equations for the charged particles ($s = e, i$) and combine them with Maxwell's equations to obtain the following set of equations [17]

$$\frac{\partial n_s}{\partial t} = -\nabla \cdot (n_s \mathbf{V}_s) + I_{s0} \quad (2.1)$$

$$m_s n_s \frac{d\mathbf{V}_s}{dt} = e_s n_s (\mathbf{E} + \mathbf{V}_s \times \mathbf{B}) - \nabla p_s - \nabla \cdot \mathbf{\Pi}_s + \mathbf{F}_{sj} - m_s I_{s0} \mathbf{V}_s \quad (2.2)$$

$$\nabla \times \mathbf{B} = \mu_0 \mathbf{J} + \frac{1}{c^2} \frac{\partial \mathbf{E}}{\partial t} \quad (2.3)$$

$$\nabla \cdot \mathbf{B} = 0 \quad (2.4)$$

$$\nabla \times \mathbf{E} = -\frac{\partial \mathbf{B}}{\partial t} \quad (2.5)$$

$$\nabla \cdot \mathbf{E} = \frac{e(n_i - n_e)}{\epsilon_0} \quad (2.6)$$

$$\mathbf{J} = e(n_i \mathbf{V}_i - n_e \mathbf{V}_e) \quad (2.7)$$

The particle equation (2.1) contains the density n_s , velocity \mathbf{V}_s , and a possible source function $I_{s0} = i_{s0} = \int I_s d^3v$. The momentum equation (2.2) contains the inertia and Lorentz force, the pressure tensor $\mathbf{p} = p_s \mathbf{I} + \mathbf{\Pi}_s$, frictional forces \mathbf{F}_{sj} (with $j = e, i, n$), and a drag force from the possible source term $\mathbf{i}_{s1} = -I_{s0} \mathbf{V} + \int \mathbf{v} I_s d^3v = -I_{s0} \mathbf{V}$ assuming that I_s is isotropic in the velocity space. I_{s0} can be approximated as the particle density multiplied by an ionization frequency $I_{s0} \sim n_s \nu_{ion,s}$.

Friction between electrons and ions or neutrals can be included. First order expressions are given by

$$\mathbf{F}_{ie} = -M n_i \nu_{ie} (\mathbf{V}_i - \mathbf{V}_e) = -M n_i \nu_{ie} \Delta \mathbf{V}_{ie} = -\mathbf{F}_{ei}$$

$$\mathbf{F}_{sn} = -m_s n_s \nu_{sn} (\mathbf{V}_s - \mathbf{V}_n) = -m_s n_s \nu_{sn} \Delta \mathbf{V}_{sn}$$

where ν_{sj} is the collision frequency of specie s against specie j and $M(m)$ is the ion (electron) mass.

The viscosity tensor can be written as $\mathbf{\Pi}_s = -\bar{\bar{\mu}}_s \cdot \mathbf{W}_s$ where $\bar{\bar{\mu}}_s$ is a 3×3 tensor and $W_{jk} = \frac{\partial V_j}{\partial x_k} + \frac{\partial V_k}{\partial x_j} - \frac{2}{3} \delta_{jk} \nabla \cdot \mathbf{V}$, $[\mathbf{W}_s] = \text{Hz}$ [5]. The kinematic viscosity is defined as $\nu_{k,s} = \mu_s / (m_s n_s)$.

2.1.2 Dimensionless Form

We normalize the previous set of equations keeping in mind that the velocity of the fluid is one of the most important quantities in our experiment. Table 2.1 contains the dimensions used or defined and the corresponding

substitutions where tilde represents typical parameters (\tilde{V} -velocity, \tilde{L} -length, \tilde{B} -magnetic field, \tilde{n} -density, \tilde{T} -temperature).

DIMENSIONS	FREQUENCIES	SUBSTITUTIONS
$\tilde{V}, \tilde{L}, \tilde{B}, \tilde{n}, \tilde{T}$ $M = m_i, m = m_e$ $V_A = \frac{B}{\sqrt{\mu_0 n_i M}}, \text{ Alfvén speed}$ $v_{th,s} = \sqrt{\frac{T_s}{m_s}}, \text{ thermal speed}$ $C_s, \text{ sound speed}$ $\lambda_s = \frac{c}{\omega_{p,s}} = \sqrt{\frac{M}{m_s}} \frac{V_A}{\Omega_s}, \text{ skin depth}$ $\sigma = \eta_e^{-1} = \frac{n_e e^2}{\nu_{ei} m}, \text{ conductivity}$	$\tilde{\omega} = \frac{\tilde{V}}{\tilde{L}}, \text{ inertia}$ $\Omega_s = \frac{q_s B}{m_s}, \text{ cyclotron}$ $\omega_{t,s} = \frac{\tilde{v}_{th,s}}{\tilde{L}}, \text{ transit}$ $\nu_{ij}, \text{ collisional } (i \rightarrow j)$ $\nu_{ion,s}, \text{ ionization}$ $\omega_{p,s} = \sqrt{\frac{n_s e^2}{\epsilon_0 m_s}}, \text{ plasma}$	$\nabla \rightarrow \frac{1}{\tilde{L}} \nabla$ $\mathbf{V}_s \rightarrow \tilde{V} \mathbf{V}_s$ $\mathbf{B} \rightarrow \tilde{B} \mathbf{B}$ $\mathbf{E} \rightarrow \tilde{V} \tilde{B} \mathbf{E}$ $p_s \rightarrow \tilde{n} \tilde{T} p_s$ $n_s \rightarrow \tilde{n} n_s$ $\mathbf{J} \rightarrow e \tilde{n} \tilde{V} \mathbf{J}$ $\mu_s \mathbf{W}_s \rightarrow \tilde{\mu}_s \tilde{\omega} \mu_s \mathbf{W}_s$ $S_s \rightarrow \tilde{n} \tilde{\nu}_{ion,s} n_s \nu_{ion,s}$

Table 2.1: Typical parameters, associated frequencies and corresponding substitutions to normalize the set of equations in Section 2.1.1.

Combining the different parameters in the system leads to the set of dimensionless quantities in Table 2.2. These quantities express the importance between the different terms in the equations. After making all the corresponding substitutions in Table 2.1 and using the dimensionless coefficient in Table 2.2 the dimensionless form of the system of equations in Section 2.1.1 becomes

DIMENSIONLESS
$M_A = \left(\frac{\tilde{V}}{V_A} \right), \text{ Alfvén Mach Number}$ $M = \left(\frac{\tilde{V}}{c_s} \right), \text{ Mach Number}$ $M_s = \left(\frac{\tilde{V}}{\tilde{v}_{th,s}} \right)$ $C_{H,s} = \left(\frac{\tilde{\Omega}_s}{\tilde{\nu}_{ss}} \right), \text{ Hall Coefficient}$ $\beta = \frac{\tilde{n}\tilde{T}}{\tilde{B}^2/(2\mu_0)} = 2 \left(\frac{\tilde{v}_{th,i}}{V_A} \right)^2 = 2 \left(\frac{M_A}{M_i} \right)^2, \text{ Beta}$ $\epsilon_s = \left(\frac{\tilde{w}}{\tilde{\Omega}_s} \right) = \sqrt{\frac{m_s}{M}} \frac{\tilde{\lambda}_s}{L} \frac{\tilde{V}}{V_A} = \frac{1}{C_{H,s}C_{D,ss}}$ $\epsilon = \left(\frac{\tilde{w}}{\tilde{\Omega}_i} \right) = \frac{\tilde{\lambda}_i}{L} \frac{\tilde{V}}{V_A} = \frac{1}{C_{H,i}C_{D,ii}}$ $C_{D,is} = \left(\frac{\tilde{\nu}_{is}}{\tilde{w}} \right), \text{ Drag Coefficient}$ $R_{e,s} = \left(\frac{\tilde{L}\tilde{V}}{\tilde{\nu}_{k,s}} \right), \text{ Reynolds Number}$

Table 2.2: Dimensionless coefficients.

$$\begin{aligned}
\frac{\partial n_s}{\partial t} &= -\nabla \cdot (n_s \mathbf{V}_s) + \frac{\tilde{\nu}_{ion,s}}{\tilde{w}} \nu_{ion,s} n_s \\
\frac{d\mathbf{V}_s}{dt} &= \frac{(\mathbf{E} + \mathbf{V}_s \times \mathbf{B})}{\epsilon_s} - \frac{\nabla p_s / n_s}{M_s^2} + \\
&\quad - \frac{\nu_{k,s} \nabla \cdot \mathbf{W}_s}{R_{e,s}} - C_{D,sj} \nu_{sj} \Delta \mathbf{V}_{sj} - \frac{\tilde{\nu}_{ion,s}}{\tilde{w}} \nu_{ion,s} \mathbf{V}_s \\
\nabla \times \mathbf{B} &= \frac{M_A^2}{\epsilon} \mathbf{J} + \left(\frac{V_0}{c} \right)^2 \frac{\partial \mathbf{E}}{\partial t} \\
\nabla \cdot \mathbf{B} &= 0 \\
\nabla \times \mathbf{E} &= -\frac{\partial \mathbf{B}}{\partial t} \\
(n_i - n_e) &= \delta n = \left(\frac{V_A}{c} \right)^2 \epsilon \nabla \cdot \mathbf{E} \\
\mathbf{J} &= n_i \mathbf{V}_i - n_e \mathbf{V}_e
\end{aligned}$$

All quantities are dimensionless including the frequencies that are normalized to their average values. It can be seen that ϵ_s is the measure of the mass-charge ratio. It appears when electromagnetic and inertial forces are compared. Moreover, while ϵ is assumed to vanish in the ideal MHD closure, it is of the order of unity when the interaction between velocity and magnetic fields in magnetofluids is strongest. It is important to notice the choice made for \mathbf{J} . It is normalized to the plasma velocities, rather than the currents creating \tilde{B} which could be external. Usually perpendicular currents that arise from inertial effects (electric drift does not contribute) are of order ϵ so that the self field generated is of order M_A^2 . This field will be comparable to the external field when Alfvén speeds are reached, point where we expect a reconnection process might take place.

2.1.3 Assumptions

A list of considerations convenient for simplifying the theory, apart from the ones already made for the source and friction forces, follows:

1. Negligible displacement current $\frac{\partial \mathbf{E}}{\partial t}$ because $\left(\frac{c}{V_A}\right)^2 \gg \epsilon$.
2. Quasineutrality: $n = n_i = n_e + \delta n$, with $\delta n \ll n$, since $\epsilon \left(\frac{V_A}{c}\right)^2 \ll 1$.
Sheath effects are treated separately, at the plasma-wall boundary.
3. The inertia of the electrons is neglected compared to the inertia of the ions, $\epsilon_e = \frac{m}{M}\epsilon_i$.
4. $\mathbf{J} \sim n(\mathbf{V}_i - \mathbf{V}_e)$, and $\mathbf{V}_i \sim \mathbf{V}$ ($\frac{m}{M} \ll 1$) so that $\mathbf{V}_e \sim \mathbf{V} - \mathbf{J}/n$.

5. Both pressure terms p_e and p_i are similar because $\frac{\epsilon_e}{M_e^2} \sim \frac{\epsilon_i}{M_i^2}$.
6. To close the system, we can choose a barotropic pressure, $p(n)$, so that $\frac{\nabla p(n)}{n} \equiv \nabla \tilde{p}(n)$. In particular, if the system is isothermal then $\tilde{p} = \ln(n)$, and if has constant density then $\tilde{p} = T$. This assumption simplifies the equations to solve.
7. The cross section of charged particles against neutrals is similar so that $\frac{\nu_{in}}{\nu_{en}} \sim \frac{v_{th,i}}{v_{th,e}}$, then the friction force of the electrons with neutrals can be neglected compared to the ions with neutrals, $\frac{\epsilon_e C_{D,en}}{\epsilon_i C_{D,in}} \sim \sqrt{\frac{m}{M}}$ [5].
8. Since $I_i = I_e$ or $\nu_{ion,i} = \nu_{ion,e} = \nu_{ion}$, the electron source momentum term can be neglected compared to the ion momentum by a factor $\frac{\epsilon_e}{\epsilon_i} \sim \frac{m}{M}$.
9. Motionless neutrals, $\mathbf{V}_n \sim 0$, in the calculation of the drag force. In MBX present conditions of a weakly ionized plasma the density of the motionless neutral background is much higher than the density of charge exchanged neutrals. In the future the mean free path of the neutrals has to be longer than the size of the machine for this assumption to hold.
10. Electron viscosity is neglected compared to the ion viscosity since $\frac{\epsilon_e}{R_{e,e}} \sim \sqrt{\frac{m}{M}} \frac{\epsilon_i}{R_{e,i}}$. Moreover, if $\Omega_i \tau_{ii} \ll 1$ only the first term in the viscosity tensor is relevant so that $\bar{\mu}_i \sim \mu_i^0 \delta_{ij}$ with $\mu_i^0 = .96 n_i \tau_{ii} T_i$ [5].
11. When the collisional frequency among electrons and ions or between ions themselves have the form $\nu_{ei}/n = f_e(T_e, \ln \Lambda)$, $\nu_{ii}/n = f_i(T_i, \ln \Lambda)$ respectively [5], η_e and μ_i^0 simplify becoming only functions of T and

$\ln \Lambda$ (Coulomb logarithm). We define $f(T, \ln \Lambda) = (\ln \Lambda)/T^{3/2}$, all dimensionless quantities.

2.1.4 Simplified Equations

These assumptions simplify the basic equations to

$$\frac{\partial n}{\partial t} = -\nabla \cdot (n \mathbf{V}) + \frac{\tilde{\nu}_{ion}}{\tilde{w}} \nu_{ion} n, \text{ for both } e, i \quad (2.8)$$

$$\begin{aligned} \frac{d\mathbf{V}}{dt} = & \frac{(\mathbf{E} + \mathbf{V} \times \mathbf{B})}{\epsilon} - \frac{1}{M_i^2} \frac{\nabla p_i}{n} - C_{D,ie} f(T, \ln \Lambda) \mathbf{J} + \\ & -\nu_{k,i} \frac{\nabla \cdot \mathbf{W}_i}{R_{e,i}} - \left(C_{D,in} \nu_{in} + \frac{\tilde{\nu}_{ion}}{\tilde{w}} \nu_{ion} \right) \mathbf{V} \end{aligned} \quad (2.9)$$

$$0 = -\frac{(\mathbf{E} + \mathbf{V}_e \times \mathbf{B})}{\epsilon} - \frac{1}{M_i^2} \frac{\nabla p_e}{n} + C_{D,ie} f(T, \ln \Lambda) \mathbf{J} \quad (2.10)$$

$$\frac{\partial \delta n}{\partial t} = -\nabla \cdot \mathbf{J} \sim 0 \quad (2.11)$$

$$\begin{aligned} \frac{d\mathbf{V}}{dt} = & \epsilon^{-1} \frac{\mathbf{J} \times \mathbf{B}}{n} - \frac{1}{M_i^2} \frac{\nabla p}{n} + \\ & -\nu_{k,i} \frac{\nabla \cdot \mathbf{W}_i}{R_{e,i}} - \left(C_{D,in} \nu_{in} + \frac{\tilde{\nu}_{ion}}{\tilde{w}} \nu_{ion} \right) \mathbf{V} \end{aligned} \quad (2.12)$$

$$\mathbf{E} + \mathbf{V} \times \mathbf{B} = -\frac{\epsilon}{M_i^2} \frac{\nabla p_e}{n} + \frac{\mathbf{J} \times \mathbf{B}}{n} + f(T, \ln \Lambda) \frac{\mathbf{J}}{C_{H,e}} \quad (2.13)$$

$$\nabla \times \mathbf{B} = \frac{M_A^2}{\epsilon} \mathbf{J} \quad (2.14)$$

$$\nabla \cdot \mathbf{B} = 0 \quad (2.15)$$

$$\nabla \times \mathbf{E} = -\frac{\partial \mathbf{B}}{\partial t} \quad (2.16)$$

$$\delta n = \left(\frac{V_{A,0}}{c} \right)^2 \epsilon \nabla \cdot \mathbf{E} \quad (2.17)$$

$$\mathbf{J} = n(\mathbf{V}_i - \mathbf{V}_e) \quad (2.18)$$

where $p = p_e + p_i$ is the total pressure and the terms in blue are used in the dissipationless theory of magnetofluid states. The set of equations corresponds to a compressible, resistive, viscous, Hall MHD.

2.1.5 Plasma Parameters

We use two different sets of plasma parameters. The first choice corresponds to the present conditions in MBX where the plasma density is low and the speed, even though supersonic, is sub-Alfvénic. The future corresponds to higher densities where magnetofluid states can exist. Table 2.3 shows both regimens as well as MCX parameters.

Presently in MBX the inertial effects are small but not negligible ($\epsilon = 0.025$) while in the future we aim to have a strong coupling between flows and the electromagnetic field ($\epsilon = 0.25$). The Alfvén Mach number in combination with ϵ yields a self magnetic field four orders of magnitude less than the external field in the present conditions while we expect to be at par (~ 0.25) in the future so that a reconnection process becomes possible. The low β presently implies that the pressure is much smaller than the magnetic pressure but at par in future conditions. The Hall coefficient is large in all cases so that the resistance arising from electron-ion collisions is small compared to the Hall term. Also, the leading term in the viscosity is much larger than the following orders as assumed in section 2.1.3. The neutral drag coefficient is presently small and we expect to be smaller as highly ionized plasmas are obtained in the future. The Reynolds number is on the order of unity which

Parameter	Units	MBX Present	MBX Future	MCX
\tilde{B}	T	0.04	0.02	0.2
\tilde{L}	m	0.25	0.25	0.25
\tilde{V}	m/s	$2.5 \cdot 10^4$	10^5	$2.5 \cdot 10^5$
\tilde{n}	particles/m ³	10^{16}	$5 \cdot 10^{18}$	$5 \cdot 10^{20}$
\tilde{n}_N	particles/m ³	$2.5 \cdot 10^{18}$	$< 2.5 \cdot 10^{18}$	$< 2.5 \cdot 10^{20}$
\tilde{T}_e	eV	5	10	15
\tilde{T}_i	eV	1	10	15
$\tilde{v}_{th,i}$	m/s	$9.8 \cdot 10^4$	$3.1 \cdot 10^4$	$3.8 \cdot 10^4$
\tilde{V}_A	m/s	$8.7 \cdot 10^6$	$2 \cdot 10^5$	$2.0 \cdot 10^5$
$\tilde{\Omega}_i$	rad/s	$3.8 \cdot 10^6$	$1.9 \cdot 10^6$	$1.9 \cdot 10^7$
$\tilde{\omega}$	Hz	$1.0 \cdot 10^5$	$4.0 \cdot 10^5$	$1.0 \cdot 10^6$
$\tilde{\omega}_t$	Hz	$3.9 \cdot 10^4$	$1.2 \cdot 10^5$	$1.5 \cdot 10^5$
$\tilde{\nu}_{ei}$	Hz	$3.6 \cdot 10^4$	$5.6 \cdot 10^6$	$2.6 \cdot 10^8$
$\tilde{\nu}_{cx}$	Hz	$2.5 \cdot 10^4$	$< 5 \cdot 10^4$	$< 5 \cdot 10^6$
$\tilde{\lambda}_i$	m	2.3	0.1	0.01
$\tilde{\lambda}_{Debye}$	m	$1.7 \cdot 10^{-4}$	$1.1 \cdot 10^{-5}$	$1.3 \cdot 10^{-6}$
β		$1.5 \cdot 10^{-5}$	0.1	0.15
$C_{D,cx}$		0.25	< 0.13	< 5
$C_{H,e}$		$1.9 \cdot 10^5$	$6.3 \cdot 10^2$	$1.4 \cdot 10^2$
$C_{H,i}$		$5.7 \cdot 10^2$	$2.1 \cdot 10^1$	4.5
ϵ		$2.6 \cdot 10^{-2}$	0.21	$5.2 \cdot 10^{-2}$
M		0.9	1.6	3.3
M_A		$2.9 \cdot 10^{-3}$	0.51	1.3
$R_{e,i}$		0.46	2.5	$1.9 \cdot 10^2$

Table 2.3: Typical plasma parameters for the present and future conditions in MBX as well as for MCX [7, 12].

means that viscosity can affect the system, mostly if finer scales appear in the plasma. In the future we aim to reach an ion skin depth (characteristic length for magnetofluid states) slightly smaller than the size of the plasma as needed.

In the case of MCX, the inertia is small compared to the electromagnetic forces but not negligible ($\epsilon = 0.05$). The self magnetic field should not be neglected because is of the order of the external field.

In summary, in this section we have reached a simplified set of dimensionless equations, after some assumptions, containing the terms used in the dissipationless theory of magnetofluid states. Accordingly, we chose two sets of parameters to use in the following sections. The first set corresponds to present conditions in MBX where the plasma density is low and the speeds are supersonic but sub-Alfvenic, and the second set for future conditions with higher densities where magnetofluid states can exist.

2.2 Dissipationless Electron-Ion equations

In order to study either magnetofluid states or externally driven rotating plasma solutions and their difference with ideal MHD predictions we seek a region in the parameter space where the dissipative terms in the electron and ion equations can be neglected. We assume a barotropic relationship $p = p(n)$

so that $\nabla p/n = \nabla \tilde{p}(n)$. The ion, electron and momentum equations become

$$-\partial_t \mathbf{A} + \left[\left(\mathbf{V} - \frac{\mathbf{J}}{n} \right) \times \mathbf{B} \right] = -\nabla P_e, \quad P_e = \frac{\epsilon \tilde{p}_e}{M_i^2} - \phi \quad (2.19)$$

$$\partial_t (\mathbf{A} + \epsilon \mathbf{V}) + [(\mathbf{B} + \epsilon \nabla \times \mathbf{V}) \times \mathbf{V}] = -\nabla P_i, \quad P_i = \frac{\epsilon \tilde{p}_i}{M_i^2} + \frac{\epsilon V^2}{2} + \phi \quad (2.20)$$

$$\partial_t \mathbf{V} + (\nabla \times \mathbf{V}) \times \mathbf{V} - \frac{\mathbf{J} \times \mathbf{B}}{\epsilon n} = -\nabla P_T, \quad P_T = \frac{\tilde{p}}{M_i^2} + \frac{V^2}{2} \quad (2.21)$$

where $\mathbf{B} = \nabla \times \mathbf{A}$ and the definition of $P_T = \epsilon^{-1}(P_e + P_i)$ in Eq. (2.21) ($\tilde{p} = \tilde{p}_i + \tilde{p}_e$) is made so that it becomes of order unity. At the same time it shows that the perpendicular current to the magnetic field \mathbf{J}_\perp is of the order ϵ (and the self magnetic field becomes order M_A^2) unless finer scales appear in the plasma so that it becomes of order $\epsilon \nabla$ or a higher order derivative. This is a distinct feature of magnetofluid states, where configurations with $\epsilon \sim 0$ can differ considerably from the ideal MHD predictions. On the other hand parallel currents can be completely carried by electrons while ions remain motionless so that they do not need to be of order ϵ .

Electron and ion equations (2.19)-(2.20) can be written in the ideal induction forms as [27]

$$\partial_t \tilde{\mathbf{A}}_j - \mathbf{U}_j \times \boldsymbol{\Omega}_j = \nabla \chi_j \rightarrow \partial_t \boldsymbol{\Omega}_j - \nabla \times (\mathbf{U}_j \times \boldsymbol{\Omega}_j) = 0 \quad (2.22)$$

$$\tilde{\mathbf{A}}_e = \mathbf{A}, \quad \mathbf{U}_e = \mathbf{V} - \mathbf{J}/n, \quad \boldsymbol{\Omega}_e = \mathbf{B}, \quad \chi_e = P_e$$

$$\tilde{\mathbf{A}}_i = \mathbf{A} + \epsilon \mathbf{V}, \quad \mathbf{U}_i = \mathbf{V}, \quad \boldsymbol{\Omega}_i = \mathbf{B} + \epsilon \nabla \times \mathbf{V}, \quad \chi_i = -P_i$$

where \mathbf{U} are the effective flows, and $\tilde{\mathbf{A}}, \boldsymbol{\Omega}$ the generalized flows and corresponding vorticities respectively. The generalized vorticities are then ideally induced

by the effective flows. It is important to note that the generalized vorticities are not the vorticities of the effective flows but the generalized flows.

There are different possible choices to solve this coupled non linear problem, we will work with two of them:

1. Magnetofluid states [27]: in stationary state the generalized vorticities are aligned to the effective flows ($\mathbf{U}_j \parallel \mathbf{\Omega}_j$) so that the different P_s 's are constant in space leading to magneto-Bernoulli confinement, $\tilde{p}/M_i^2 + V^2/2 = \text{constant}$. While the Bernoulli equation appears in fluids assuming an irrotational flow, in a magnetofluid the $\mathbf{J} \times \mathbf{B}$ term balances the vorticity term. Usually, in magnetofluids the fluid velocity is normalized to the Alfvén speed while the pressure leads to the plasma beta. In our case, the typical plasma speed \tilde{V} is the normalization factor so that the Mach number M_i appears in the pressure term. This system contains helicity due to the alignment of the generalized flows and vorticities, $\tilde{\mathbf{A}} \cdot \mathbf{\Omega} = (\nabla \times^{-1} \mathbf{\Omega}) \cdot \mathbf{\Omega} \neq 0$. As previously said, we plan to create magnetofluid states embedded in an external magnetic field after a reconnection process. The core of this state would not have a direct connection to the external world. That is, the magnetic field lines connected to the external drive would reach only the boundary of the magnetofluid state. The control of the profile is only indirect.
2. Externally driven rotating plasma states: under certain conditions the effective and generalized flows can be aligned ($\mathbf{U}_j \parallel \mathbf{A}_j$) and completely

perpendicular to the corresponding effective and generalized vorticities so that the net result of the right hand sides of the Eqs. (2.19)-(2.20) are gradient forces instead of zero as in magnetofluid states. These states have been produced in rotating plasmas experiments without a reconnection process with small values of ϵ . In this case, the plasma core has a direct connection to the external world. That is, the magnetic field lines connected to the external drive reach the inner parts of the rotating plasma creating a direct control of the plasma profile.

2.2.1 Validity Region

The simplifications that lead to the dissipationless set of equations are only valid in one region of the parameter space. The terms dropped are the viscosity, neutral and source drag and the friction between electrons and ions. This region shrinks when a strong coupling between the velocity and magnetic fields is required. MBX aims to operate under these conditions to reach magnetofluid states. Fig. 2.1 shows a region of strong coupling ($\epsilon > .5$, $M_A > .5$) embedded in another with less coupling ($\epsilon > .1$, $M_A > .1$). The surfaces corresponds to the constraints imposed by ϵ and M_A as well as by neglecting the dissipative terms ($R_{e,i} > 1$, $C_{H,i} > 1$). The present conditions in MBX (red dot) are far from the region mainly due to the low density. MCX present conditions (magenta square) are away from the region due to the high magnetic fields used.

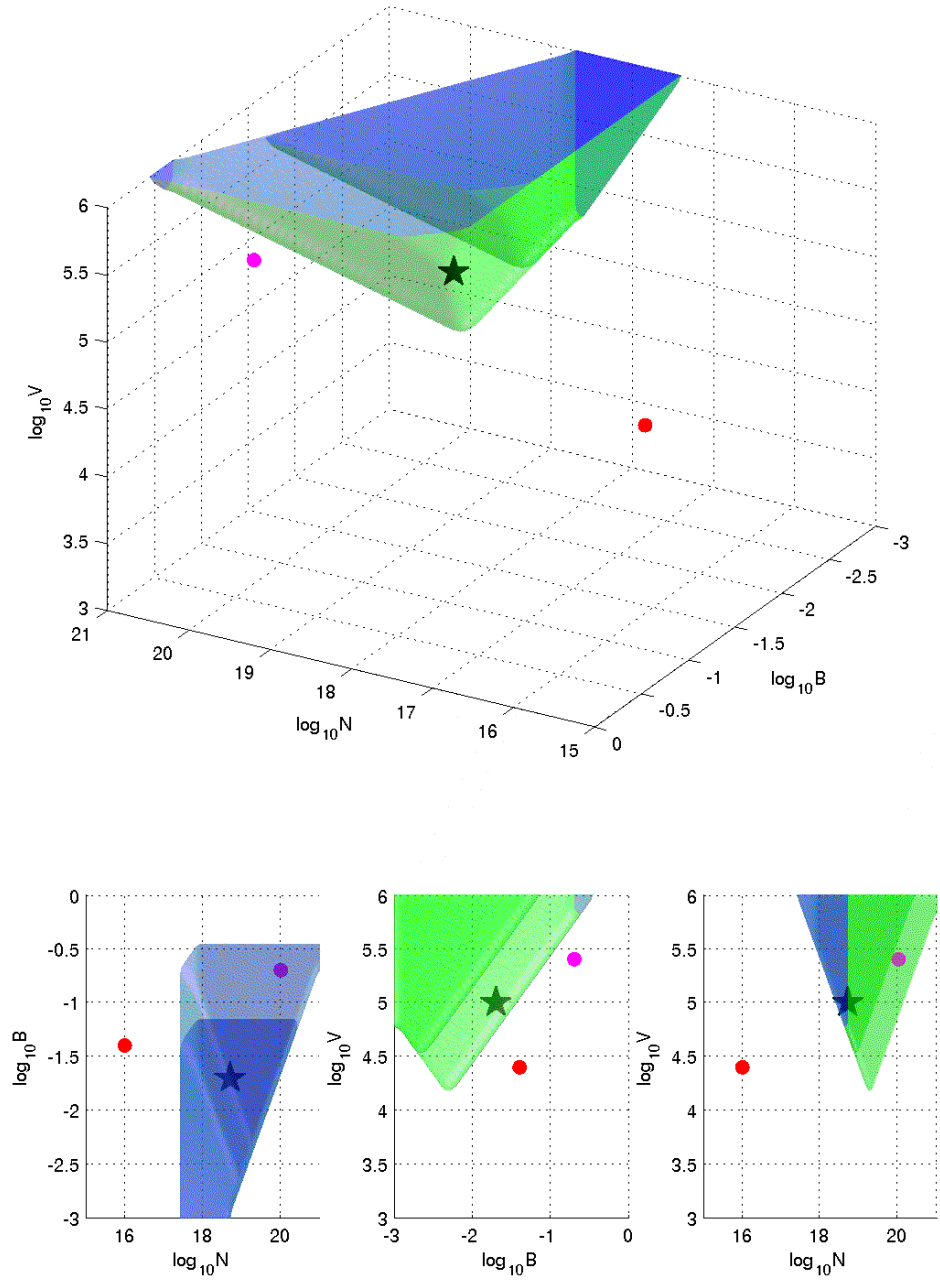


Figure 2.1: Region in parameter space where dissipationless equations apply and strongly coupled magnetofluid states can exist. Units are in MKS.

The future conditions where MBX plans to operate (black star) are at the edge of the strong coupling region. Stronger coupling could be achieved lowering the external magnetic field however the Larmor orbit of the particles would become comparable to the size of the machine.

2.2.2 Magnetofluid States

Magnetofluid states solutions introduced by Mahajan and Yoshida [27] appear in the two fluid treatment of the plasma dynamics as compared to the flowless MHD force-free relaxed states introduced by Taylor [42]. Ideal MHD allows solutions of the Beltrami form

$$\mu_0 \mathbf{J} = \nabla \times \mathbf{B} = \kappa(x) \mathbf{B} \quad (2.23)$$

where $\kappa(x)$ is a scalar function that satisfies $\mathbf{B} \cdot \nabla \kappa(x) = 0$. These states are force free fields since $-\nabla p = \mathbf{J} \times \mathbf{B} = 0$, and can be derived minimizing the magnetic energy $E = \frac{1}{2} \int B^2 d^3x$ subject to the constraint that the local magnetic helicity $h_1 = \frac{1}{2} \int \mathbf{A} \cdot \mathbf{B} d^3x$ is a constant of motion [46]. Despite the simple form of Beltrami equation (2.23), a solution is hard to find because of the dependence of κ with the position, leading to a nonlinear system of partial differential equations. Taylor assumed that dissipative processes would destroy all local helicity constraints ("relaxation process") leaving only the global helicity conserved. This processes of self organization of the plasma current (or magnetic field) leads to Taylor's relaxed states that correspond to constant- κ Beltrami fields [42]

$$\mu_0 \mathbf{J} = \nabla \times \mathbf{B} = \kappa \mathbf{B} \quad (2.24)$$

The problem then reduces to find the eigenvalues of the curl operator. Relaxed states have served as a paradigm for plasma self organization and have been invoked to understand the nature of both laboratory and astrophysical plasmas. The equilibrium states of a reversed field pinch (RFP) are considered prime examples of such relaxation [43]. In RFP's a toroidal current is induced in a plasma embedded in a toroidal field to generate a poloidal magnetic field. In some particular cases that depend on the initial conditions and after a turbulent phase the toroidal field can reverse direction at the plasma edge.

Magnetofluid states extend the ideal MHD structures introduced by Taylor including the self organization of the plasma under the combined influence of currents and flows in the context of a two fluid system. The simplest equilibrium of the coupled electron-ion equations ideal induction forms (2.22) is one where the generalized vorticities are aligned with the effective flows [26]

$$\begin{aligned} \Omega_e \parallel \mathbf{U}_e &\rightarrow a_e \mathbf{B} = n \left\{ \mathbf{V} - \frac{\epsilon}{M_A^2} \frac{\nabla \times \mathbf{B}}{n} \right\} \\ \Omega_i \parallel \mathbf{U}_i &\rightarrow \mathbf{B} + \epsilon \nabla \times \mathbf{V} = a_i n \mathbf{V} \\ \text{satisfying } \nabla \cdot (n \mathbf{V}) &= 0. \end{aligned}$$

This transforms the original expressions into a system of linear equations for the variable \mathbf{B}, \mathbf{V} . The density couples these equations to the solutions of $\nabla P_e = \nabla P_i = 0$ leading to a nonlinear problem. In order to find analytical solutions and reveal the most distinct features of magnetofluids a constant density is assumed, that in normalized units becomes $n = 1$. Solving for $\mathbf{B} (\mathbf{V}$

yields the same form) leads to the double curl Beltrami equation

$$\epsilon^2 \nabla \times \nabla \times \mathbf{B} + \epsilon \alpha \nabla \times \mathbf{B} + \beta \mathbf{B} = 0 \quad (2.25)$$

where $\alpha = a_e M_A^2 - a_i$ and $\beta = M_A^2(1 - a_i a_e)$. The solutions to this equation cover a wider and richer range of equilibria that can differ considerably from Taylor's states. Eq. (2.25) can be written as

$$(\epsilon \nabla \times - \Lambda_+)(\epsilon \nabla \times - \Lambda_-)\mathbf{B} = D(\mathbf{r}, \Lambda_+)D(\mathbf{r}, \Lambda_-)\mathbf{B} = 0$$

where $D(\mathbf{r}, \Lambda_{\pm}) = (\epsilon \nabla \times - \Lambda_{\pm})$, and $\Lambda_{\pm} = \frac{1}{2} \left[-\alpha \pm \sqrt{\alpha^2 - 4\beta} \right]$. The solutions can be constructed as a linear combination, $\mathbf{B} = C_+ \mathbf{B}_+ + C_- \mathbf{B}_-$, of single Beltrami solutions $D(\mathbf{r}, \Lambda_{\pm})\mathbf{B}_{\pm} = 0$. When the problem is cast in this form \mathbf{B}_{\pm} and its coefficients can be complex as long as the final solution is a real physical quantity. As an example consider Eq. (2.25) with $\epsilon = 1, \alpha = 0, \beta = 1$ so that $\nabla \times \nabla \times \mathbf{B} = -\nabla^2 \mathbf{B} = -\mathbf{B}$. One type of solution is $\mathbf{B} = \exp(x)(C_y \hat{\mathbf{y}} + C_z \hat{\mathbf{z}})$, C_y & $C_z \in \mathbb{R}$. However, the solutions $D(\mathbf{r}, \Lambda_{\pm})\mathbf{B}_{\pm} = 0$ with $\Lambda_{\pm} = \pm i$ are of the form $\mathbf{B}_{\pm} = \exp(x)(\pm i \hat{\mathbf{y}} + \hat{\mathbf{z}})$. A linear combination of them yields $\mathbf{B} = C_+ \exp(x)(i \hat{\mathbf{y}} + \hat{\mathbf{z}}) + C_- \exp(x)(-i \hat{\mathbf{y}} + \hat{\mathbf{z}})$ that is the same as the final real solution \mathbf{B} taking $C_+ = C_-^* = \frac{1}{2}(C_z - i C_y)$.

Originally, $a_e, a_i \in \mathbb{R}$ and \mathbf{B} is real for being a physical quantity then $\alpha, \beta \in \mathbb{R}$. Since Eq. (2.25) is linear in \mathbf{B} and all its coefficients are real then $\tilde{\mathbf{B}} \in \mathbb{C}/\mathbf{B} = \text{Re}(\tilde{\mathbf{B}})$ is also a solution to the equation. It is possible then to work with the solutions of $D(\mathbf{r}, \Lambda_{\pm})\mathbf{B}_{\pm} = 0$ so that $\tilde{\mathbf{B}} = C_+ \mathbf{B}_+ + C_- \mathbf{B}_-, C_{\pm} \in \mathbb{C}$ and take the real part at the end of the calculation to find \mathbf{B} . In the example given before the solution using this technique requires $C_+ = C_y, C_- = i C_x$.

The solutions to Eq. (2.25) using complex quantities and taking the real part at the end of the calculation are given by

$$\mathbf{B} = C_+ \mathbf{B}_+ + C_- \mathbf{B}_-, \quad \nabla \times \mathbf{B}_\pm = \left(\frac{\Lambda_\pm}{\epsilon} \right) \mathbf{B}_\pm \quad (2.26)$$

$$\mathbf{V}_e = a_e \mathbf{B} \quad (2.27)$$

$$\mathbf{A} = \epsilon \left(\frac{C_+}{\Lambda_+} \mathbf{B}_+ + \frac{C_-}{\Lambda_-} \mathbf{B}_- \right) \quad (2.28)$$

$$M_A^2 \mathbf{J} = \Lambda_+ C_+ \mathbf{B}_+ + \Lambda_- C_- \mathbf{B}_- = \epsilon \nabla \times \mathbf{B} \quad (2.29)$$

$$\mathbf{V} = a_e \mathbf{B} + \mathbf{J} = \left(a_e + \frac{\Lambda_+}{M_A^2} \right) C_+ \mathbf{B}_+ + \left(a_e + \frac{\Lambda_-}{M_A^2} \right) C_- \mathbf{B}_- \quad (2.30)$$

$$\nabla \times \mathbf{V} = a_i \mathbf{V} - \mathbf{B} = \frac{1}{M_A^2} [(\Lambda_+ - \beta) C_+ \mathbf{B}_+ + (\Lambda_- - \beta) C_- \mathbf{B}_-] \quad (2.31)$$

Magnetofluid states have many important features that can be seen from the previous formulation:

- The number of solutions from a combination of Beltrami fields increases considerably the number of states found in single Beltrami-Taylor states, that are a singular limit of Eq. (2.25) when the higher order derivative is neglected [48].
- The equilibrium solutions lead to Bernoulli conditions $\nabla P_e = \nabla P_i = \nabla P_T = 0$. Electrons follow a Boltzmann distribution while the total fluid follows the Bernoulli equation $\frac{\tilde{p}}{M_i^2} + \frac{V^2}{2} = \text{constant}$, showing that the right shear flow can create a strong pressure gradient and a highly confined plasma.

- The solutions present two characteristics scale lengths $(\Lambda_{\pm}/\epsilon)^{-1}$ that depend on the intrinsic ion skin depth (λ_i) contained in ϵ , compared to the scaleless ideal MHD.
- The appropriate choice of constants C_+, C_- can lead to a system where a smooth magnetic field coexists with a highly varying velocity field or vice versa.
- While Taylor states are paramagnetic ($\nabla \times \mathbf{B} = \kappa \mathbf{B}$ leads to $\nabla^2 \mathbf{B} + \kappa^2 \mathbf{B} = 0$ with $\kappa^2 > 0$), magnetofluid states do not have the positivity requirement and $\alpha = 0, \beta = -\gamma^2$ in the double curl Beltrami equation (2.25) leads to diamagnetic structures where $\nabla^2 \mathbf{B} - \gamma^2 \mathbf{B} = 0$.
- Magnetofluids can be obtained minimizing the enstrophy of the system $F = \frac{1}{2} \int |\nabla \times (\mathbf{V} + \mathbf{A})|^2 d^3x$ keeping the magnetic helicity h_1 and the helicity of the generalized vorticity $h_2 = \frac{1}{2} \int (\mathbf{V} + \mathbf{A}) \cdot (\nabla \times \mathbf{V} + \mathbf{B}) d^3x$ constants [47]. Relaxation then leads to a state of minimum turbulence instead of a minimum energy as in Taylor states.
- Electrons follow the magnetic lines while ions have their motion along the lines modified by their inertia through the vorticity.

Many of the features listed previously can be seen using the simple example of a one dimensional cylinder configuration [27]. The solutions to the eigenvalue problem of the curl operator in cylindrical coordinates are given in

terms of Bessel functions [6]

$$\nabla \times \mathbf{H} = a\mathbf{H} \Rightarrow \mathbf{H} = \mathbf{S} + \mathbf{T} \quad (2.32)$$

$$\mathbf{T} = a\nabla \times (\psi \mathbf{i}) = a\nabla \psi \times \mathbf{i}, \text{ with } \mathbf{i} \text{ constant unit vector.}$$

$$\nabla^2 \psi + a^2 \psi = 0 \text{ (Helmholtz's eq.)}, \text{ the same for } \mathbf{T} \text{ and } \mathbf{S}.$$

$$\mathbf{S} = a^{-1} \nabla \times \mathbf{T}, \quad \mathbf{T} = a^{-1} \nabla \times \mathbf{S}$$

For the cylindrical solution we chose $a = \left(\frac{\Lambda}{\epsilon}\right)$, $\hat{\mathbf{i}} = \hat{\mathbf{z}}$, $\mathbf{H} = \mathbf{u}$, $\mathbf{S} = \mathbf{u}_T$, $\mathbf{T} = \mathbf{u}_P$, $\psi = \chi$, where P, T mean poloidal and toroidal vectors

$$\begin{aligned} \mathbf{u}_{\pm}(\mathbf{r}; m, k) &= \underbrace{\left(\frac{\Lambda_{\pm}}{\epsilon}\right) \nabla \chi_{\pm} \times \hat{\mathbf{z}}}_{\mathbf{u}_{P\pm}(\mathbf{r}; m, k)} + \underbrace{\nabla \times (\nabla \chi_{\pm} \times \hat{\mathbf{z}})}_{\mathbf{u}_{T\pm}(\mathbf{r}; m, k)} \\ \chi_{\pm}(\mathbf{r}; m, k) &= J_m(\mu_{\pm} r) \exp[i(m\theta - kz)] \end{aligned}$$

where J_m is the Bessel function of order m , and $\mu_{\pm}^2(k) = \left(\frac{\Lambda_{\pm}}{\epsilon}\right)^2 - k^2$. For axisymmetric ($m = 0$, $\partial_{\theta} = 0$) and homogeneous in z ($k = 0$, $\partial_z = 0$), cylindrical equilibria becomes

$$\mathbf{B}_{\pm}(r) = \left(\frac{\Lambda_{\pm}}{\epsilon}\right)^2 \left[\underbrace{J_0\left(\frac{\Lambda_{\pm}}{\epsilon} r\right) \hat{\mathbf{z}}}_{\mathbf{B}_{T\pm}} + \underbrace{J_1\left(\frac{\Lambda_{\pm}}{\epsilon} r\right) \hat{\theta}}_{\mathbf{B}_{P\pm}} \right], \quad \chi_{\pm}(r) = J_0\left(\frac{\Lambda_{\pm}}{\epsilon} r\right)$$

Typical solutions for the conditions $\mathbf{B}(0) = 1$ and $\mathbf{J}(0) = 1$ at the axis are shown in Fig. 2.2. In one limiting case, where the singular double curl term is negligible, the flowless reverse field pinch solutions can be obtained (Fig. 2.2 - left hand side). In other cases, the strong interaction between magnetic and velocity fields leads to multiple scale structures, confined by the Bernoulli

mechanism, fully diamagnetic, with a high β value of 0.2 (Fig. 2.2 - right hand side).

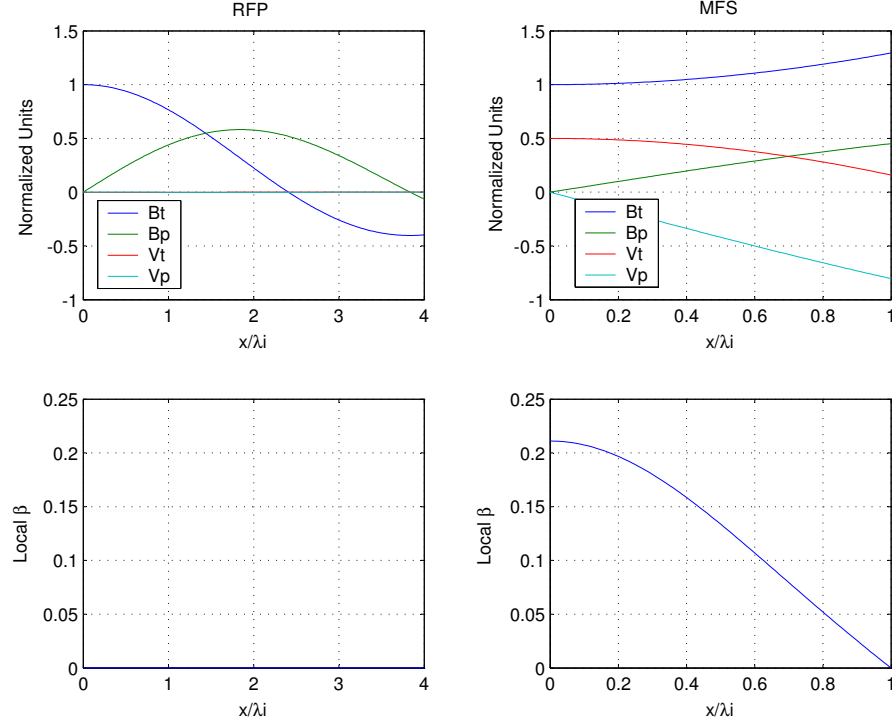


Figure 2.2: 1-D cylindrical solution for a double curl Beltrami system. In one limiting case, where the singular double curl term is negligible, the flowless reverse field pinch solutions can be obtained (left hand side). In other cases, the strong interaction between magnetic and velocity fields in a magnetofluid state leads to high confinement through Bernoulli mechanism (right hand side).

In MBX we start with a configuration that contains an external magnetic mirror field to obtain the velocities needed for magnetofluid states. Since the set of linear equations found after using the magnetofluids assumption (generalized vorticities aligned to effective flows) is non linear, the introduc-

tion of an external magnetic field is not trivial and depends on the particular case considered. One of the possible solutions to this problem is to find a magnetofluid state that when combined with an external field leads to forces that are a gradient of a potential. In the previous case where a one dimensional cylinder is considered, magnetofluid configurations can exist in the presence of a constant magnetic field $\mathbf{B}_0 = B_0 \hat{\mathbf{z}}$. In this case the electron and ion equations and the magnetofluid assumption ($\mathbf{V}_e = a_e \mathbf{B}^{self}, \mathbf{B}^{self} + \epsilon \nabla \times \mathbf{V} = a_i \mathbf{V}$) lead to

$$\begin{aligned} a_e \mathbf{B}^{self} \times \mathbf{B}_0 &= -\nabla P_e \\ \mathbf{B}_0 \times \mathbf{V} &= -\nabla P_i \end{aligned}$$

where \mathbf{B}^{self} is the magnetic field created by plasma currents. Since $\mathbf{B}^{self}, \mathbf{V}$ are linear combinations of \mathbf{B}_\pm the only requirement to satisfy the equations is that $\mathbf{B}_0 \times \mathbf{B}_\pm$ can be written as a gradient, so that $\nabla \times (\mathbf{B}_0 \times \mathbf{B}_\pm) = 0$. In the cylindrical case

$$\nabla \times (\mathbf{B}_0 \times \mathbf{B}_\pm) = \underbrace{\mathbf{B}_0 (\nabla \cdot \mathbf{B}_\pm)}_{=0} - \underbrace{\mathbf{B}_\pm (\nabla \cdot \mathbf{B}_0)}_{=0} + \underbrace{(\mathbf{B}_0 \cdot \nabla) \mathbf{B}_\pm}_{B_0 \partial_z} - \underbrace{(\mathbf{B}_\pm \cdot \nabla) \mathbf{B}_0}_{B_0 (\mathbf{B}_\pm \cdot \nabla) \hat{\mathbf{z}}} = 0$$

The first two terms on the right hand side are zero because $\nabla \cdot \mathbf{B} = 0$. The third term is zero because $\mathbf{B}_\pm(r)$ is not a function of the z component, and the last term is zero because the derivatives of $\hat{\mathbf{z}}$ are zero. This means that the interactions must derive from a gradient that can be calculated as follows

$$\mathbf{B}_0 \times \mathbf{B}_\pm = B_0 \left(\frac{\Lambda_\pm}{\epsilon} \right)^2 \hat{\mathbf{z}} \times (\nabla \chi_\pm \times \hat{\mathbf{z}}) = \nabla \left[B_0 \left(\frac{\Lambda_\pm}{\epsilon} \right)^2 \chi_\pm \right]$$

Then, the final state is found using the previous magnetofluid solution for the one dimensional cylinder, adding the constant external field, and finally finding the pressure using Bernoulli equation that now contains the coupling between the external magnetic field and the plasma, $B_0 \left(\frac{\Lambda_{\pm}}{\epsilon} \right)^2 \chi_{\pm}$.

Not all configurations are suitable for the introduction of an external magnetic field. In the case of the modeling of the H-mode layer [28] the introduction of a toroidal magnetic field generated by the external coils requires more conditions on the fields and layers so that external forces become gradient forces. In the case of MBX the external field is a mirror and it is not constant but has a dependence of the form $\cos(z)$. We have not reached a satisfactory decoupling in this configuration due to the z dependence.

2.2.3 Externally Driven Rotating Plasma Solutions

Solutions for a rotating plasma immersed in an external mirror magnetic field can be created by decoupling \mathbf{A} , \mathbf{V} and their vorticities in completely poloidal and toroidal fields as shown in Fig. 2.3. Let us assume a stationary state ($\partial_t = 0$) and symmetry around the z axis ($\partial_\phi = 0$). The fields can be written as

$$\mathbf{V} = V_\phi \hat{\phi} \rightarrow \nabla \times \mathbf{V} = \nabla \times (V_\phi \hat{\phi}) = \frac{\nabla(rV_\phi) \times \hat{\phi}}{r} \quad (2.33)$$

$$\mathbf{A} = A_\phi \hat{\phi} \rightarrow \mathbf{B} = \nabla \times (A_\phi \hat{\phi}) = \frac{\nabla(rA_\phi) \times \hat{\phi}}{r} = \frac{\nabla \Psi \times \hat{\phi}}{r} \quad (2.34)$$

$$\tilde{\mathbf{J}} = \frac{\nabla \times \mathbf{B}}{M_A^2} = -\frac{\nabla^2 \mathbf{A}}{M_A^2} = -\frac{1}{M_A^2} \left[\nabla^2 A_\phi - \frac{A_\phi}{r^2} \right] \hat{\phi} = -\frac{\Delta^* \Psi}{M_A^2 r} \hat{\phi} = \tilde{j}_\phi \hat{\phi} \quad (2.35)$$

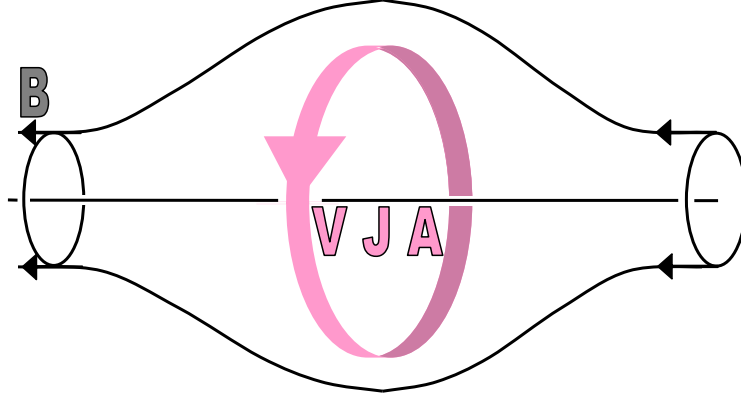


Figure 2.3: Decoupling of the fields representing a rotating plasma in a poloidal magnetic field.

where $\nabla \cdot \mathbf{A} = \partial_\phi A_\phi = 0$, and $\nabla \times (\hat{\phi}/r) = 0$ were used, $\Psi \equiv rA_\phi$ is proportional to the total magnetic flux and $\Delta^* \equiv r\partial_r(\frac{\partial r}{r}) + \partial_z^2$ is the Grad-Shafranov operator. This choice also satisfies the particle conservation equation (2.8) with the assumption that sources are neglected. The choice of $\mathbf{J} = \epsilon \tilde{\mathbf{J}}$ is based on the fact that \mathbf{J}_\perp is of order ϵ as explained at the beginning of Section 2.2 so that $\tilde{\mathbf{J}}$ is of order unity. $\Psi = \Psi^{ext} + \Psi^{self}$ where Ψ^{ext} is the flux generated by external currents to the plasma (such that $\Delta^* \Psi^{ext} = 0$ inside the plasma) that lead to a mirror field in our case, while Ψ^{self} is created by plasma currents.

Under these choices, Eqs. (2.19)-(2.21) transform into

$$(V_\phi - \epsilon j_\phi/n) \hat{\phi} \times \frac{\nabla \Psi \times \hat{\phi}}{r} = \frac{(V_\phi - \epsilon j_\phi/n)}{r} \nabla \Psi = -\nabla P_e \quad (2.36)$$

$$\frac{\nabla(\Psi + \epsilon r V_\phi) \times \hat{\phi}}{r} \times V_\phi \hat{\phi} = -\frac{V_\phi}{r} \nabla(\Psi + \epsilon r V_\phi) = -\nabla P_i \quad (2.37)$$

$$-\frac{V_\phi}{r} \nabla(r V_\phi) - \frac{j_\phi/n}{r} \nabla \Psi = -\nabla P_T \quad (2.38)$$

The electron and ion equations are of the form $\pm w \nabla g = -\nabla P$, where w is a rotational frequency ($w_e = V_{\phi,e}/r, w_i = V_\phi/r$). The solutions to this form can be found in the following way: assume $\pm w = \pm w(g) = \frac{dW(g)}{dg}$, then $w \nabla g = \frac{dW(g)}{dg} \nabla g = \nabla W(g) = -\nabla P$ so that $W(g) = \pm \int w(g) dg = -P + C$, with C a constant. This method yields the same solutions as taking the curl of the equation $\nabla \times (w \nabla g) = \nabla w \times \nabla g = 0$. If $w = w(g)$ then $\nabla w = \frac{dw}{dg} \nabla g$ and the equation is satisfied. This means that the torque of the forces such as Coriolis and $\mathbf{J} \times \mathbf{B}$ balance each other leaving only gradient forces that are balanced by P_s . Electrons rotate on the magnetic flux surfaces while ions try to do the same but their motion is modified by the inertia and are not tight to the magnetic surface.

Defining $w_j = j_\phi/(nr)$ the total momentum equation (2.38) and its projection along the magnetic field lines are

$$r w_i^2 \nabla r + w_j \nabla \Psi = \nabla(\tilde{p}/M_i^2) \xrightarrow{\cdot \hat{\parallel}} r w_i^2 \nabla_{\parallel} r = \nabla_{\parallel}(\tilde{p}/M_i^2) \quad (2.39)$$

which shows the basic concept of centrifugal confinement in a rotating mirror. The centrifugal force increases the pressure along the magnetic field lines when we move from the mirror throats to the equatorial plane as shown in Fig. 1.2.

Once $w_e(g_e)$ and $w_i(g_i)$ are known the solution for the pressure and electric potential are:

$$\phi = \frac{1}{2} \left[(W_e - W_i) + \epsilon \left(\frac{\tilde{p}_e - \tilde{p}_i}{M_i^2} - \frac{V_\phi^2}{2} \right) \right] + C_\phi \quad (2.40)$$

$$\tilde{p} = \tilde{p}_e + \tilde{p}_i = -M_i^2 \left[\frac{W_e + W_i}{\epsilon} + \frac{V_\phi^2}{2} \right] + C_p \quad (2.41)$$

with C_p and C_ϕ constants. The potential can be further simplified assuming equal electron and ion pressures $\tilde{p}_e = \tilde{p}_i = \tilde{p}/2$.

In ideal MHD closure the velocity of the fluid to the lowest order is $\mathbf{V} \sim (\mathbf{E} \times \mathbf{B})/B^2$ that is the same as requiring $\epsilon \sim 0$. In this case the electron and ion equations become the same containing the zero order motion while the momentum equation accounts for the small perturbation given by ϵ . The magnetic field lines become equipotentials ($\phi \propto \Psi$) as seen in the electron equation while ions tend to isorotate ($w_i \sim w_i(\psi)$) as electrons do. The electrons and ions rotate together.

Taking the curl of the momentum equation (2.38), we get an equation combining Ψ , $w_e(\Psi)$, and w_j

$$\begin{aligned} \nabla \Psi \times \nabla w_j &= \nabla w_i \times \nabla (r^2 w_i) = \frac{1}{2} \nabla w_i^2 \times \nabla r^2 = \\ &= \frac{1}{2} \nabla (w_e(\Psi) + \epsilon w_j)^2 \times \nabla r^2 = r \partial_z (w_e(\Psi) + \epsilon w_j) \hat{\phi} \end{aligned} \quad (2.42)$$

that has to be combined with Maxwell's equation $\Psi = \Psi(w_j)$ to yield the complete solution. When $\epsilon \ll 1$ and the gradients are not large the last

equation becomes

$$\begin{aligned}\nabla\Psi \times \nabla w_j &\sim \frac{1}{2}\nabla(w_e(\Psi))^2 \times \nabla r^2 = \frac{1}{2}\frac{dw_e^2}{d\Psi}\nabla\Psi \times \nabla r^2 = \\ &= \frac{1}{2}\nabla\Psi \times \nabla(r^2\frac{dw_e^2}{d\Psi})\end{aligned}$$

Then $\nabla\Psi \times \nabla\left(w_j - \frac{r^2}{2}\frac{dw_e^2}{d\Psi}\right) \sim 0$ yields solutions of the form [44]

$$w_j \sim r^2 w_e(\Psi) \frac{dw_e(\Psi)}{d\Psi} + F(\Psi)$$

where F is an arbitrary function of the magnetic flux. Then Ψ can be replaced by Ψ^{ext} if the external field is much higher than the field generated by the plasma and the current can be calculated without the need of the ion equation that becomes the same as the electron equation when $\epsilon \ll 1$.

The external magnetic field can be computed numerically as shown in Section 3.3 or approximated with an analytical solution satisfying $\Delta^*\Psi^{ext} = 0$. One solution is given by $\Psi^{ext} = rA_\phi^{ext} = B^{ext}\frac{r^2}{2}(1 - b\frac{I_1(kr)}{kr}\cos(kz))$ [29] that for $kr \ll 1$ becomes $\Psi^{ext} \sim B^{ext}\frac{r^2}{2}(1 - b\cos(kz))$ that resembles a mirror field with a mirror ratio $R = \frac{b+1}{b-1}$. At the throat and equatorial plane where the magnetic field lines are in the $\hat{\mathbf{z}}$ direction the flux appears as created by a constant magnetic field of intensity $B^{ext}(1 \pm b) = R, 1$ respectively in normalized units. In MBX the mirror ratio is $R = 7$ so that $b = 0.75$ and $B^{ext} = 4B(0, 0)$ where $B(0, 0)$ the magnetic field on the axis at the equatorial plane. Since we use this field to normalize the equations then $B^{ext} = 4$. For MBX dimensions (plasma radius = 1 and distance between mirror throats = 4) $k = \pi/2$.

To find the solutions for the specific problem $w_e(\Psi)$ and $w_i(\Psi + \epsilon r^2 w_i)$ have to be chosen so that boundary conditions at the throat are met. We analyze the easiest case considering the rotational frequencies constants in space leading to a rigid rotation of the plasma. Other choices of w_e, w_i lead to different shear profiles. There can be different solutions satisfying the same potential applied at the throat [44]. Experimentally we found that under certain conditions the system is bistable (for the same external conditions the system can be found in two or more states) in both AC and DC bias [18]. The bistability reacts nonlinearly with the control parameters of electron density and external biasing.

Rigid rotation with current ($w_s = \text{constant}$, no shear flow)

$$\begin{aligned} w_e(g_e) &= \frac{(V_\phi - \epsilon j_\phi / n)}{r} = \Omega_e \rightarrow V_{\phi,e} = r\Omega_e \\ w_i(g_i) &= \frac{V_\phi}{r} = \Omega_i \rightarrow V_\phi = r\Omega_i \\ \Rightarrow w_j &= \frac{\Delta\Omega}{\epsilon} = \Omega_j \rightarrow \tilde{j}_\phi = nr\Omega_j \end{aligned}$$

where Ω_i, Ω_e , and $\Delta\Omega = \Omega_i - \Omega_e$ are constants. With this choice, assuming $\tilde{p}_e = \tilde{p}_i = \tilde{p}/2$, and defining the average angular frequency of rotation $\bar{\Omega} \equiv \frac{\Omega_i + \Omega_e}{2}$, the solutions for the electric potential and pressure (Eqs. (2.40)-(2.41)) become

$$\begin{aligned} w_e(g_e) &= \Omega_e \rightarrow W_e = \Omega_e g_e = \Omega_e \Psi \\ w_i(g_i) &= \Omega_i \rightarrow W_i = -\Omega_i g_i = -\Omega_i (\Psi + \epsilon r^2 \Omega_i) \\ \Rightarrow \phi &= \bar{\Omega} \Psi + \epsilon \frac{(r\Omega_i)^2}{4} + C_\phi \end{aligned} \tag{2.43}$$

$$\Rightarrow \tilde{p} = M_i^2 \left[\Omega_j \Psi + \frac{(r\Omega_i)^2}{2} \right] + C_p \tag{2.44}$$

The solution for the potential and the pressure follows the flux function but modified by the inertia of the ions (through Ω_i). While for the potential this modification is small if ϵ is small, for the pressure this two terms can have the same weight depending on the boundary conditions.

A priori all the variables depend on the flux function that is not known until Ampère's law is solved

$$\Delta^* \Psi + M_A^2 r \tilde{j}_\phi = \Delta^* \Psi + M_A^2 n r^2 \Omega_j = 0 \quad (2.45)$$

The equation for the flux (2.45) is not straight forward to solve because the density n couples it with the pressure equation. There are two possibilities to take, each with pros and cons. We can assume a constant density and reach an exact solution. As a consequence we loose the possibility to increase the current at the equatorial plane to generate self magnetic fields. The other possibility is to assume low sub-Alfvénic flows ($M_A^2 \ll 1$) so that the self field can be neglected compared to the external field to find a solution. This possibility does not allow a transition to a possible reconnection process. In this case a constant temperature can be assumed leading to an exponential increase of the density along the magnetic lines due to centrifugal confinement given by Eq. (2.39).

If the density is assumed constant ($n = 1$) the problem decouples and any external field and vector potential satisfying $\Delta^* \Psi^{ext} = 0$ can be added without modifying the result because it is solution to the homogeneous equation. Then, the term $M_A^2 r^2 \Omega_j$ yields the particular solution and the equation

becomes invariant under translation in z . Choosing $\Psi^{ext} = \Psi^{ext}(r)$ the differential equation reads $\Delta^* \Psi^{ext} = \partial_r \left(\frac{\partial_r \Psi^{ext}}{r} \right) + \partial_z^2 \Psi^{ext} = \partial_r \left(\frac{\partial_r \Psi^{ext}(r)}{r} \right) = -M_A^2 r^2 \Omega_j$. The solution is found assuming $\Psi^{ext}(r) = Cr^l \Rightarrow l = 4$ and $C = -M_A^2 \frac{\Omega_j}{8}$. The Biot-Savart integral is also simplified due to the symmetry around $\hat{\mathbf{z}}$ and arrives to the same result. Then, the final solution is any vacuum field added to

$$\begin{aligned} \Psi^{self} = -M_A^2 \frac{\Omega_j}{8} r^4, \mathbf{A}^{self} = -M_A^2 \frac{\Omega_j}{8} r^3 \hat{\phi} &\rightarrow \mathbf{B}^{self} = -M_A^2 \frac{\Omega_j}{2} r^2 \hat{\mathbf{z}} \\ \tilde{\mathbf{J}} = r \Omega_j \hat{\phi} &\rightarrow \mathbf{J} = \epsilon r \Omega_j \hat{\phi} \end{aligned}$$

So far the system contains 2 independent variables that can be Ω_i, Ω_e that we have no control over. Instead we have control at the throat with the applied potential. An extra consideration is connected to the pressure that is built by the combination of centrifugal forces and diverging magnetic field lines. If we consider a linear machine instead of a mirror system there are two options for the pressure. There can be rotation and centrifugal force that is balanced by the current generated by the extra drift that the ions experience due to the centrifugal force in a constant density system, Eq. (2.39),

$$r w_i^2 \nabla r + w_j \nabla \Psi = 0$$

where no extra pressure is generated along the magnetic field lines. The other option is similar to a θ -pinch where the pressure is balanced by an induced current

$$w_j \nabla \Psi = \nabla(\tilde{p}/M_i^2)$$

The only difference between these two situations is the pressure at the boundary. Either the density is constant or there is a density profile. For a mirror system the situation is similar. If the system initially starts with zero biasing and a constant pressure profile at the throat and then potential is applied, the pressure at the boundary will remain constant as in the linear system while inside the mirror it will increase due to centrifugal confinement along the lines given by Eq. (2.39). This is the case that we are interested in. So, to find the solutions for the rigid rotation case we will choose the rotational frequencies so that the throat pressure is nearly constant that according to Eq. (2.44) requires $\Omega_j \Psi(r, 2) \sim -(r\Omega_i)^2/2$. Using the analytical approximation for the external flux $\Psi^{ext}(r, 2) \sim B^{ext}(1+b) \cdot (r^2/2) = R(r^2/2)$ yields $\Omega_j \sim -\Omega_i^2/R$. The current has always a negative sign meaning that it is diamagnetic given by the centrifugal force. The factor $1/R$ arises because at the boundary condition the magnetic field is higher compared to the field at the equatorial plane that has been used to normalize the equations. Written in a different way $\epsilon V_\theta^2/r + BJ = 0, V_\theta = \epsilon \Omega_i, J = \epsilon r \Omega_j \rightarrow \Omega_j = -\frac{\Omega_i^2}{B}$.

In the case of ideal MHD applied to the system the limit $\epsilon \rightarrow 0$ makes ions and electrons lock up in a rigid rotation without any current that is an exact solution to ideal MHD closure. When ϵ is small current starts flowing, the pressure term is not modified while the electric potential becomes $\phi \sim \Omega_i \Psi$ that is different than the two fluid model. However, the pressure is indirectly affected since the potential induces the rotational frequency that in turn affects the pressure profile.

After these considerations we will study a couple of scenarios with present and future parameters in MBX to find the most important characteristics of the different cases. We choose $C_\phi = 0$ in Eq. (2.43) so that $\phi = 0$ on the axis. Similarly, we choose $C_p = 1$ in Eq. (2.44) so that $\tilde{p} = 1$ on the axis. We define the difference in pressure compared to the axis as $\Delta\tilde{p} = \tilde{p} - 1 = M_i^2 \left[\Omega_j \Psi + \frac{(r\Omega_i)^2}{2} \right]$. The electric field at the throat will have both polarities while values for $\epsilon = 0.025, 0.25, 1$ and $M_A = 3 \cdot 10^{-3}, 0.6, 1$ are considered.

The initial case is our present configuration in MBX, $\epsilon \sim .025$, $\phi_0 \sim 250$ V, $E_0 \sim 10^3$ V/m, $M_i \sim 1$, so that $V_0 \sim 2.5 \cdot 10^4$ m/s and $M_A \sim 3 \cdot 10^{-3}$. The case for positive radial electric field E_r at the throat is shown in Fig. 2.4. The normalized difference in potential between the axis and $r = 0.3$ is set to 1 where this particular radius defines the outer magnetic surface at the throat that corresponds to $r = 0.93$ at the equatorial plane of the external magnetic field. At the throat the maximum $\Delta\tilde{p} = 2 \cdot 10^{-2} \ll 1$ so that the pressure is uniform there as required. $\Omega_e = -2.5$ and $\Omega_i = -2.517$ creating a small current (0.017 maximum at the equatorial plane) and corresponding small self magnetic field compared to the external field. The equipotentials follow mostly the flux surfaces, so that the maximum drop in potential along a magnetic line from the throat to the equatorial plane is about ~ 0.03 that corresponds to ~ 7.5 V. The isobars, on the contrary, are far from the magnetic fluxes and show centrifugal confinement. The pressure increases towards the equatorial plane reaching $\Delta\tilde{p} = 2.45$ which for the case of constant density being analyzed

would be a change of the same factor in the plasma temperature. Considering that the self magnetic field is small we could assume constant temperature which would lead to an exponential increase of the density along the lines with a maximum density of 11.6. On the axis there is no centrifugal force acting so that the pressure and electric potential remain constants.

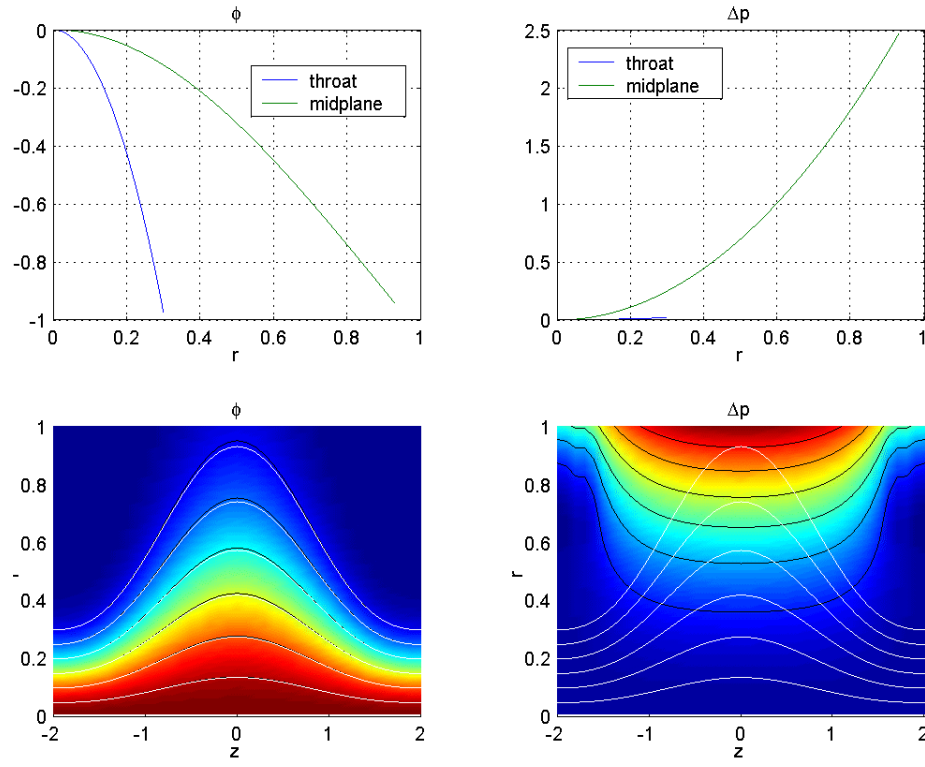


Figure 2.4: Rigid rotation solution for $E_r > 0$ at the mirror throat and present conditions in MBX: $\epsilon \sim 0.025$, $\phi_0 \sim 250$ V, $E_0 \sim 10^3$ V/m, $M_i \sim 1$, so that $V_0 \sim 2.5 \cdot 10^4$ m/s and $M_A \sim 3 \cdot 10^{-3}$. At the top the electric potential and pressure at the throat and equatorial plane as function of radius. At the bottom electric potential and pressure as function of (r, z) combined with magnetic lines (white) and equipotential contours (black).

The case with negative radial electric field is shown in Fig. 2.5. The results are similar to the positive E_r case, with $\Omega_e = 2.58$ and $\Omega_i = 2.561$ to match the boundary conditions. The main qualitative difference appears as an asymmetry in the displacement of the equipotential lines. While the equipo-

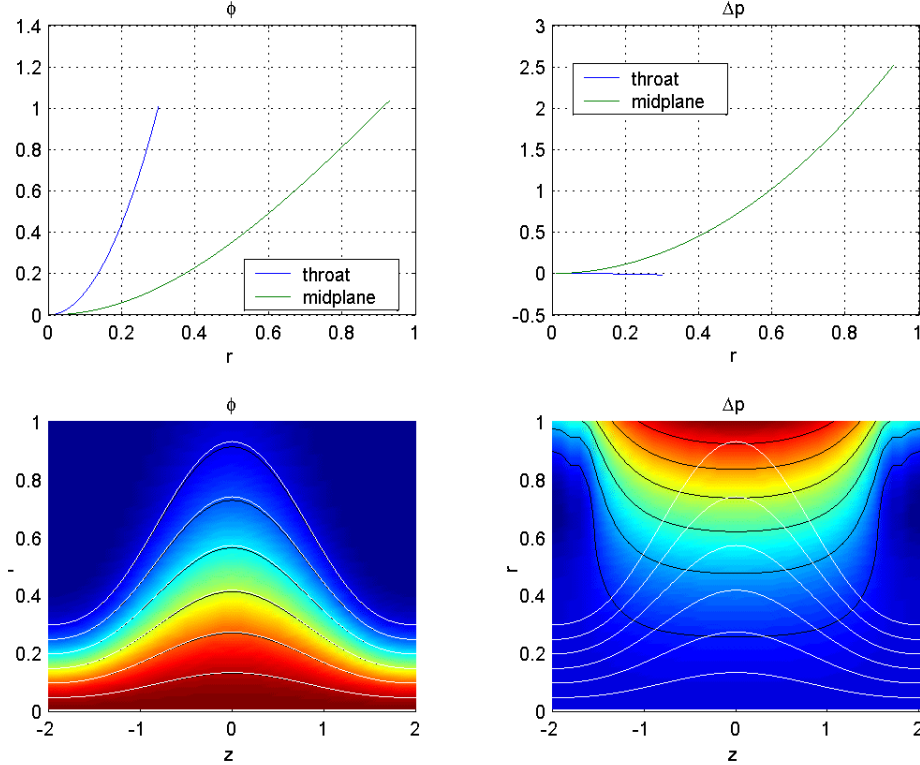


Figure 2.5: Rigid rotation solution for $E_r < 0$ at the mirror throat and present conditions in MBX: $\epsilon \sim 0.025$, $\phi_0 \sim 250$ V, $E_0 \sim 10^3$ V/m, $M_i \sim 1$, so that $V_0 \sim 2.5 \cdot 10^4$ m/s and $M_A \sim 3 \cdot 10^{-3}$. At the top the electric potential and pressure at the throat and equatorial plane as function of radius. At the bottom electric potential and pressure as function of (r, z) combined with magnetic lines (white) and equipotential contours (black).

tential starting at some magnetic line at the throat displaces radially outward

from the magnetic flux in the bulk of the plasma, with a maximum at the outer surface on the equatorial plane, the opposite is true for the positive electric field case. This can be understood considering the electron equation along the magnetic lines. The pressure is balanced by the electric potential leading to a Boltzmann distribution. The centrifugal force increases the pressure as we move towards the equatorial plane that in turn increases the electric potential along the magnetic lines.

The asymmetry is schetched in Fig 2.6. When a positive electric field

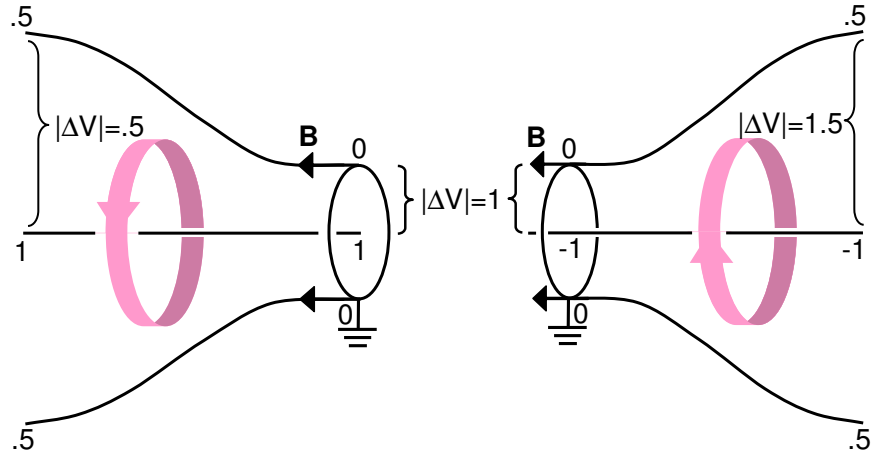


Figure 2.6: Asymmetry in the penetration of the electric potential from the throat to the equatorial plane. The equipotentials displace radially outward (inward) when E_r at the throat is positive (negative).

is present at the throat (left hand side) and the potential remains the same on the axis due to lack of centrifugal confinement the outer magnetic field

line increases its potential when going from the throat to the equatorial plane. Consequently, the potential between this line and the axis at the equatorial plane is less than at the throat. The equipotentials get further apart compared to the magnetic flux. When the electric field is negative (right hand side) the potential at the outer magnetic surface increases and so does the difference in potential at the equatorial plane. This asymmetry is only seen when a 2 fluid model is used to find the solutions.

In the future stage expected in MBX the parameters will be $\epsilon \sim 0.25$, $\phi_0 \sim 2500$ V, $E_0 \sim 10^4$ V/m, $M_i \sim 3$, so that $V_0 \sim 2.5 \cdot 10^5$ m/s and $M_A \sim .6$. The case for positive electric field is shown in Fig. 2.7. The solutions to the boundary conditions for the electric potential and a maximum $\Delta\tilde{p} = 2 \cdot 10^{-2}$ at the throat are $\Omega_e = -2.5$ and $\Omega_i = -2.71$. The current created (maximum of 0.21) is not negligible in this case with 20% of the flow leading to a change in the magnetic flux compared to the external field. The magnetic lines are pushed down by the diamagnetic current a maximum distance $d \sim 0.03$ that corresponds to 0.75 cm. The magnetic lines are far from equipotentials with 0.28 in difference from the throat to the equatorial plane that corresponds to 700 V. This is an important difference compared to ideal MHD solution. The difference in pressure is $\Delta\tilde{p} = 25$. The results are similar when a negative electric field is applied, with $\Omega_e = 2.55$ and $\Omega_i = 2.39$ solution to the boundary conditions. The slight asymmetry in the potential mentioned in the case of $\epsilon = 0.025$ is greatly amplified in this case.

Finally lets consider the case where $\epsilon \sim 1$, $M_A \sim 1$ that could be

reached lowering the external magnetic field by ~ 3 . The solutions are shown in Fig. 2.8. For a negative electric field, $\Omega_e = 2.5$ and $\Omega_i = 2.03$ satisfy the boundary conditions. The effects of non equipotential lines and magnetic flux change due to diamagnetic currents are amplified even more. The difference in

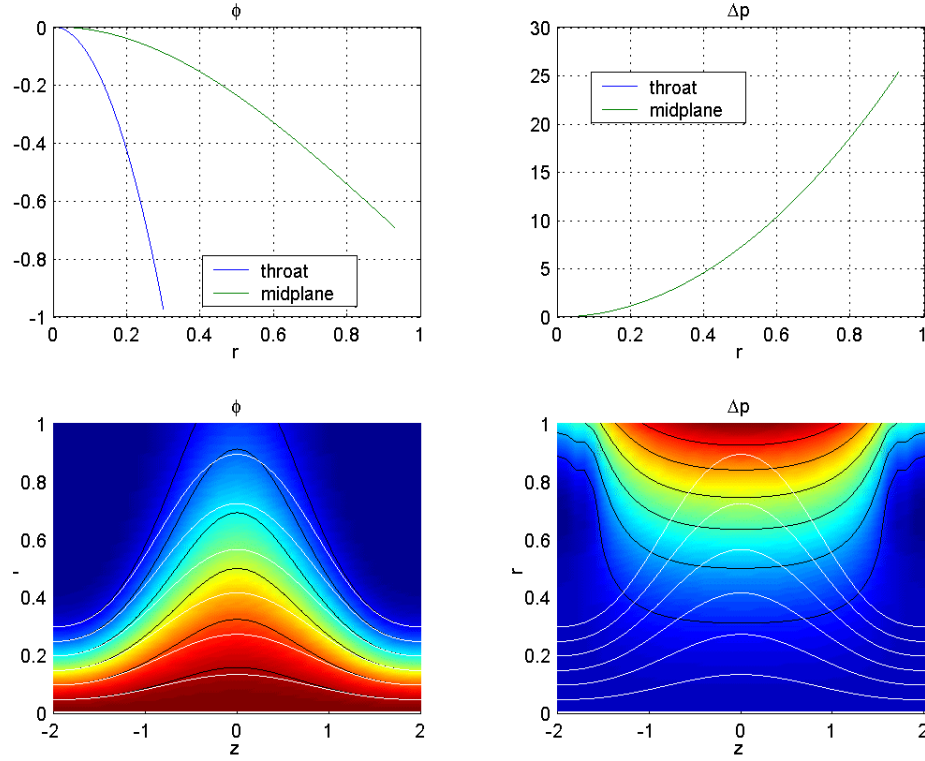


Figure 2.7: Rigid rotation solution for $E_r > 0$ at the mirror throat and future conditions in MBX: $\epsilon \sim 0.25$, $\phi_0 \sim 2500$ V, $E_0 \sim 10^4$ V/m, $M_i \sim 3$, so that $V_0 \sim 2.5 \cdot 10^5$ m/s and $M_A \sim .6$. At the top the electric potential and pressure at the throat and equatorial plane as function of radius. At the bottom electric potential and pressure as function of (r, z) combined with magnetic lines (white) and equipotential contours (black).

potential along the lines reaches a maximum of 0.89, $\Delta\tilde{p} = 14$ and the flux

is pushed down by a distance $d \sim 0.05$. However, for positive electric field there is no solution that can match the boundary condition of zero pressure at the throat. This can be understood considering that the interaction of the ion velocity and the magnetic field in the Lorentz force is not enough to balance the electric and centrifugal forces. That is, for ions at the throat

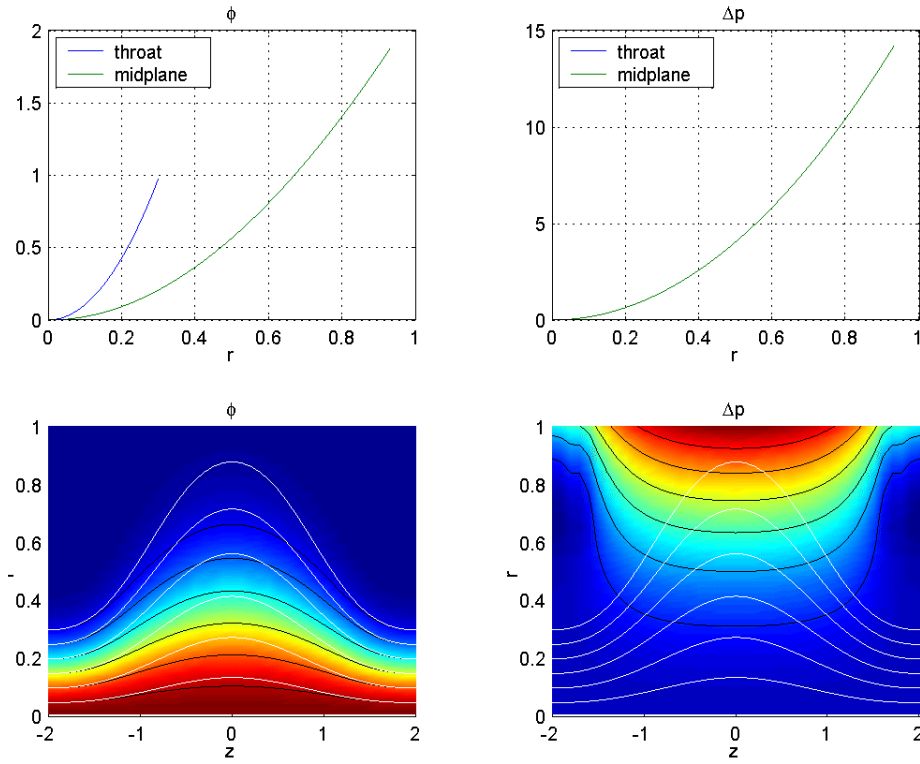


Figure 2.8: Rigid rotation solution for $E_r > 0$ and $\epsilon \sim 1$, $M_A \sim 1$. At the top the electric potential and pressure at the throat and equatorial plane as function of radius. At the bottom electric potential and pressure as function of (r, z) combined with magnetic lines (white) and equipotential contours (black).

assuming constant pressure, the equation of motion in the radial direction and

its corresponding solution are

$$\epsilon\Omega_i^2 + B\Omega + E_r/r = 0 \rightarrow \Omega_i = \frac{B}{2\epsilon} \left(-1 + \sqrt{1 - \frac{4\epsilon}{r}V_E} \right), \quad V_E = \frac{E_r}{B}$$

where V_E is the usual electric drift. In this case the ion drift is affected by the centrifugal force and does not have solutions if $V_E > r/(4\epsilon)$ that can only occur for $E_r > 0$. For $E_r < 0$ the Lorentz force is enough to balance the centrifugal force.

This cut off has being investigated and successfully achieved in a linear machine by the Archimedes Technology Group¹ to use as a method to clean nuclear waste. The cut off depends on the parameter ϵ that is proportional to the ion mass. For the cut off mass and heavier ions the lack of a solution represents expulsion of the particles in the radial direction where they are collected while the lighter ions remain confined to the magnetic field rotating while collected at the throats. This effect in the rotating mirror helps in getting rid of impurities so that a clean plasma is expected.

In summary, we found a region in parameter space where the dissipationless equations are valid and there is a strong coupling between flows and magnetic fields. In this space we located the present conditions of MBX and MCX (away from the strong coupling region) and the future conditions where MBX plans to run (at the edge of the strong coupling region). We reviewed the theory of magnetfluid states and the consequences of using an external magnetic field. In a cylindrical configuration embedded in a constant axial

¹<http://www.archimedestechology.com>

magnetic field the solution is simple. However, when there is a z dependence, like in our mirror field, we have not reached a solution. We also analyzed externally driven mirror plasmas and found solutions that differ from MHD predictions due to the finite ϵ . The solutions show a high increase in the plasma potential from the throat of the mirror to the equatorial plane that creates asymmetry in the system response with respect to the polarity of the externally biasing potential. There is also high centrifugal confinement and the rotational speeds differ from the electric drift V_E . These features become stronger as the plasma speed increases. For positive electric field there is a velocity cut off because the magnetic force is not strong enough to balance the electric and centrifugal force.

2.3 Dissipation equations

Since the plasma configuration achieved in MBX is not dissipationless, there are certain requirements needed from external sources to sustain the rotation in the system. One of the most important inputs is the external current injected when the plasma is biased. The torque created in the plasma by the combination of this current and the poloidal magnetic field balances the neutral drag for a steady state operation.

In order to gain insight of the consequences of some of the dissipative terms and compare their effects with experimental data we simplify the momentum and induction equations (2.12)-(2.13). This will lead to an approximation for the perpendicular resistivity ρ_{\perp} of the system that in a dissipationless

system would be infinite but dissipative terms make it finite.

In order to simplify we consider a steady state ($\partial_t = 0$), symmetric about $\hat{\mathbf{z}}$ ($\partial_\theta = 0$), and homogeneous in the z direction ($\partial_z = 0$) so that the mirror transforms in a straight cylinder with constant magnetic field in the $\hat{\mathbf{z}}$ direction. We also consider no viscosity, the perpendicular velocity of the fluid much less than the toroidal ($V_r \ll V_\theta$) and the pressure term is dropped. These last two approximations lead to equations that do not have variation in the r direction forming an algebraic system. Eqs. (2.12)-(2.13) in the r and θ direction become

$$-\frac{V_\theta^2}{r} = \epsilon^{-1} \frac{J_\theta B}{n} - \alpha V_r \quad (2.46)$$

$$0 = \epsilon^{-1} \frac{J_r B}{n} + \alpha V_\theta \quad (2.47)$$

$$E_r + V_\theta B = \frac{J_\theta B}{n} + \zeta J_r - \delta V_r \quad (2.48)$$

$$V_r B = \frac{J_r B}{n} - \zeta J_\theta + \delta V_\theta \quad (2.49)$$

where $\alpha = C_{D,in}$, $\gamma = C_{H,e}^{-1}$, $\delta \sim \epsilon \alpha \sqrt{m/M}$, and $\xi = \gamma + \delta$, all less than unity quantities. The first equation shows the balance between the toroidal current force to hold the centrifugal force exerted by the rotation plus any possible friction due to radial motion. The second equation shows that the perpendicular currents sustain the rotation against the neutral drag on the fluid. This current is driven by the external power supplies that we measure. The fourth equation states that if the dissipative terms on the electrons are small, then the radial current is carried entirely by the ions while the electrons stay tied to the magnetic field lines.

For a defined position r the last set of equations yields a quadratic form for the toroidal velocity

$$\epsilon \frac{V_\theta^2}{r} + bBV_\theta + cE_r = 0 \quad (2.50)$$

where $c = \frac{1+\xi\alpha\epsilon n/B^2}{1+\delta\xi/B^2}$ and $b = c \left(1 + \frac{\xi\alpha\epsilon n + \delta(\delta-\alpha\epsilon)}{B^2} \right) + \frac{\epsilon\alpha(\epsilon\alpha-\delta)}{B^2}$. In the case where dissipative terms are much less than unity then $c \sim 1$ and $b \sim 1$ so that the equation simplifies to the usual electric drift $V_E = E/B$ modified by the inertia term that has a weight of ϵ . The magnetic field squared accompanies all the dissipative terms, so that the larger the magnetic field the less the dissipation modifies the toroidal motion.

The solutions to the quadratic equation are of the form

$$V_\theta = \frac{-bB \pm \sqrt{(bB)^2 - 4crE_r/\epsilon}}{2\epsilon/r} \quad (2.51)$$

where we choose the positive branch solution that corresponds to lower rotations (the negative branch leads to cyclotron motion).

Fig. 2.9 shows the solutions for the present conditions in MBX (see Table 2.1): $\epsilon = 0.025$, $L_0 = 0.25$ m, $E_0 = 10^3$ V/m, $B_0 = 0.04$ T, so that $V_0 = 2.5 \cdot 10^4$ m/s. The dissipative coefficients are: $\alpha < 1$, $\gamma \sim 5 \cdot 10^{-6}$, $\delta \sim 10^{-4}$ so that $\xi < 10^{-4}$. The neutral drag coefficient α varies linearly from 1 (red) to 0.01 (blue). The solutions for the toroidal motion correspond closely to dissipationless results, $\epsilon V_\theta^2/r + BV_\theta + E_r \sim 0$ and $J_\theta \sim -\epsilon V_\theta^2/r$. The current is always negative, diamagnetic, because it balances the centrifugal force that points in $\hat{\mathbf{r}}$ independent of the direction of the rotation. The perpendicular current is carried mostly by ions so that $V_r \sim J_r \sim -\alpha\epsilon V_\theta$.

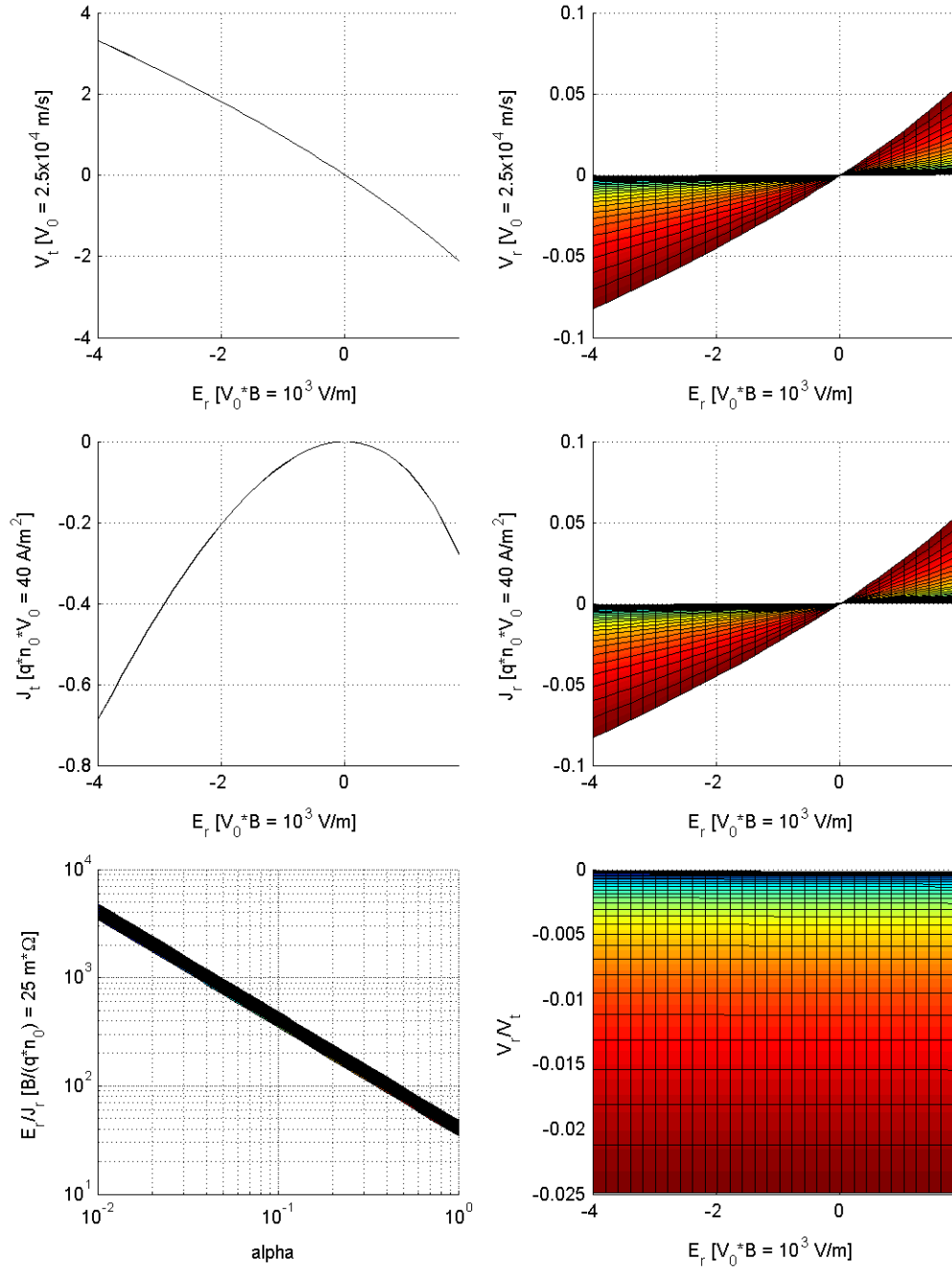


Figure 2.9: Cylindrical solution for a rotating plasma with dissipation in MBX present conditions: $\epsilon = 0.025$, $L_0 = 0.25$ m, $E_0 = 10^3$ V/m, so that $V_0 = 2.5 \cdot 10^4$ m/s and $M_A = 3 \cdot 10^{-3}$.

The external requirements are proportional to the neutral drag that appears as the main mechanism of dissipation. At the same time V_r turns out to be an order of magnitude less than unity in agreement with our initial assumption. Since the perpendicular current is linear with α , the perpendicular resistivity ρ_{\perp} is inversely proportional α , that is, the more neutral drag, the more drift in the perpendicular direction and a less resistive plasma. Typical values obtained are $\rho_{\perp} \sim 2.5 \text{ k}\Omega\text{m}$. This value will be compared to the experimental results.

Fig. 2.10 shows the solutions for the future conditions in MBX (see Table 2.1): $\epsilon = 0.1$, $L_0 = 0.25 \text{ m}$, $E_0 = 4 \cdot 10^3 \text{ V/m}$, $B_0 = 0.04 \text{ T}$, so that $V_0 = 10^5 \text{ m/s}$. The dissipative coefficients are: $\alpha < 1$, $\gamma \sim 7.5 \cdot 10^{-4}$, $\delta \sim 7.5 \cdot 10^{-4}$ so that $\xi < 10^{-3}$. The behavior of the solutions in dimensionless form are close to present parameters in MBX (Fig. 2.9) with one exception. The velocity is cut off when the electric field is positive and in this case $E_r = 1$ in dimensionless quantities that corresponds to $4 \cdot 10^3 \text{ V/m}$. This cut off is the same as the one appearing in Section 2.2.3 for the rigid rotation case. Negative electric fields do not present the cutoff and the velocity differs by 25 % from the electric drift V_E when $E_r = -2$. The perpendicular resistivity decreases by a factor of 10^3 due to the increase in the plasma density, considering the same neutral density as in the present conditions.

In summary, after simplifying the magnetic field geometry to a constant axial field we found the perpendicular resistivity of the rotating plasma. This resistivity appears mainly due to the neutral drag force in the azimuthal

direction so that an $\mathbf{I} \times \mathbf{B}$ force is required to balance it. The current \mathbf{I} is the external requirement to rotate the system. The perpendicular resistivity for the present conditions will be compared to the experimental data in Section 5.6. For future conditions, an estimate of the perpendicular resistivity is given, however we expect the pressure gradient to be too large (Section 2.2.3) to be dropped as we did in this section to find an analytical solution.

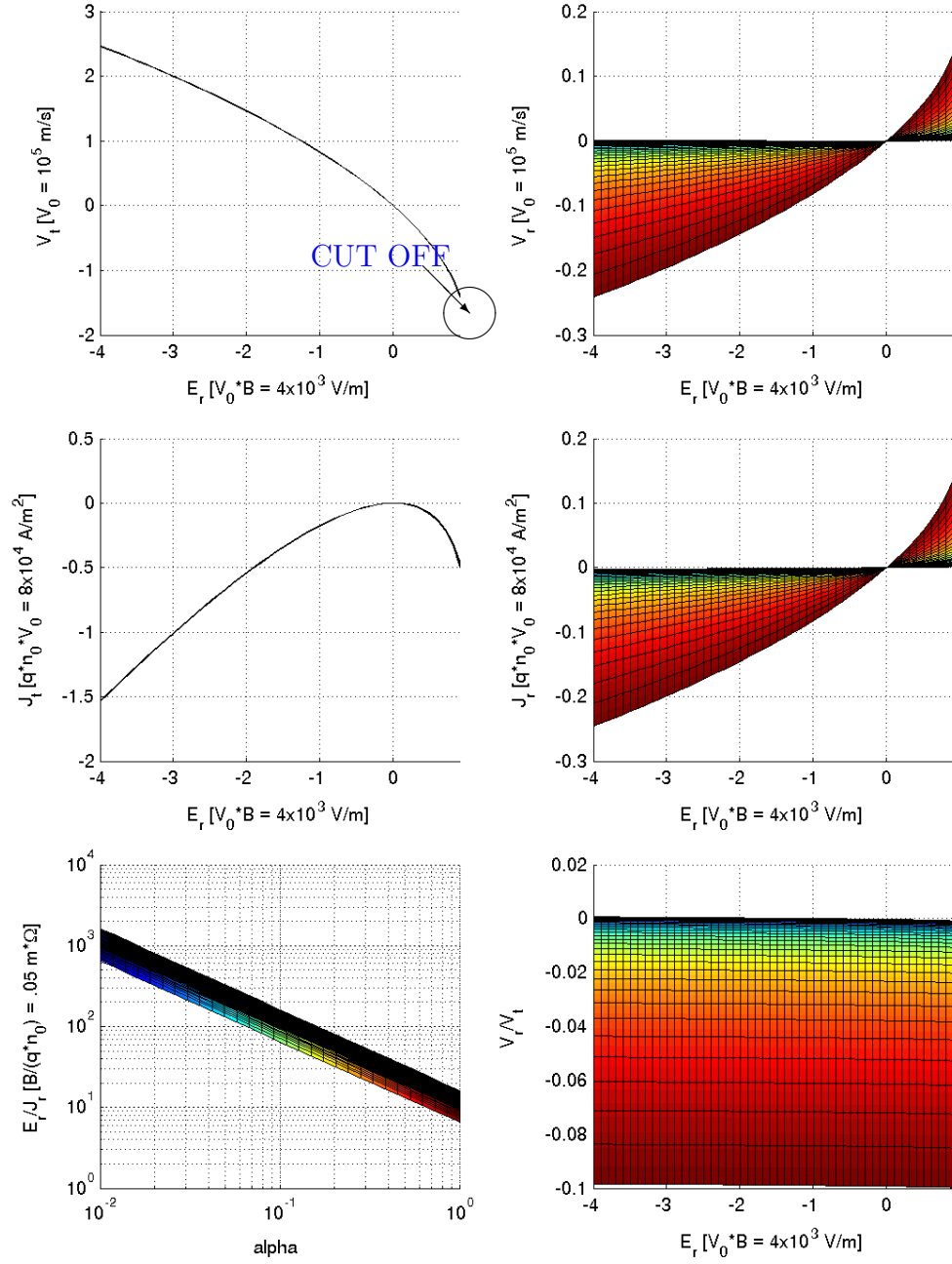


Figure 2.10: Cylindrical solution for a rotating plasma with dissipation in MBX future conditions: $\epsilon = 0.1$, $L_0 = 0.25$ m, $E_0 = 4 \cdot 10^3$ V/m, so that $V_0 = 1 \cdot 10^5$ m/s and $M_A = .25$.

Chapter 3

Experimental Setup

The goal of the experiment is to create a plasma that can be driven to high speeds so that there is the possibility of creating a magnetofluid state. Typical magnetofluid parameters are densities such that the ion skin depth λ_i is of the order of the size of the machine L , and velocities higher than 10 % of the Alfvén speed V_A . The steps that we follow to achieve a fast, supersonic rotating plasma are shown in Fig. 3.1.

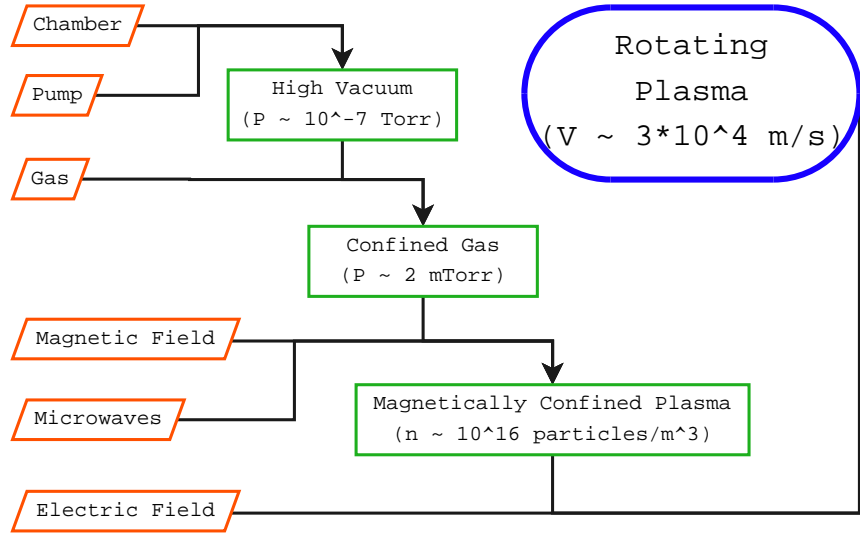


Figure 3.1: Steps followed to create a high speed, supersonic rotating plasma.

Since MBX is a low-budget device, some of the choices in the creation of such a rotating plasma state are based on existent material such as a vacuum chamber, microwaves, that have been inherited from older experiments in the laboratory.

A turbomolecular pump is connected to a stainless steel vacuum chamber to achieve a high vacuum inside of it $\sim 10^{-7}$ Torr. Hydrogen is added to the chamber at a pressure $\sim 10^{-4}$ Torr and will become the main component of the plasma. Magnetic coils external to the vessel run continuously to create an axisymmetric mirror magnetic field $\sim .04$ T at the equatorial plane of the chamber. Electromagnetic waves at a frequency $f = 2.54$ GHz are injected into the vacuum chamber through a glass window and, in combination with the gas and the magnetic field, create a magnetically confined plasma. Electrodes inside the chamber are biased at high potential, ~ 1 kV, to set up an electric field \mathbf{E} that in conjunction with the mirror magnetic field creates a fast, supersonic rotating plasma.

A detailed explanation of each of these steps follows in the next sections.

3.1 Vacuum Chamber

The vacuum chamber is one of the main components of the experiment because it allows the generation of a high vacuum environment with base pressures $\sim 10^{-7}$ Torr and low impurity levels, where the plasma can be created and rotated. It was originally designed for the TEXMEX project in the machine shop of the Physics Department, University of Texas at Austin in 1997.

The chamber is made out of 304 stainless steel. It is cylindrical in shape, and contains 36 ports of different sizes, from 1.5 in. to 20 in. diameter, for the different plasma diagnostics. The volume of the chamber is approximately 0.46 m^3 and its dimensions are shown in Fig. 3.2.

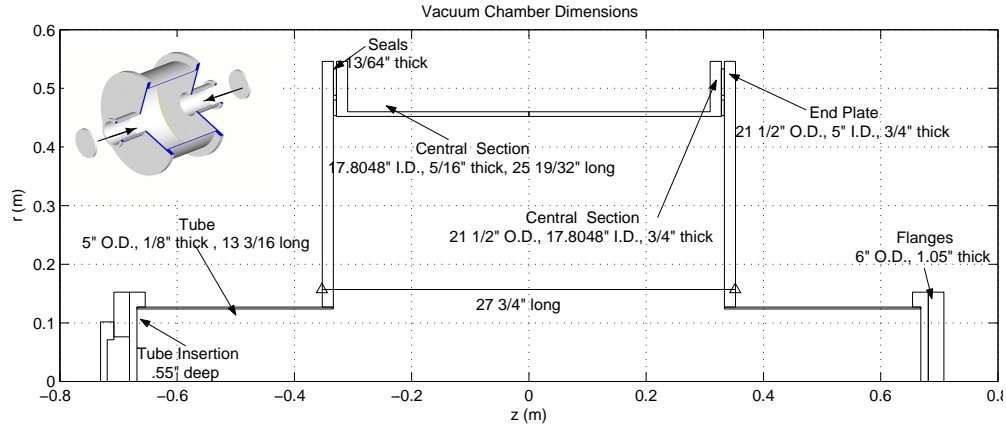


Figure 3.2: Vacuum chamber dimensions, symmetric around the z axis.

The chamber consists of a central section 0.9 m inner diameter, 0.65 m long and 7.5 mm thick sealed by O-rings to a 21.5 in. outer diameter and 3/4 in. thick circular plates on each side. Each disk is welded at its inner diameter to one end of a 5 in. diameter, 0.335 m long and 1/8 in. thick stainless steel tube. The other end of the tube is sealed using 12 in. Huntington flanges. Around these two identical tube sections is where the magnetic coils are located generating the throats of the mirror magnetic field (Section 3.3). The ports are located around the main section and on the faces of the plates.

The vacuum chamber is connected to a turbo molecular pump Leybold-

Heralus Turbovac 360 (360 liters/s) at the bottom port through an air operated gate valve, shown in Fig. 3.3.

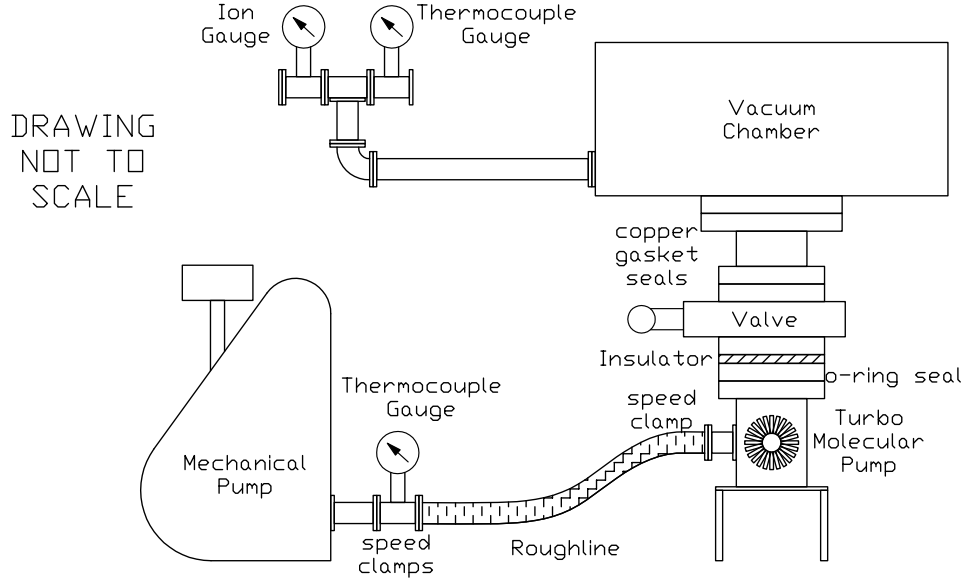


Figure 3.3: Vacuum pump system diagram.

The valve is connected with a copper gasket to the chamber while an O-ring creates the seal between the pump and the valve. An insulator electrically isolates the pump from the vessel. This pump requires neither oil for lubrication nor water for cooling thanks to its ceramic bearings and is able to achieve a base pressure of 10^{-7} Torr inside the chamber. This is a high vacuum considering the small size of the pump and the large size of the chamber, which suggests a small leak and out gassing rate. In order to operate the turbo molecular pump, its exit port must be at a pressure < 100 mTorr.

Then, a mechanical pump is connected with speed clamps to the exit of the turbo pump through a roughing line made out of plastic. This pump requires oil and creates a pressure of 40 mTorr in the roughing line when the turbo molecular pump is not operating.

3.2 Gas

The gas used in the vacuum chamber to generate the plasma is primarily hydrogen. Sometimes, argon is injected at low pressures, as an impurity, for spectroscopic purposes. The choice of hydrogen is based on the following advantages:

- The ion Larmor radius is much smaller than the size of the machine so that the plasma can have a fluid description, in which magnetofluids are based.
- The ion skin depth λ_i is the size of the machine and is the characteristic length that appears in magnetofluid states.

However one important disadvantage is that since the hydrogen ion is just a proton, there are no transition lines in the visible that can be observed with a spectrometer to infer the speed of the plasma using their Doppler shift. Doppler measurements can only be done with transition lines from impurities or hydrogen atoms after going through a charge exchange process.

The injection of hydrogen in the vacuum chamber is shown in Fig. 3.4. The gas is introduced into the vacuum chamber using a feedthrough at the

side of the central section of the chamber and a needle valve regulates the flow into it. An extra valve follows the line to completely block the gas flow when the machine is not operating. This valve is connected to the gas tank through another piece of line. A similar system is available to introduce other gases as impurities.

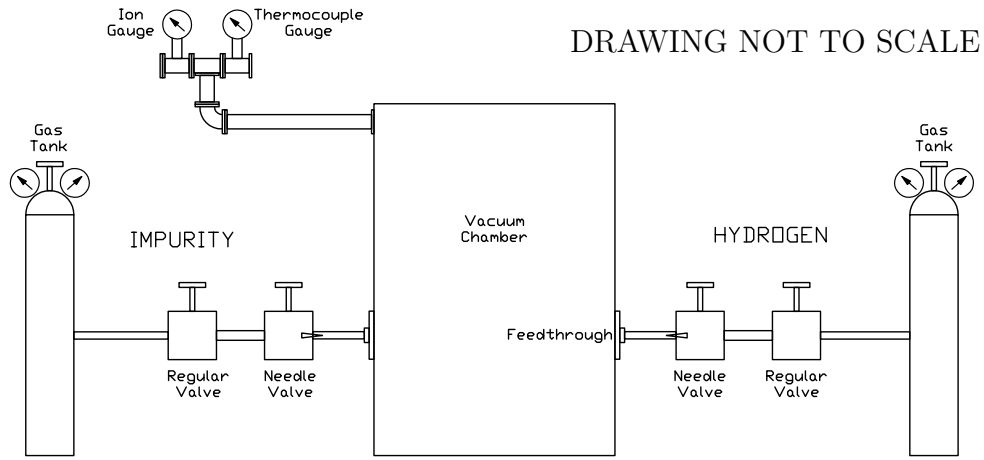


Figure 3.4: Schematic of the gas injection system.

The neutral pressure inside the vacuum chamber is measured with an ion and a thermocouple gauge that are connected through a long L-shaped tube to the chamber to avoid the plasma from reaching it and affecting the measurements. The range of pressures measured by the Granville-Phillips Series 270 using a nude Bayart-Alpert ion gauge is (10^{-3} to 10^{-8}) Torr, while using a Huntington thermocouple 6000 is (1 to 10^{-3}) Torr. Another thermo-

couple gauge measures the pressure in the roughing line located between the turbo molecular and the mechanical pump (Fig. 3.3). It is used to find out when the line reaches a pressure of 40 mTorr with only the mechanical pump operating so that the turbo molecular pump can be turned on. The maximum pressure that can be achieved with the turbo pump operating without the use of a variable gate valve between the chamber and the pump is 1 mTorr. The ionization gauge is originally calibrated for N_2 , then the pressure of the working gas is obtained after multiplying the read out pressure by a factor K that depends on the gas. In the case of hydrogen $K_{H_2} = .46$, helium $K_{He} = .18$ and argon $K_{Ar} = 1.29$ [11].

3.3 Magnetic Field

The main magnetic field is created by external coils to the vacuum chamber and has the configuration of an axisymmetric mirror bottle. The purpose of the field is to generate a natural magnetic confinement of the plasma in the radial direction as well as in the axial direction through the conservation of the magnetic moment of the particles. It also allows relatively easy biasing of the magnetic surfaces with electrodes for plasma rotation and enhancement of axial confinement through centrifugal forces [24].

The magnetic field is generated by 6 water cooled coils connected in series to a DC power supply so that the current, measured by a shunt, is the same in all of them. The maximum current delivered to the coils before they dangerously heat up is ~ 1200 A for about 30 s generating a field strength

~ 0.1 T on the axis at the throat. The coils can run continuously with currents smaller than 700 A. The position and orientation of the coils are physically aligned respect to the chamber to create a mirror ratio $R = \frac{B_{throat}}{B_{center}} = 7.4$, that is maximized to achieve the strongest confinement in the axial direction. They lay on the axis of symmetry of the vacuum chamber with their planes perpendicular to it, 3 coils on each side. Each coil has 2 sets of spiraling copper stripe, separated along the axis of symmetry by 0.05 in. Each spiraling copper stripe consist of 32 concentric turns separated radially by 0.003175 in., with the innermost (outermost) turn having a radius of curvature equal to 0.15 (0.27) m. The resulting axisymmetric magnetic field lines, magnetic intensity surfaces, and the position and radii of the coils turns are shown in Fig. 3.5 after some approximations explained in the next paragraph are made.

The magnetic field \mathbf{B} and its vector potential \mathbf{A} are calculated with a code developed by the author in Matlab language¹. We use the assumption that the coil can be modeled as a set of concentric loops because the thickness of the copper strip is much smaller than the turn radius. At the same time, the current generating the magnetic field can be considered only in the azimuthal direction θ neglecting the small drift of the current in the r direction to go from the inner to the outer winding. Under these assumptions the fields are calculated adding the magnetic field generated by each individual circular loop

¹<http://www.mathworks.com>

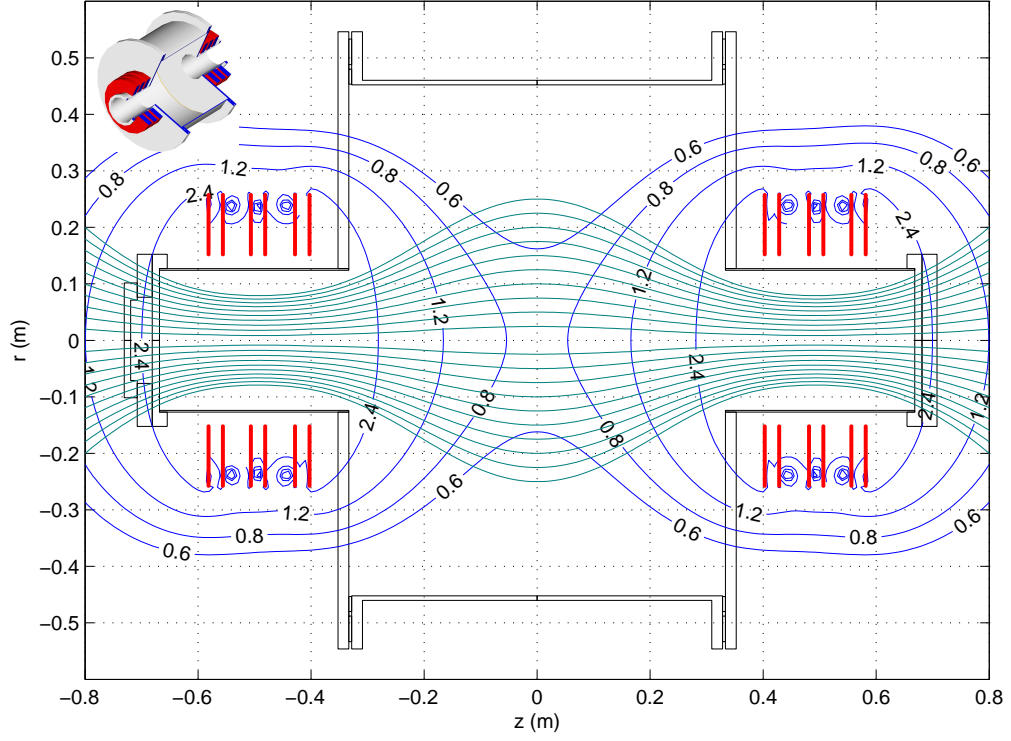


Figure 3.5: Mirror magnetic field configuration symmetric about the z axis. Magnetic field lines (green), $B(\text{G})/I(\text{A})$ (blue), and position and radii of coils windings (red).

as expressed by Eqs. (3.1)-(3.2).

$$\mathbf{A}(\mathbf{r}) = \sum_{i=\text{loops}} \mathbf{A}_i(\mathbf{r}, a_i, \mathbf{r}_{0,i}, I_i) \quad (3.1)$$

$$\mathbf{B}(\mathbf{r}) = \sum_{i=\text{loops}} \mathbf{B}_i(\mathbf{r}, a_i, \mathbf{r}_{0,i}, I_i) \quad (3.2)$$

where \mathbf{r} is the position vector, a_i , $\mathbf{r}_{0,i}$, and I_i are the radius, center position and current of the coil i respectively.

The potential \mathbf{A} and magnetic field \mathbf{B} for a circular loop can be written

in terms of elliptic integrals. Their expressions at a position \mathbf{r} from the center of a circular loop of radius a and current I is given by Eqs. (3.3)-(3.5) [39]

$$A_\theta = \frac{\mu_0 I}{\pi} \frac{1}{k} \sqrt{\frac{a}{r}} \left[\left(1 - \frac{k^2}{2} \right) K(k^2) - E(k^2) \right] \quad (3.3)$$

$$B_r = \frac{\mu_0 I}{2\pi a} \left(\frac{z}{r} \right) \sqrt{b} [-K(k^2) + cE(k^2)] \quad (3.4)$$

$$B_z = \frac{\mu_0 I}{2\pi a} \sqrt{b} [K(k^2) + dE(k^2)] \quad (3.5)$$

where K and E are complete elliptic integrals of the first and second kind, $k^2 = 4b \left(\frac{r}{a} \right)$, $b = \frac{1}{\sqrt{\left(1 + \frac{r}{a}\right)^2 + \left(\frac{z}{a}\right)^2}}$, $c = \frac{1 + \left(\frac{r}{a}\right)^2 + \left(\frac{z}{a}\right)^2}{\left(1 - \frac{r}{a}\right)^2 + \left(\frac{z}{a}\right)^2}$, and $d = \frac{1 - \left(\frac{r}{a}\right)^2 - \left(\frac{z}{a}\right)^2}{\left(1 - \frac{r}{a}\right)^2 + \left(\frac{z}{a}\right)^2}$

An important simplification occurs when we consider the mirror bottle configuration. All the coils, and so the individual loops, have their center on the axis of symmetry $\hat{\mathbf{z}}$. The enclosed surfaces lay on the r - θ plane as seen in Fig. 3.5. In this case, even though the center of the circular loops that constitute the coils are displaced in the z axis, each with a different $z_{0,i}$, and the radii a_i are different, their magnetic fields have only $\hat{\mathbf{r}}$ and $\hat{\mathbf{z}}$ components and depend only on (r, z) . The vector potential is in the $\hat{\theta}$ direction and depends on (r, z) . This simplification leads from Eqs. (3.1)-(3.2) to Eqs. (3.6)-(3.7).

$$\mathbf{A}(r, z) = \sum_{i=\text{loops}} A_{\theta,i}(r, z - z_{0,i}, a_i, I_i) \hat{\theta} \quad (3.6)$$

$$\mathbf{B}(r, z) = \sum_{i=\text{loops}} [\mathbf{B}_{r,i}(r, z - z_{0,i}, a_i, I_i) \hat{\mathbf{r}} + \mathbf{B}_{z,i}(r, z - z_{0,i}, a_i, I_i) \hat{\mathbf{z}}] \quad (3.7)$$

Since all the coils have the same current I and \mathbf{B} is linear with it, a field $\mathbf{G}(r, z) = \mathbf{B}(r, z, I)/I$ can be constructed that depends only on the position and radius of the coils but is independent of the current. The relevance of

this field, specially G contours shown in Fig. 3.5, relies in the fact that the plasma is generated where the cyclotron motion of the electrons resonate with the circularly polarized microwaves (Section 3.4). That is, when the electron cyclotron frequency $\Omega_e = 2\pi \cdot 2.45$ GHz rad, which corresponds to a magnetic field strength $B = 0.0875$ T and $G = 875/I$ (I in amperes).

Another simplification allowed by the axisymmetry is the calculation of the magnetic lines or surfaces shown in Fig. 3.5. Due to $\nabla \cdot \mathbf{B} = 0$, following the magnetic lines keeps the enclosed magnetic flux $\Psi = \iint \mathbf{B} \cdot d\mathbf{A} = \oint \mathbf{A} \cdot d\mathbf{s}$ constant. From (3.6) $\mathbf{A} = A_\theta \hat{\theta}$ due to axisymmetry, then $\Psi = 2\pi r A_\theta$, so that the magnetic field surfaces can be easily calculated from the contour surfaces of rA_θ .

3.4 Microwaves

Electromagnetic waves have been chosen as the mechanism to generate the target plasma with densities of the order of 10^{16} particles/m³. An increase of this density to decrease the Alfvén speeds V_A and ion skin depth λ_i to achieve magnetofluids conditions is expected from ionization due to rotation when the plasma kinetic energy reaches the ionization potential of the gas being used [2], $6 \cdot 10^4$ m/s for hydrogen (Section 5.8). Some advantages in using microwaves respect to other techniques used to generate a plasma, in particular a rotating one, are the following:

- In our case the source of microwaves was already available, inherited

from a previous experiment.

- The plasma density can be controlled by the amount of power injected.
- Microwaves propagating along the magnetic lines do not have a cutoff density limit.
- There is no need for high potential (5 kV) and Paschen [30] restrictions in the neutral density, usually a concern in rotating plasma experiments [8].

The main disadvantages of using microwaves are the following:

- A magnetic field of 0.0875 T is needed for the waves to resonate with the electrons and ionize the filling gas.
- The impedance of the plasma depends on the density so that tuning to achieve low reflection of the microwaves is constantly needed. Even rotation can generate a large mismatch of impedance and detuning as shown in Fig. 3.6.
- Expensive equipment is needed to achieve high densities, ~ 20000 dollars for 6 kW of power to create $\sim 3 \cdot 10^{16}$ particles/m³ in the present machine.
- The output power is very sensitive to the high voltage applied to the source of microwaves. A ripple in the voltage of 1 % can generate fluctuations in the plasma current of 30 % as shown in Fig. 3.6.

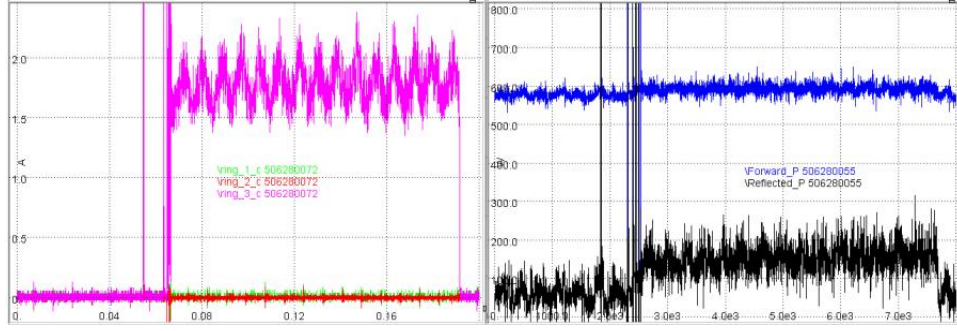


Figure 3.6: On the left hand side, fluctuations in the electrode current between $t_0 = 0.03$ s and 0.18 s due to 120 Hz ripple in the microwave power injected. On the right hand side, detuning of the microwaves, as seen in the reflected power (black), when the plasma is biased and rotating.

The microwave system was built by previous researchers at the Fusion Research Center at The University of Texas at Austin. A schematic of the microwave power system is shown in Fig. 3.7.

A ~ 4 kV DC power supply with a ripple of 1 % is connected to a magnetron National Electronics NL-2555² to deliver a continuous power in the range of (0 to 1) kW. The low ripple appears because of the diode-like response of the magnetron head current and power to the applied voltage. Small ripple in the output voltage of the supply is amplified to generate a higher ripple in the power output of the microwaves and for example in the plasma current as shown in Fig. 3.6. The magnetron head generates 2.45 GHz microwaves that are piped through a 340W rectangular waveguide where only the TE₁₀ mode (cutoff frequency $f_{c,10} = 1.735$ GHz) with a wavelength $\lambda = 0.174$ m

²<http://www.rell.com>

allowing reflected power to reach the magnetron head. The circulator contains three directional couplers. They allow the measurement of the microwave power flux in a particular direction. In our case, there is a coupler measuring the power leaving the circulator towards the plasma, another looking at the reflected power from the plasma reaching the circulator, and a third coupler measuring the power going back to the magnetron. This last one checks the efficiency of the water load in dissipating the reflected power and the possibility of damage of the magnetron head.

After the waves pass the circulator, they are converted to a TEM mode and travel through a semirigid coaxial cable to be converted back to TE_{10} . The coaxial cable allows the launching of the waves through different ports in the vacuum chamber without the need of moving the heavy DC power supply and circulator and allowing different mechanisms of absorption by the plasma. After the transition the microwaves reach a 4 stub tuner with the purpose of minimizing waves travelling back to the circulator and maximizing the power flowing to the plasma. In simple words, the impedance of the tuner is changed varying the length of the stubs so that combined with the impedance of following stage, vacuum window and plasma, generates an impedance as close as possible to that of the 340W rectangular waveguide preceding it, 535Ω [31]. If there is no impedance mismatch at this transition, there is no reflected power at it. After the tuner the waves pass through an air cooled vacuum window made out of glass, mostly transparent to microwaves. The use of high temperature rubber seals allowed heating up of the window without

cracks, something that happened with standard models. The linearly polarized waves enter in the vacuum chamber parallel to the magnetic field. They can be decomposed in left and right handed circularly polarized waves with a dispersion relation for cold plasma given by [40]

$$n^2 = \left(\frac{kc}{\omega}\right)^2 = 1 - \frac{\omega_{pe}^2}{\omega^2} \frac{\omega}{\omega \mp |\Omega_e|} - \frac{\omega_{pi}^2}{\omega^2} \frac{\omega}{\omega \pm \Omega_i} \quad (3.8)$$

where the upper and lower signs correspond to the right and left circularly polarized waves respectively. The right hand polarized waves can travel along the field lines until they resonate with the electrons at the electron cyclotron frequency Ω_e that for a frequency $f = 2.45$ GHz corresponds to a magnetic field $B = 0.0875$ T (Fig. 3.5). The left hand polarized mode is lost or absorbed through a different mechanism.

3.5 Electric Field

To achieve high rotation of the plasma contained in the magnetic mirror bottle an electric field \mathbf{E} perpendicular to the magnetic field surfaces is generated. To the lowest order, an azimuthal drift of the plasma with a velocity $\mathbf{V}_E = \frac{\mathbf{E} \times \mathbf{B}}{B^2}$ is created by these two fields as shown in Fig. 3.8. This method has been successfully used in many experiments in the past [24] and present [8] with certain limitations and relays in the way the electric field is generated either by biasing the plasma at the ends, mirror throats in our case, or at the axis of symmetry.

The approach that we use to create the perpendicular electric field is

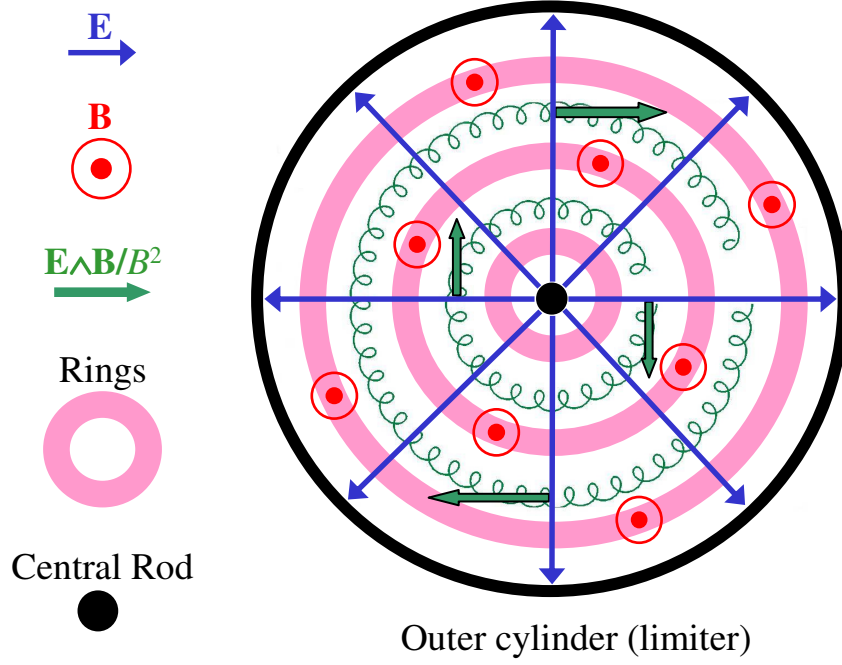


Figure 3.8: Schematic of the $\frac{\mathbf{E} \times \mathbf{B}}{B^2}$ mechanism to rotate plasma.

to assume that the conductivity of each magnetic surface is much higher than the one between them due to the high mobility of electrons along the field lines. Then, biasing different magnetic surfaces at different potentials would create the desired field. Fast rotation, about $2.5 \cdot 10^4$ m/s, can be achieved in a 0.04 T magnetic field with an electric field $E = 10^3$ V/m.

In order to bias the magnetic surfaces, electrodes at one throat of the mirror are biased against the chamber and limiter as shown in Fig. 3.9. Even though the magnetic lines could behave as equipotentials, they do not acquire

the electrodes potential due to the thin sheath formed around them. This sheath can play an important role in the penetration of the potentials into the plasma and in the overall rotational velocity (Section 5.3).

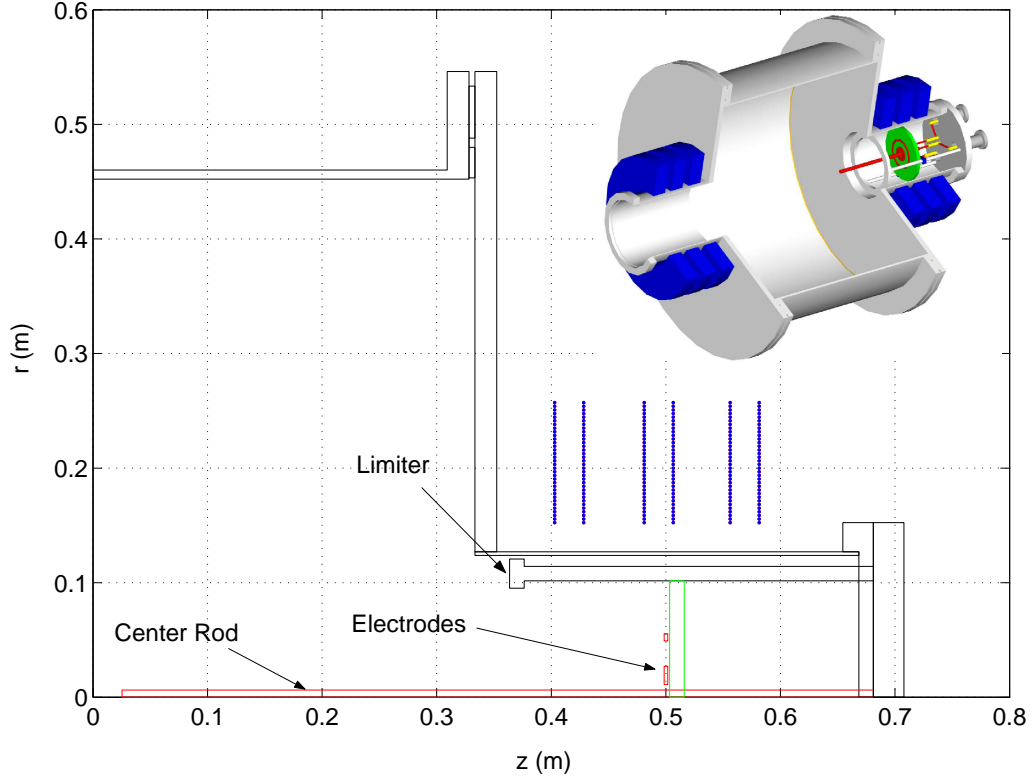


Figure 3.9: Schematic of one type of electrode configuration showing the electrodes (red), insulator (green), chamber and limiter (gray-black).

Insulators at the throats avoid the contact of the plasma with the electrically conducting end walls and the consequently shorting of the magnetic lines to the grounded chamber. Originally the material used was Teflon, but its performance was far from acceptable in our configuration, because it would

melt under some operating conditions. Also Teflon made a dirt plasma. We solved the problem using boron nitride grade AX05 from Saint-Gobain Ceramics³ with a cost of 800 dollars per disk.

High voltage (20 kV) and high current (150 A) feedthroughs ISI⁴ connect the electrodes inside the vacuum chamber to the power supplies outside.

Different electrodes configurations have been used as well as different materials. Electrodes made out of aluminum tend to heat up and deform after many shots with currents of 5 A for 0.4 s as shown in Fig. 3.10 - left hand side. Electrodes made out of 304 stainless steel under the same conditions do not present this problem, no damage has been seen after a thousand shots (Fig. 3.10 - right hand side).

Different configurations of electrodes used in this experiment are shown in Fig. 3.11. Initially bolts were used to bias different magnetic surfaces (Fig. 3.11 - top left hand side) without satisfactory results because the applied potential would not penetrate into the plasma. A center rod [8] that reached the equatorial plane was used next with similar results (Fig. 3.11 - top right hand side). The area of the electrodes perpendicular to the magnetic field turned out to be an important factor in the current drawn and the speed of the plasma achieved (Section 5.3). A third configuration was used with a center electrode and concentric rings [1] with better results due to the bigger collecting area (Fig. 3.11 - bottom left hand side). In this case there was

³<http://www.bn.saint-gobain.com/>

⁴<http://www.insulatorseal.com>

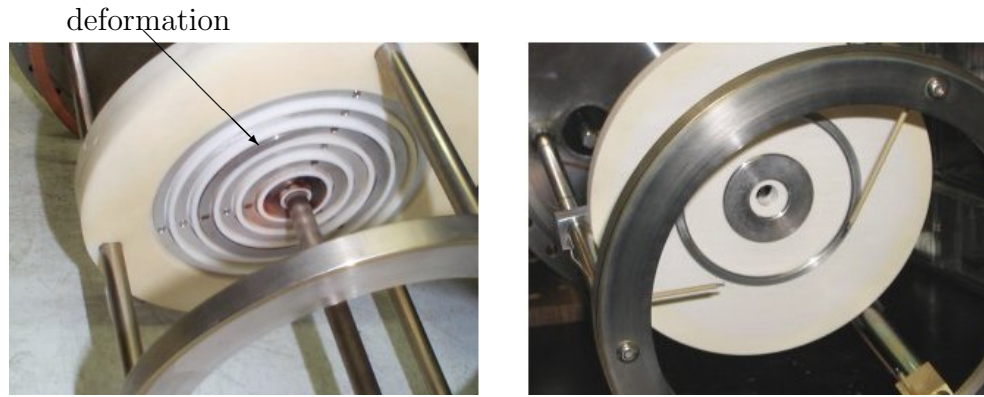


Figure 3.10: Deformation of aluminum electrodes after many shots with currents of 5 A for 0.4 s (left hand side) and no deformation of 304 stainless steel electrodes under the same conditions (right hand side).

a partial control of the potential profile. A last configuration using a single plate was used to maximize the collecting area (Fig. 3.11 - bottom right hand side) with satisfactory results but loosing the possibility to directly control the potential profile.

Originally low voltage (< 200 V) power supplies were used with currents ~ 4 A. The fact that the potential did not penetrate as much as it was desired led to the modification of the original electrodes to achieve more current to drive the plasma. These requirements led to the use of a 1 kV-80 mF capacitor bank with an energy of 32 kJ. 60 Hz Variacs have also been used with voltages of 330 V peak to peak and 10 A of current for multiple electrode biasing.

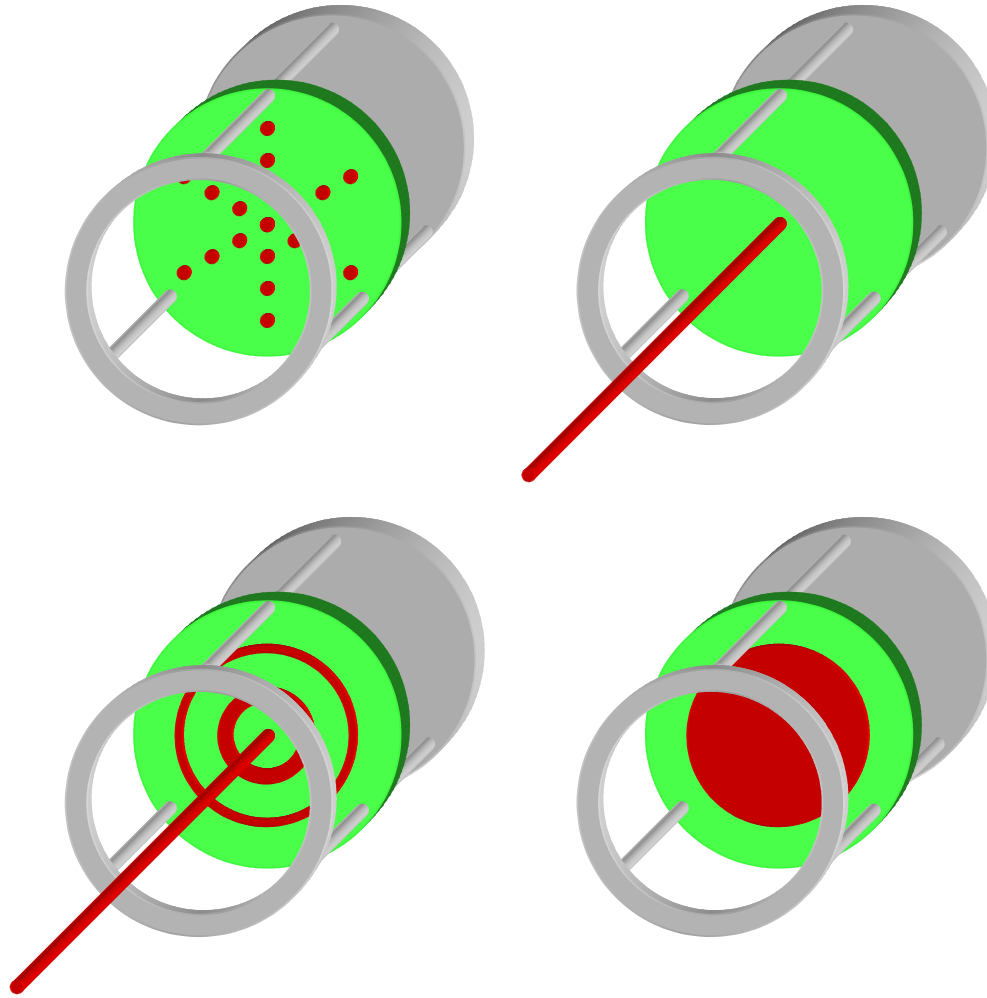


Figure 3.11: Different electrode configurations used in MBX. Bolts (top left hand side), center rod (top right hand side), center rod and rings (bottom left hand side) and single plate (bottom right hand side).

Chapter 4

Plasma Measurements

Once the rotating plasma has been created (Chapter 3) measurement of the plasma such as density, potential, velocity, are needed to characterize its state. These properties are measured directly using different diagnostics or indirectly using theoretical models based on experimental data. The steps followed to characterize the state of the plasma are shown in Fig. 4.1.

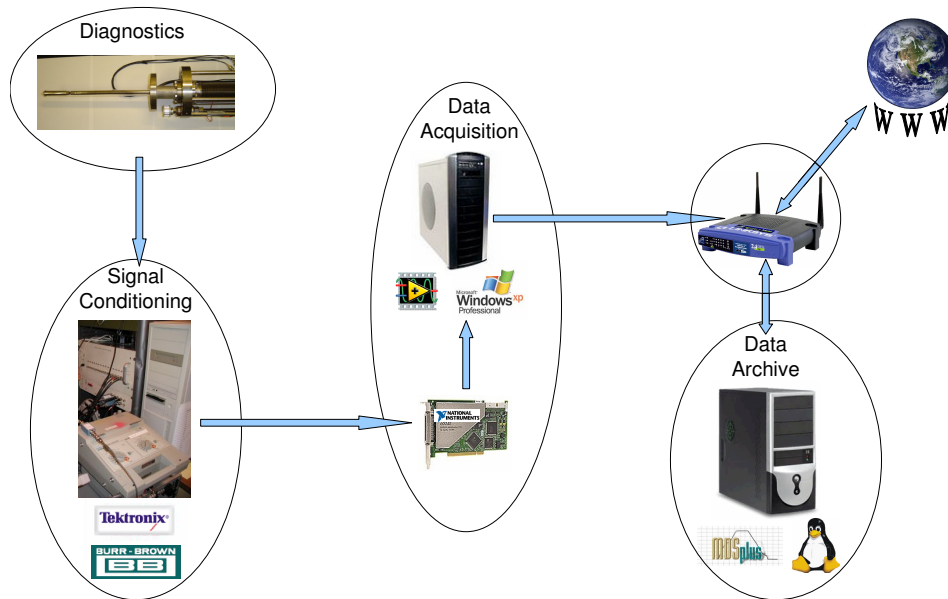


Figure 4.1: Steps followed to characterize the state of the plasma.

Different diagnostics such as floating, current, Langmuir probes are used to interact physically with the plasma while others such as spectrometer and photodiodes are non intrusive. Generally, the signals generated by the diagnostics are in the form of voltages. They are passed through conditioning devices that filter, amplify, and/or isolate them, to finally reach data acquisition boards located in a generic computer. Labview software run by the user tells the boards when to acquire signals and how to digitize them so that they can be stored in a hard drive. The digitized data is then transferred and saved in a computer that acts as an archive where it can be accessed by users worldwide. Finally, the data is analyzed to calculate the properties that characterize the state of plasma such as density, potential, rotational velocity, and so forth.

A detailed explanation of each of the diagnostics used in the present experiment as well as the different steps to condition the signals, acquire, store and process the data follows in the next sections.

4.1 Diagnostics

4.1.1 Langmuir/Mach Probe

The Langmuir/Mach movable probe is actually two different types of invasive probes arranged together. The Langmuir probe is designed to measure the density n , electron temperature T_e , and plasma potential V_p [21]. The Mach probe, very similar in design to the Langmuir probe, measures the plasma velocity V for speeds less than the sound speed c_s after which the theory is

not as clear [13].

The probe is located at the equatorial plane and is able to scan the whole radial extension of the plasma. Each radial position measurement corresponds to a different shot and since the probe does not perturb the plasma appreciably as inferred from measurements of other quantities, a full radial profile can be obtained for the same plasma conditions.

In a typical Langmuir probe the plasma particle flux is collected biasing a metal tip inserted in the plasma. The measurement is local which means that an understanding of how the probe perturbs the plasma around it is necessary to calculate the plasma quantities away from the probe, typically tenths of Debye lengths. Different external potentials V_0 applied to the probe generate different currents I collected by it. Many theories have been derived with different degrees of complexity to explain their dependence. Specifically for our case, the characteristic curve for a cylindrical probe inserted in a low density plasma where the presheath is collisionless and the ions are cold is given by Eqs. (4.1)-(4.4) [21]

$$I = I_{i,sat} \left[\left(\frac{e^{\frac{1}{2}}}{2} \sqrt{\frac{2m_i}{\pi m_e}} \right) e^{\frac{V_0}{T_e}} - \frac{A_s}{A_p} \right] \quad (4.1)$$

$$I_{i,sat} = eA_p \sqrt{\frac{T_e}{m_i}} n_{\infty} e^{-\frac{1}{2}} \quad (4.2)$$

$$A_s \simeq A_p \left(1 + \frac{x_s}{a} \right) \quad (4.3)$$

$$\frac{x_s}{\lambda_D} = 1.02 \left[\sqrt{\frac{-eV_0}{T_e}} - \frac{1}{\sqrt{2}} \right]^{\frac{1}{2}} \left[\sqrt{\frac{-eV_0}{T_e}} + \sqrt{2} \right] \quad (4.4)$$

$I_{i,sat}$ is usually referred as ion saturation current, e is the electron charge, m_i

(m_e) the ion (electron) mass, a is the probe radius, A_p the probe area, A_s the effective probe area due to the increase in the sheath thickness x_s , n_∞ the electron density in the bulk of the plasma and λ_D the Debye length. The first term in the right hand side of Eq. (4.1) corresponds to the collection of the electrons consisting of a Maxwellian distribution with temperature T_e while the second term corresponds to cold ions. Usually the increase in sheath thickness is negligible respect to the probe radius. In that case $A_s \sim A_p$ and the ion current saturates to the value $I_{i,sat}$.

The usual procedure to characterize the plasma from the characteristic curve is to first find the floating potential V_f , the potential applied to the probe such that the current is zero ($I(V_0 = V_f) = 0$). Differentiation of Eq. (4.1) considering the expansion of the sheath negligible gives

$$\frac{dI}{dV_0} = \frac{e}{T_e}(I - I_{i,sat}) \quad (4.5)$$

The slope of the linear fit of Eq. (4.5) yields T_e . Once $I_{i,sat}$ is calculated from the saturation of the current n_∞ is obtained from Eq. (4.2) and the plasma potential for a hydrogen plasma turns out to be

$$V_p \sim V_f + 3.34 \cdot T_e \quad (4.6)$$

However, in plasmas like ours the situation is more difficult since saturation does not occur and for a cylindrical probe the expansion of the area is given by Eq. (4.3). A typical $I - V_0$ characteristic curve in non rotating MBX plasma is shown in Fig. 4.2. The floating potential can still be calculated,

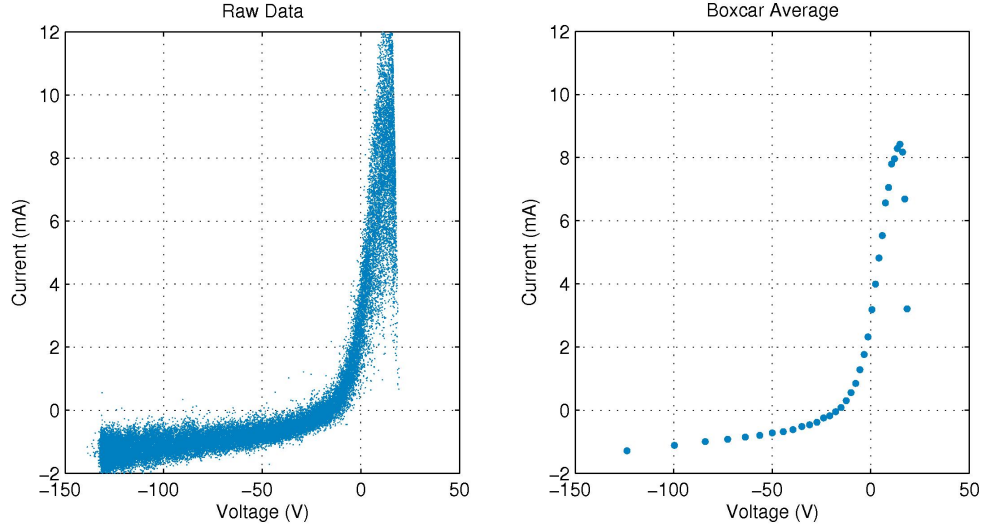


Figure 4.2: Typical Langmuir probe $I - V_0$ characteristic curve for non rotating MBX plasma. The raw data collected is shown on the left hand side while the boxcar average is on the right hand side. The expansion of the probe area can be seen from the increase in $I_{i,sat}$.

as well as T_e around V_f where the sheath has not expanded much. To find n_∞ a full fit of the equations is necessary and the agreement is not always satisfactory.

A typical Mach probe consists of two Langmuir probes separated by a tab that blocks the flux of particles arriving from each hemisphere. In this way each tip collects the flux coming from its own hemisphere. Due to plasma rotation a larger particle flux arrives from upstream (up) than from downstream (down). Measurement of the ion saturation currents collected by the two tips gives an indication of the plasma speed. A widely used theory that relates the ratio in ion saturation currents to the plasma flow in units of

the Mach number M is given by (4.7) [20]:

$$\frac{I_{i,sat-up}}{I_{i,sat-down}} = \exp(KM), \text{ where } M = \frac{V_\theta}{c_s} \quad (4.7)$$

where K is the Mach probe calibration factor that depends on the theory considered and the plasma characteristics. Values for K are between 1 and 4. c_s is the sound speed considering cold ions.

A typical Mach probe measurement in rotating MBX plasma is shown in Fig. 4.3. There is a clear difference in the ion saturation currents collected by both probes. The velocity in this case corresponds to .45 Mach.

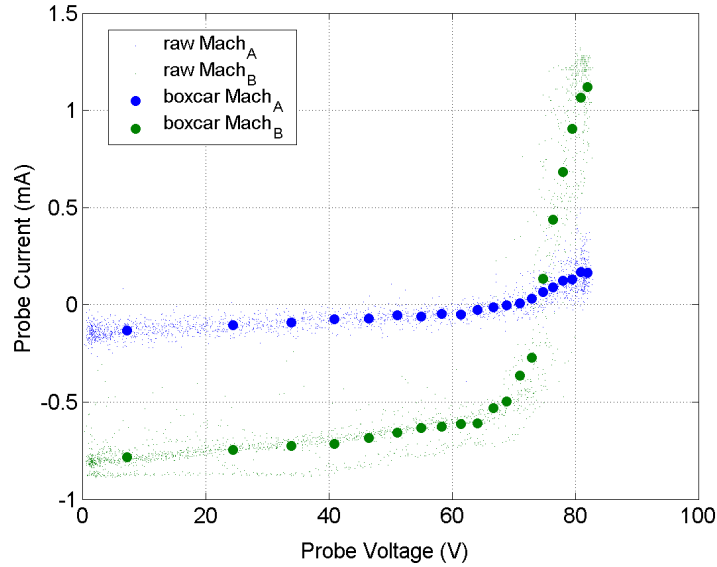


Figure 4.3: Typical Mach probe $I - V_0$ characteristic curve for rotating MBX plasma. Green and blue correspond to the probe facing upstream and downstream respectively. Superimposed is the boxcar average of the signals. The velocity corresponds to .45 Mach.

There are at least two issues involved in the formulas used for the Langmuir and Mach probes:

1. Langmuir probe theory works fine for a non flowing plasma, in our case the base plasma. But when the plasma is rotated, as it is mentioned for a Mach probe, the ion saturation current changes. The decoupling of rotation and increase in density out of the ion saturation current is the difficult task. There are theories that include the effect of a flowing plasma in the Langmuir probe characteristic curve [20]. Then, theoretically, one could measure with the Mach probe the velocity and with this value and the ion saturation current calculate the plasma density.
2. The Mach probe theory works well for subsonic speed but it is not that effective when the flow is supersonic. A presheath is not formed in the upstream tip and no clear theory is available [13].
3. Some cases with high fluctuations in the plasma potential when the plasma is rotating fast create a distorted characteristic curve that is difficult to analyze

The system to bias the Langmuir/Mach probe and measure the current flowing is shown in Fig. 4.4. It consists mainly of three parts: the probe itself, a resistor to measure the current I flowing through the probe and a power supply to bias the probe at V_0 .

The probe consists of 4 Molybdenum tips 1.5 mm diameter and 4 mm long arranged in a diamond pattern held in position by a boron nitride holder

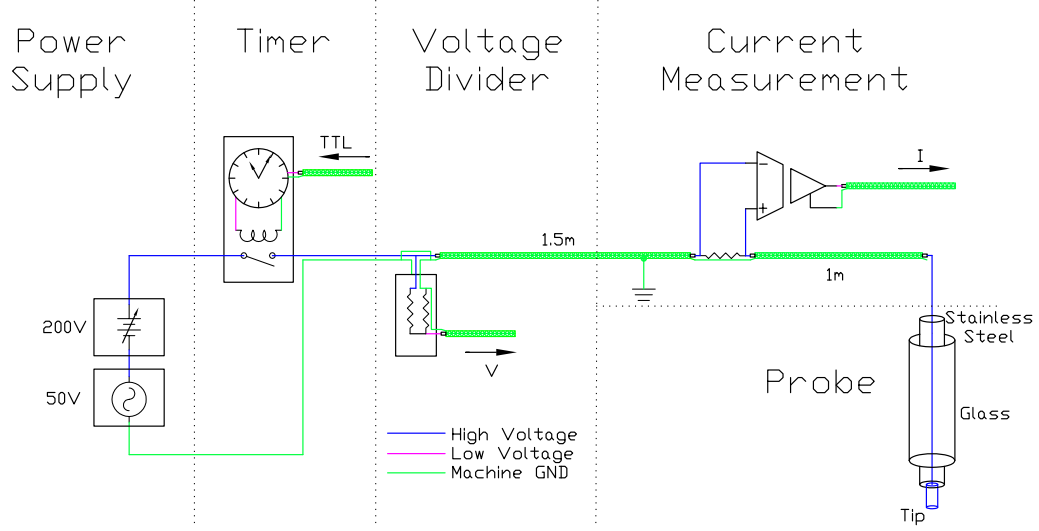


Figure 4.4: Schematic of the system used to bias the Langmuir/Mach probe and measure the collected current.

as shown in Fig. 4.5. The 2 tips along the magnetic field lines act as a Langmuir probe measuring the flux from either hemisphere. The possible difference in ion saturation currents is due to the position of the plasma source (Section 3.4). The two tips perpendicular to the field lines act as a Mach probe. They are meant to measure velocity drifts in the $\hat{\theta}$ direction.

The current I is inferred by the potential measured across the resistor R . There is one resistor for each tip in the probe. Since the Mach probe measures only ion saturation current while the Langmuir probe also collects also electron current to measure T_e , the resistors used for the Mach probe tips is ten times bigger than the Langmuir probe ones. Since the tips are bi-

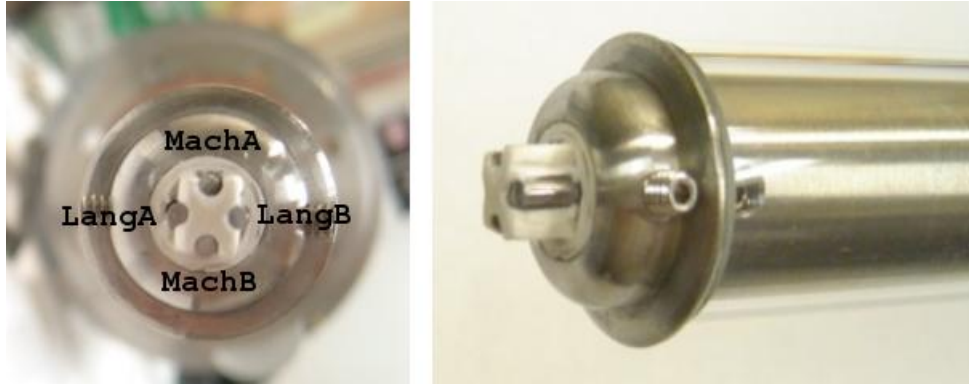


Figure 4.5: Langmuir/Mach probe head.

ased around the floating potential of the plasma to measure the characteristic curve, both ends of the resistor R can be at hundreds of volts. Then, isolation amplifiers are needed, because the data acquisition boards only handle a maximum of 10 V. The isolation amplifiers are specifically designed to extract the small signal across the resistor ~ 1 V from the high common signal ~ 200 V (Section 4.2).

The potential V_0 is applied with an AC in series with a DC power supply respect to the vacuum chamber (ground). The AC scans the characteristic curve while the DC allows the tips to be scanned around the floating potential of the plasma. There is a timing circuit that controls that the bias is applied once the shot has been fired and the plasma is at high potential. A voltage divider reduces the bias voltage in the range that the acquisition boards can measure.

Radial scans of the plasma can be performed fast and accurate using

a probe drive. A TTL signal is sent by the computer activating the indexer Compumotor¹ model 172 that sends a series of square pulses (steps) to the motor controller AH-drive 7464. This in turn drives the stepper motor AX-106-120 and moves the probe up or down by a finite amount, usually 2 cm.

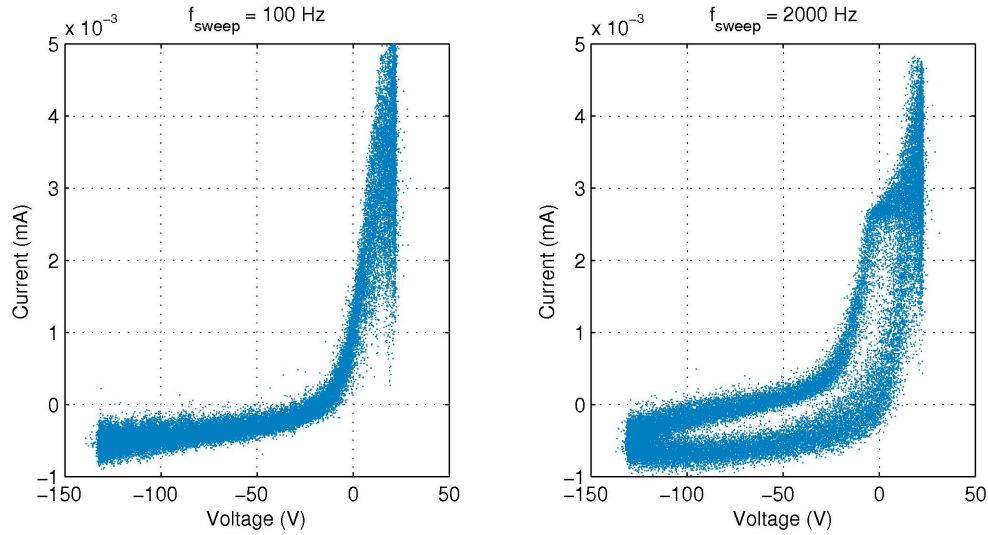


Figure 4.6: Hysteresis in the Langmuir probe measurements as the sweeping frequency is increased.

There are two important issues to consider when biasing the Langmuir/Mach probe:

- The plasma presents hysteresis when AC biased and the effect is worse as the frequency increases as shown in Fig. 4.6. The hysteresis creates a

¹<http://www.compumotor.com>

constraint in the maximum frequency that the plasma can be probed in addition to the limit the minimum frequency that can be used limited by the duration of the shot = 0.4 s.

- The rejection of the sweeping voltage that the isolation amplifier has with frequency degrades as if a stray capacitance was present. The more the frequency or the measuring resistor value the less the rejection. The end result is that there is an upper limit in the frequency used to sweep above which the parasitic current becomes comparable to the current driven by the probe and a hysteresis like curve appears even without plasma.

For the current conditions a 200 Hz sweeping is more than adequate to avoid plasma hysteresis while the parasitic currents are a tenth of the ion saturation currents at the plasma axis. This factor increases when we move away of the axis due to lower densities and ion saturation currents.

A way to measure the density of the plasma and its fluctuations is to negative bias the probes with a DC power supply (instead of sweeping) to collect only $I_{i,sat}$ and from there calculate n_∞ using Eq. (4.2), assuming or already knowing an estimate of T_e . This is not possible in the present conditions where MBX operates. The reasons are that, apart from the increase in $I_{i,sat}$ due to rotation, there is a large expansion of the sheath due to the high plasma potential that makes the current collected far from $I_{i,sat}$ in Eq. (4.1).

4.1.2 Floating Probes

The floating probes are designed to measure the floating potential of the plasma V_f that and the assumption of constant electron temperature. The measurement of this property has many advantages in this particular experiment such as:

- Calculate how much of the external potential applied at the electrodes penetrates the plasma (or drops at their sheaths) which is tightly connected to the speed of rotation.
- Check whether the magnetic field lines are equipotential, a statement often used in the literature due to the high mobility of electrons to claim isorotation of the plasma [24].
- Calculate an approximate value of the electric field \mathbf{E} using the difference in the plasma potential at different locations.
- Compare at subsonic speeds the velocity calculated using the Mach probe to the electric drift $\mathbf{V}_E = (\mathbf{E} \times \mathbf{B})/B^2$ that is a first approximation to the plasma rotational velocity.
- Calculate low supersonic speeds that are not fast enough to be measured by a spectrometer assuming $\mathbf{V} \sim \mathbf{V}_E$.
- Compare at fast supersonic speeds \mathbf{V}_E with the velocity measured with a spectrometer. The difference should give an indication of the centrifugal

force drift [9], relevant quantity for the centrifugal confinement achieved in the mirror due to rotation.

- Study fluctuations in V_f allows the investigation of possible instabilities or flow turbulence.
- High time resolution of the order of the sampling frequency of the acquisition boards compared to the low resolution in time of the Mach probe that is of the order of sweeping frequency.
- One shot captures the potential in the equatorial plane at four places while it would take four shots with the Langmuir/Mach probe.

There are two set of fixed floating probes as shown in Fig. 4.7. The first set of three probes is located near the throat of the mirror field, at a r - θ plane 0.1 m away from the biasing electrodes. The probes are separated by 120° to measure any possible perturbation in the azimuthal direction with correlation lengths longer than 0.2 m. The second set of four probes is located in the equatorial plane of the machine 120° away from the Langmuir/Mach probe. Three of the probes are connected by the same magnetic surface in vacuum to the probes at the throat to check whether the magnetic lines are equipotentials. The forth probe is used to increase the resolution in the radial direction.

Probe tips similar in physical characteristics to the ones in the Langmuir/Mach probe are used to measure the floating potential. The tips are

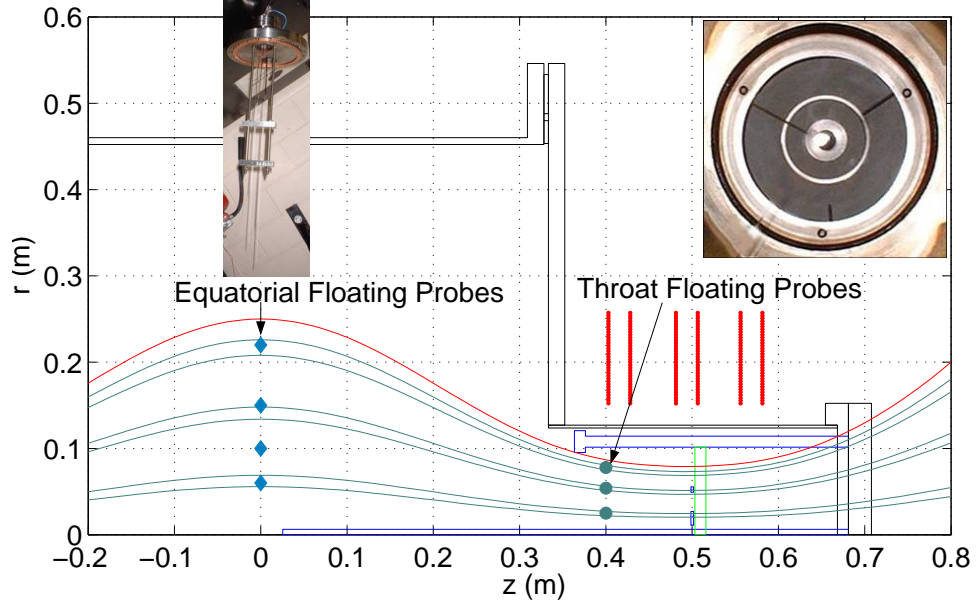


Figure 4.7: Positions of the floating probes. One set is located near the throat of the magnetic mirror and the other at the equatorial plane of the machine.

isolated from the vacuum chamber through a high input impedance $\sim 2 \text{ M}\Omega$, limiting the current drawn from the plasma to avoid loading effects. This effect occurs when the current collected by the probe becomes the ion saturation current $I_{i,sat}$ defined in Eq. (4.2) or its increased value due to sheath expansion (Section 4.1.1). In Fig. 4.8 a typical $I - V_0$ characteristic curve is displaced by a floating potential $V_f \sim 675 \text{ V}$ and has a $I_{i,sat} \sim 1 \text{ mA}$ that increases due to sheath expansion. Three different input impedances R are tested. The $100 \text{ k}\Omega$ impedance intersects the characteristic curve at $V_0^* \sim 300 \text{ V}$, that is the value one would read for V_f , causing a $\sim 100 \%$ error in the measurement. A $1 \text{ M}\Omega$

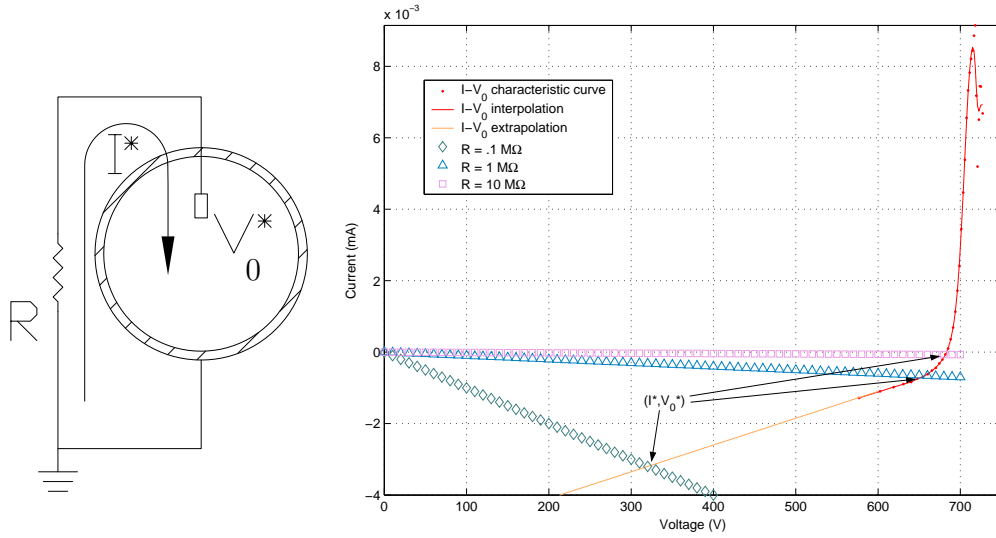


Figure 4.8: Loading effect of the plasma due to different input impedances used at the floating probes. The intersection between the plasma $I - V_0$ characteristic and the resistor curves determines the working point.

intersects at ~ 650 V, with an error of ~ 5 % in the measurement. Finally, the $10 \text{ M}\Omega$ yields the correct value with an error less than 1 %. It is then a good procedure to use different input impedances in order to check what the minimum value is at which the floating potential measurement begins to change, implying loading of the plasma. The use of a small resistor to measure the saturation current and the minimum input impedance for not loading the plasma is not a correct procedure because of the increase in the current with the expansion of the sheath. Only $I_{i,sat}$ is a good reference to determine when the plasma is being loaded. It is important to point out that once the input impedance has been calculated for a positive biased plasma, it can also be used

for a negative biased shot because in this case electrons are collected which have a saturation current much larger than $I_{i,sat}$.

We use voltage dividers to attenuate the floating potential that reaches about 100 times the maximum limit that the data acquisition boards can safely read. They are made with the high input impedance explained in the last paragraph facing the plasma in series with a low resistance, $\sim 2\text{ k}\Omega$, connected to ground. It is important to realize that this output impedance in combination with the long cables used to transfer the signals create a low pass filter with a bandwidth of 10 kHz. If this value is not appropriate a buffer can be used to drive the lines to the data acquisition boards to increase the bandwidth.

4.1.3 Camera

A CCD video camera has been mounted to take pictures of the plasma along the r - z plane. The importance of this diagnostic relays in the qualitative understanding of features such as electron cyclotron resonant layer position, biased layers, magnetic lines visualization, etc. some of them shown in Fig. 4.9. The superposition of the theoretical model increases further the understanding. The CCD camera is a small generic color NTSC video one that acquires 30 frames per second. Its signal travels through a BNC cable to a National Instruments video acquisition board IMAQ PCI-1411 that is triggered so that only when the plasma is biased and rotating the picture is taken, digitized and archived. The resolution achieved is 640×480 pixels.

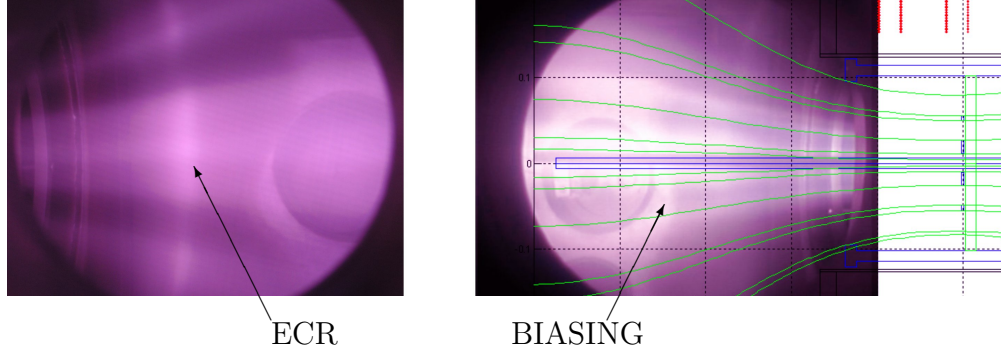


Figure 4.9: Qualitative features captured with the mounted camera. Electron cyclotron resonance is shown on the left hand side and biased magnetic lines on the right hand side. A superposition of the theoretical model is also included.

4.1.4 Biasing Electrodes

The electric field and rotation of the plasma is achieved biasing different electrodes at the throat of the mirror magnetic field (Section 3.5). The potential sets how fast the plasma spins and the current is a consequence of the torque needed to sustain the rotation. The high potential is reduced with voltage dividers similar to the ones used in the floating probes (Section 4.1.2), but with a lower input impedance. This allows for lower output impedance of the voltage divider and higher bandwidth of the signal. The currents are measured using EMPRO² shunts with resolutions of 100 mV per 1 A or 10 A.

²<http://www.emproshunts.com>

4.2 Signal Conditioning

Once the signals leave their corresponding diagnostics, they travel to signal conditioning devices. Their role is to act as isolation for high common floating voltage, amplifiers for small signals, or the removal of possible ground loops. Also, filters are used to remove high frequency noise or limit the bandwidth so that aliasing³ does not happen when the data acquisition boards digitize the signals at a sampling frequency f_s [19].

Tektronix A6902A isolation amplifiers are the preferred ones for the Langmuir/Mach probe because they have 2 kV of common mode voltage isolation and a bandwidth of 10 MHz. Burr Brown 3650 isolation amplifiers can handle 2 kV common mode voltages with a rejection of 140 dB but their bandwidth is limited to 15 kHz. Filters are mainly designed for low pass frequency using RC circuits with cut off frequencies of 20 kHz.

4.3 Data Acquisition

After the conditioning stage the signals travel to a computer as shown in Fig. 4.1 where National Instruments⁴ data acquisition boards digitize them. The boards used in the experiment are the E-Series and their main characteristics are shown in Table 4.1.

³Aliasing is an effect by which a signal with a frequency higher than $f_s/2$ appears as a signal with a frequency lower than $f_s/2$. For example, a sinusoidal signal with the same frequency as the sampling f_s would appear as DC signal.

⁴<http://www.ni.com>

Acquisition Board	# Differential Channels	Maximum Sampling Frequency	Resolution
PCI-MIO-16E-1	8	1.25 MSamples/s	12-bit
AT-MIO-64E-3	32	0.5 MSamples/s	12-bit

Table 4.1: Main characteristics of the National Instruments acquisition boards used to digitize the signals collected with the diagnostics.

The maximum sampling frequency of these particular boards is shared by all the channels being acquired. If the maximum sampling frequency of the AT-MIO-64E-3 is 500 kSamples/s and the total number of channels being sampled is 20 then the maximum sampling rate per channel is 25 kSamples/s. The cut off frequency of the low pass filters is bellow the sampling frequency per channel so that aliasing does not occur. The acquisition boards are controlled by the Labview software running under Windows operating system.

A code has been written in Labview by the author to acquire the data and transfer it to an archive. A screenshot of the control panel that is the interface between the code and the user is shown in Fig. 4.10. You can see a shot button to fire the biasing voltage for rotation, a move probe button to scan the Langmuir/Mach probe across the plasma, and the raw data collected in real time on the screen. A typical “wire code“ that runs behind the interfaces is shown in Fig. (4.11).

The sequence followed by the code is shown in Fig. 4.12. It starts by pressing the run button in the Labview window. The code initializes different digital lines such as the one to control the Langmuir/Mach probe motor drive,

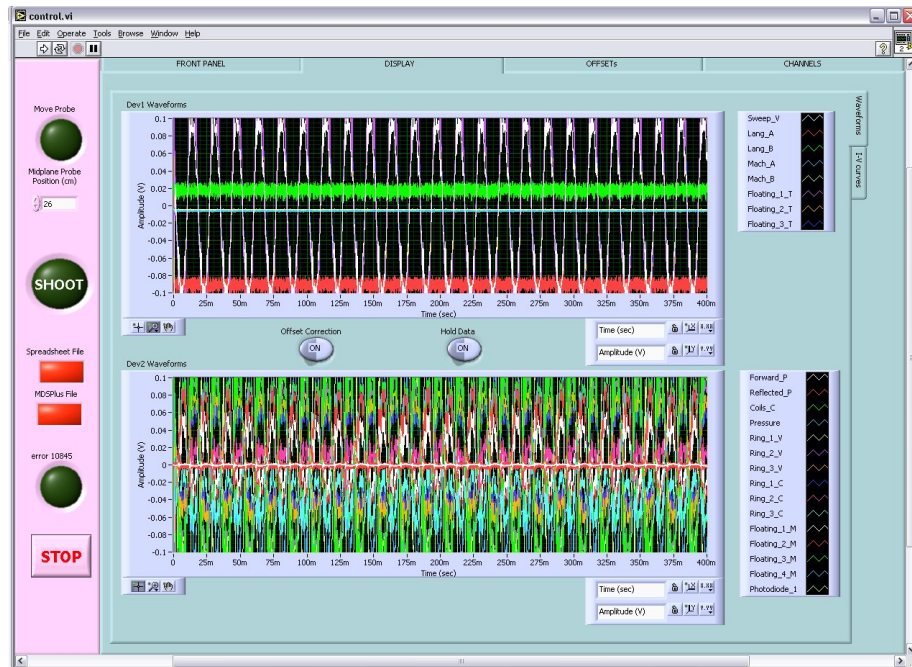


Figure 4.10: Screenshot of part of the control panel written in Labview that is the interface between the user and the data acquisition and archiving codes.

and variables such as analog input AI that contains all the channels and their data, sampling rate, offsets, etc. Then the code enters in the offset phase. Offsets appear due to the diagnostics design or the conditioning used. Amplifiers, for example, need about 5 minutes to warm up for the offset not to drift in time.

The National Instruments boards used do not show any offset when the inputs are shorted, that is, the voltage read is zero. If offsets are required by the user then the code runs another code, `offset.vi`, that checks the channels needed to be digitized and gets a sample using `getdata.vi`. The data is 10 Hz digitally

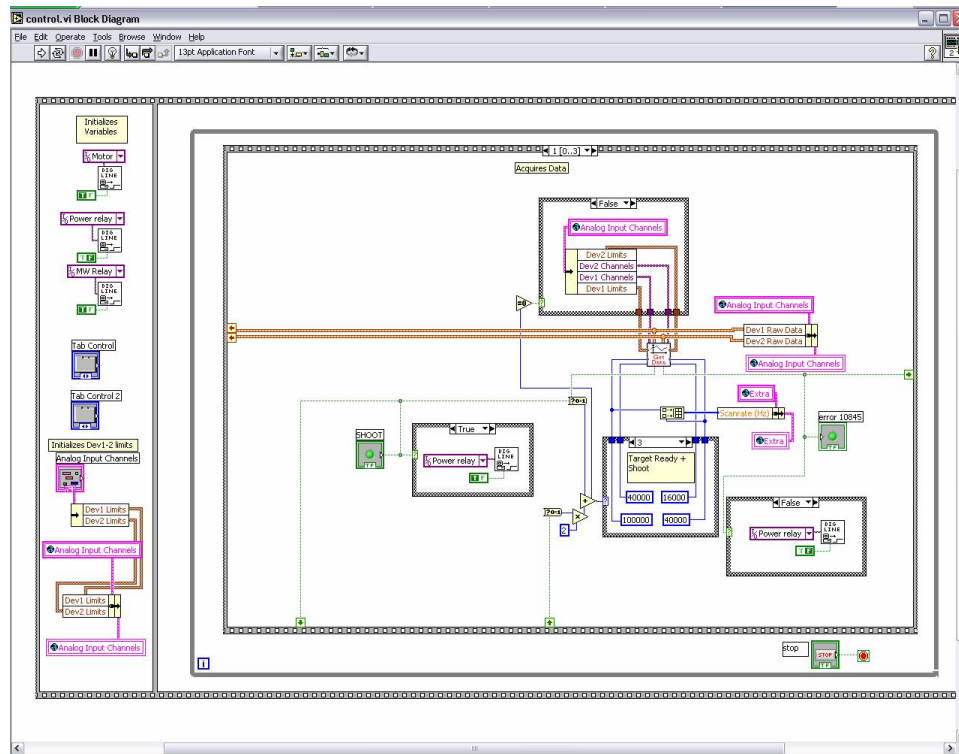


Figure 4.11: “Wire code“ that runs behind Labview interfaces. This frame corresponds to the part of the sequence where the characteristics of the next shot pass to the acquire.vi for data acquisition.

low pass filtered to extract the DC component, save it in the variable AI, and display it. The code has also the opportunity to reset all the offsets to zero if required. After the offset phase the code enters in the acquisition phase. There, the program checks if the machine is ready (microwaves, capacitor bank, etc. are ON) which is manually controlled by the user. The program also checks if a shot has been required. Considering these two options the code runs getdata.vi and samples the channels at different speeds, the fastest corresponding to the

machine ready and a shot requested. If a shot is not needed the code still samples at lower speeds so that the operator can see the status of the different variables. The digitized data is saved in the AI variable and displayed on screen. After the acquisition section the code goes into the file phase. If the data is requested to be stored the code interfaces with the MDSplus application locally using MS-DOS. A shot is created, comments are added as well as data. A shot is created, comments are added as well as data.

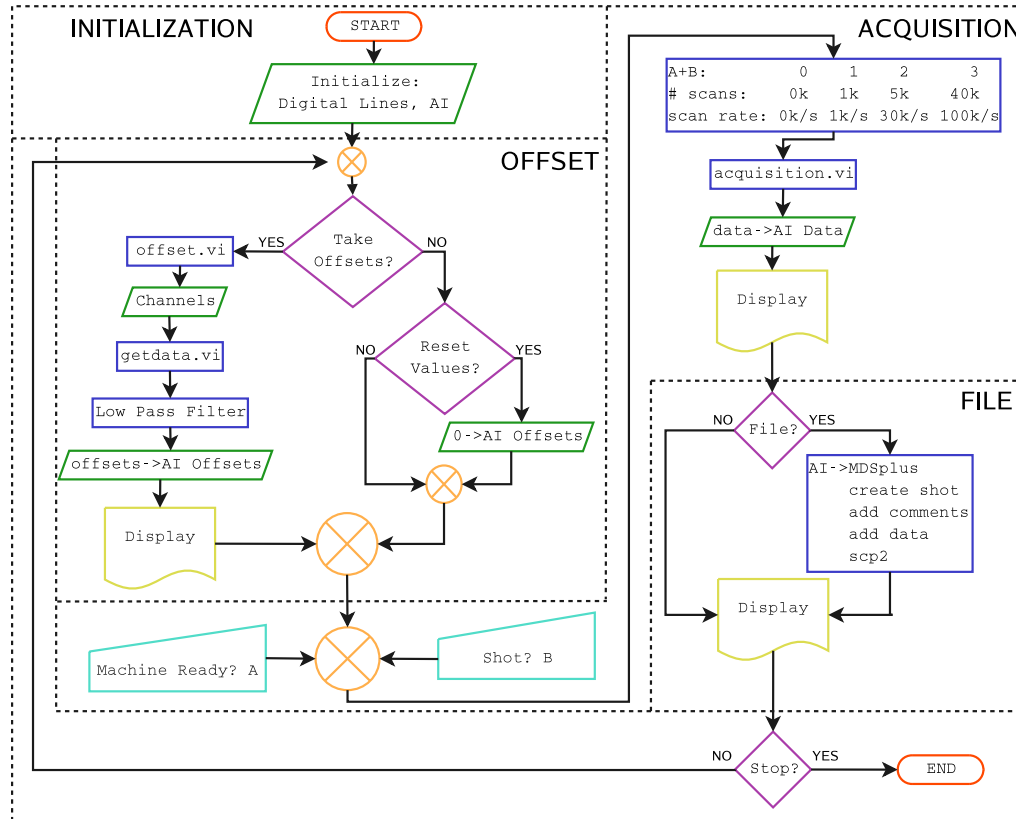


Figure 4.12: Sequence used by the code written in Labview to control the experiment, acquire data and transfer it to an archive server.

Then the shot is transferred securely to the archive computer through the network using SCP protocol. Once the file phase finishes the code starts over unless the user stops it. The whole loop, including acquisition and archiving lasts about 5 seconds, where at least 4 of them are spent transferring data. The Labview code has the advantage of being controlled remotely using any web browser which allows different users to run the experiment from their own computer while doing other activities such as calibrating a diagnostic in situ.

4.4 Data Archiving

The Labview application transfers the files containing the shots with data and comments to an archive computer running an MDSplus⁵ server. The choice of MDSplus as the archive system is due to the many advantages it offers such as:

- The client/server connection allows users to access the data worldwide without the need of file transfers.
- All the data is saved in a single hierarchical structure like the one shown in Fig. 4.13.
- The data can be accessed relatively easy by different applications such as Labview, Matlab, IDL.

⁵<http://www.mdsplus.org>

- The application is available in different operating systems such as Linux, Windows, Mac.
- It is widely used in the fusion community.

In the present experiment the server runs under Linux operating system and allows people in the MBX group to access the data. The whole hierarchical structure can be seen with the Traverser application and a typical tree is shown in Fig. 4.13.

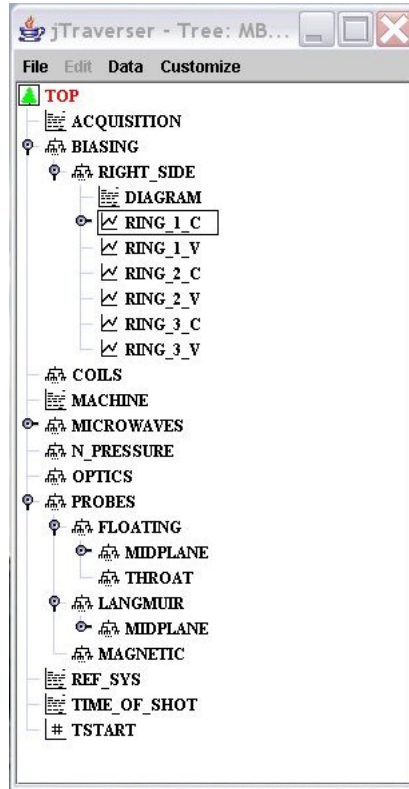


Figure 4.13: MDSplus tree showing its hierarchical structure.

Once the data resides in the server, it is access locally or remotely by codes written in Matlab for processing or Scope for viewing data as is shown in Fig. 4.14. Processed data can also be stored in the same shot where the raw data resides.

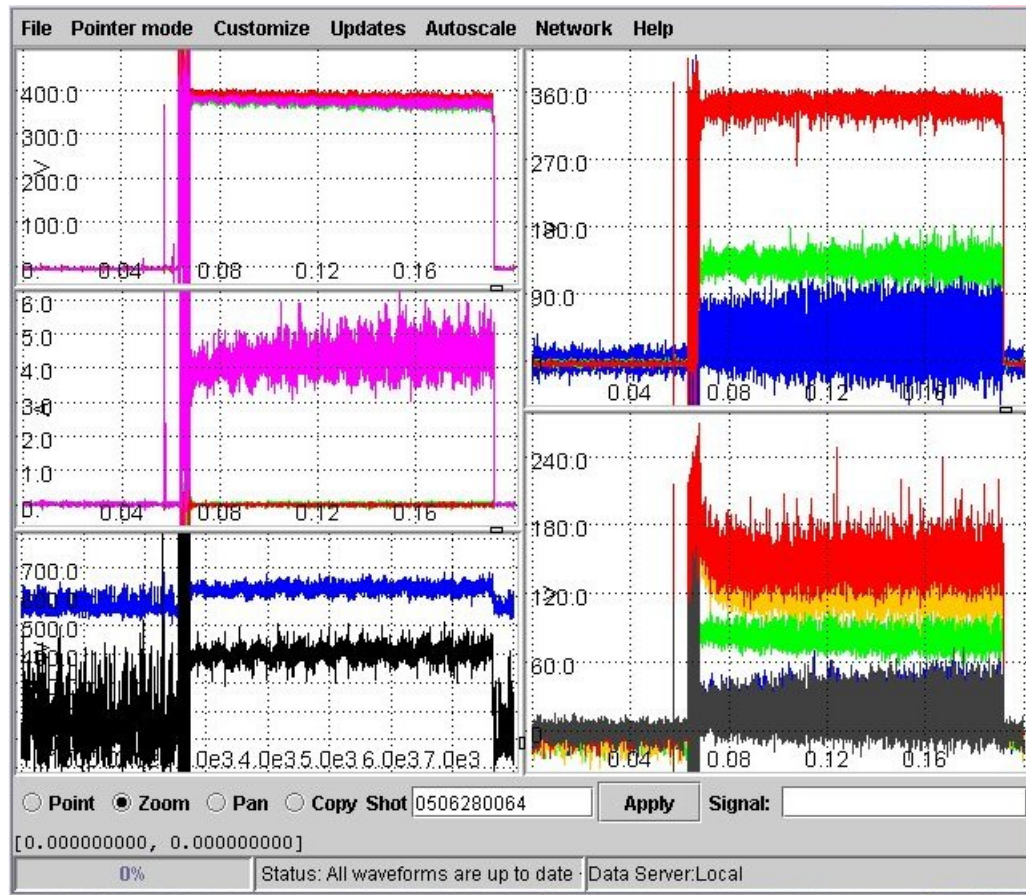


Figure 4.14: Scope application to easily view the data stored in an MDSplus shot locally or remotely.

Chapter 5

Experimental Results

In this chapter we present the measurements obtained using the diagnostics described in Chapter 4 to characterize the different plasma states. The results will let us understand how to improve the system to achieve faster rotation and profile control. The measurements will be compared to the theory developed in Chapter 2. Initially the target plasma is analyzed, where target refers to the state created by the microwaves under the external magnetic field but not electrically biased. Later in the chapter, biased electrodes rotate the target plasma as described in Section 3.5 and its response is diagnosed and analyzed.

5.1 Target Plasma

A combination of 5 'knobs' controls the creation of the different target plasmas. These knobs are: microwave power flowing into and out of the vacuum chamber (referred as forward and reflected power), neutral gas pressure and external magnetic field intensity and geometry. The applied voltage on the magnetron controls the power flowing into the system (0 to 1) kW while the tuner controls the amount of reflected power. A minimum reflection is always

desired but not always possible. A needle valve regulates the neutral pressure (10^{-7} to 10^{-3}) Torr. The currents flowing through the external coils control the intensity of the magnetic field, with a maximum of 1200 A due to coil heating and a minimum of 500 A due to the microwave source limitation. The geometry of the magnetic field is a knob that has been fixed to maximize the mirror ratio R , reaching the largest mirror as well as centrifugal confinement.

In most of the cases a greater forward power in the microwaves results in a denser plasma for different neutral pressures or magnetic fields. Even though the tuner is varied so that less than 5 % of the total power is reflected, there are some plasma conditions that cannot be tuned and 20 % reflected powers occur. In any case a denser plasma is obtained when a higher forward power is used even if the net power is the same. Something to notice is that a second resonant layer, not as intense in brightness as the first one, is seen at the other side of the equatorial plane (Fig. 4.9). This could be due to the right circularly polarized wave not completely absorbed by the first resonance or due to the left polarization being reflected off the walls and converted to right circularly polarization.

Considering that a maximum in forward power maximizes the plasma density in all cases, we have performed radial scans using the Langmuir probe at the equatorial plane with different magnetic field intensities and neutral pressures. Fig 5.1 shows the change in plasma density under the different conditions. The overall plasma density decreases as the neutral density increases. Even if more neutral targets increase the ionization frequency in the

resonant layer, more collisions of the plasma bulk with neutrals decreases the particle confinement time resulting in a lower density plasma. An increase in

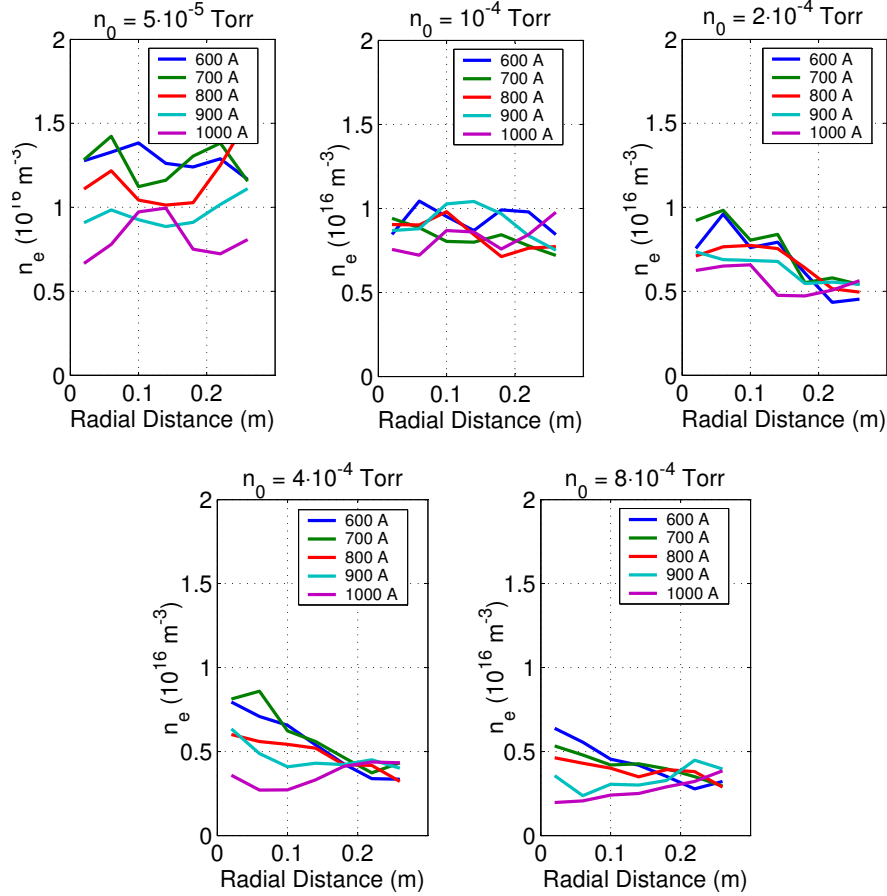


Figure 5.1: Density radial scan at the midplane using maximum microwave power for different magnetic field intensities and neutral pressures. The density increases when the neutral density or the magnetic field intensity decreases.

the magnetic field decreases the plasma density and this effect is mostly noticed for neutral densities higher than $2 \cdot 10^{-4}$ Torr where the profile changes

from a plasma with a center core at low magnetic field intensities to a hollow plasma at higher fields. Even if a bigger magnetic field intensity reduces the perpendicular losses due to diffusion by a factor $(\Omega_{cyclotron}\tau_{collisional})^{-2}$, it does not affect the loss cone losses in the parallel direction. The intensity of the magnetic field mostly affects the source function of the plasma which changes position as shown in Section 3.4.

The figure also shows that the density does not drop to zero at the limiter boundary as is the case in experiments where a scrap off layer is produced. On the contrary the density stays high due to the source function created by the microwaves that operates well outside the limiter position. A solution for this problem would be to extend the microwave waveguide inside the vacuum vessel until the ceramic insulator where the vacuum window would be placed so that waves spread out less before reaching the resonance. At the same time the resonance can be brought close to the ceramic disk working at lower magnetic fields, that is not possible presently because ionization would occur behind the current window position. The waveguide could be tapered and filled with some higher dielectric constant ϵ material like boron nitride ($\epsilon = 4$) so that the waves can still propagate and the emission area is smaller.

As mentioned in Section 3.4 the method of launching the waves parallel to the magnetic field lines avoids the cutoff usually imposed by ω_{pe} in other methods. In our case the densities achieved are about 7 times less than this limit. A 6 kW microwave source was borrowed from Prof. Kenneth Gentle reaching about 3 times the previous densities still without reaching this limit.

At higher powers the tuning for zero reflected power became almost impossible and reflections of 25 % were typical.

For the same conditions present in the density measurements the temperature profile is presented in Fig. 5.2. It shows a fairly isothermal plasma with values of (4 ± 1) eV for all the different magnetic fields intensities and neutral pressures.

Measurements carried out with the Langmuir probe facing the microwave source show higher values of temperatures and densities compared to the measurements in the side facing the rings (Fig. 5.3). This difference is evidence of the losses in the mirror bottle. The stronger the magnetic field intensity the higher the difference in the two sides of the probe reaching ratios as high as 1.4.

In summary, we use the maximum power available in the microwaves to achieve the highest plasma density that according to the measurements decreases as the neutral pressure or the magnetic field increases. The temperatures are ~ 4 eV. Density measurements show that the limiter is not effective in controlling the radial extent of the plasma due to the location of the plasma source function.

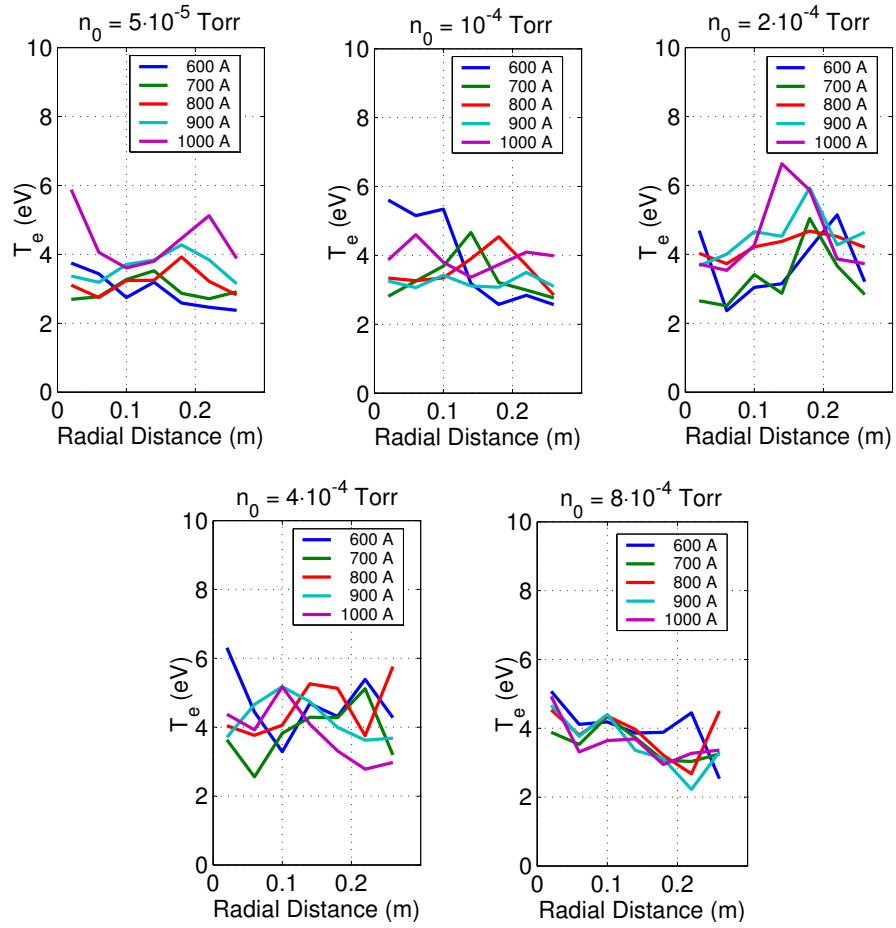


Figure 5.2: Temperature radial scan at the midplane using maximum microwave power for different magnetic field intensities and neutral pressures. The electron temperature is $\sim (4 \pm 1)$ eV.

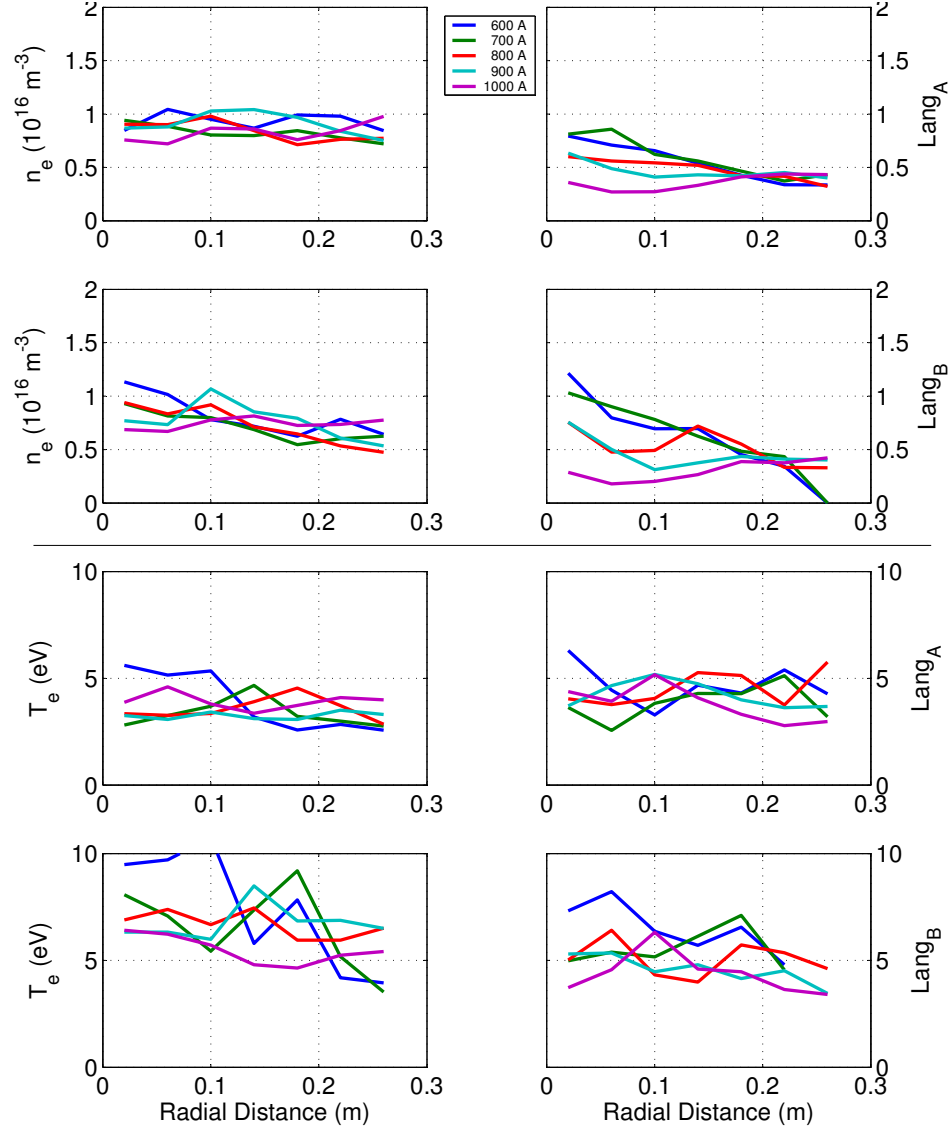


Figure 5.3: Difference in density profiles measured by the Langmuir probe facing the plasma source (Lang_A) and the electrode region (Lang_B), evidence of losses in the mirror magnetic bottle.

5.2 Plasma Speed and Electric Drift

The rotational velocity should agree with the electric drift V_E in the case of velocities high enough compared to the diamagnetic drift, but subsonic so that the centrifugal drift does not contribute considerably. The velocity profile is measured with the Mach probe at the equatorial plane as described in Section 4.1.1 while $V_E = E/B$ is calculated measuring the plasma potential at the equatorial plane, taking its gradient to get the electric field and dividing by the magnetic field given by the model in Section 3.3. Fig. 5.4 shows a typical scan for a biased plasma with a center rod, two rings and the limiter (in gray from left to right) and compared to an unbiased plasma [36]. The electrode positions are extrapolated to the midplane following the magnetic lines. The neutral density is 0.1 mTorr and the coil current is 600 A. The unbiased plasma presents a roughly constant floating potential with a consequent low or zero electric field and so negligible rotational velocity. The outer (inner) ring is biased at ± 50 V (± 100 V) while the center rod is at ± 150 V with respect to the limiter and chamber. The positive biased plasma shows a good correlation between the Mach probe measurement and V_E (where the temperature is roughly constant so that the gradient in plasma potential is the same as the gradient in floating potential).

As mentioned in Section 4.1.1, while most of the theories regarding Mach probes agree that there is a logarithmic dependence between velocity and ratio of probe currents, the actual calibration factor K is still in dispute. In our case $K = 3.7$ is obtained that is in close agreement with typical values [20].

The maximum velocity is obtained between the two biased rings. For radii less than 0.1 m the plasma seems to rotate rigidly, that is $V \sim r\Omega$, with $\Omega = 9 \cdot 10^4$ rad/sec. This case was analyzed in Section 2.2.3. Between 0.1 m

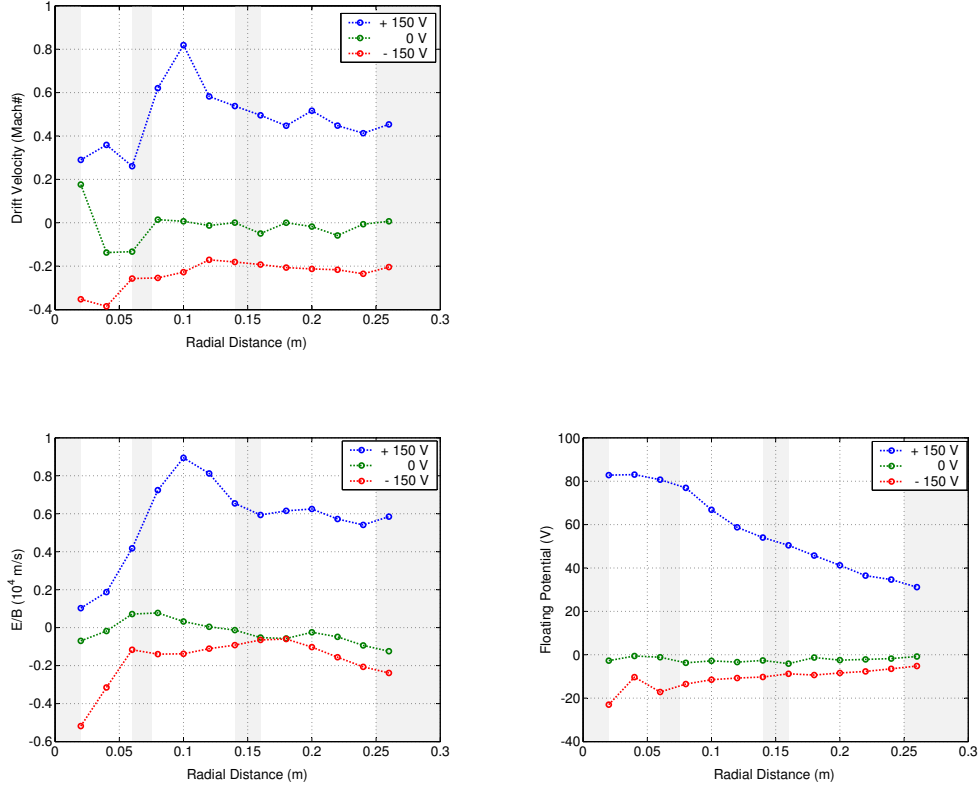


Figure 5.4: Velocity measured with the Mach probe compared to the electric drift V_E calculated from the plasma potential measured by the Langmuir probe. In green the plasma is unbiased while in blue (red) is positively (negatively) biased with respect to the limiter and chamber. The electrode positions extrapolated to the midplane following the magnetic lines are shown in gray. The plasma speed agrees with V_E .

and 0.15 m there is a transition region where the velocity decays. For larger

radii the speed remains roughly constant so that $\Omega \sim r^{-1}$ with a consequently constant electric field. For a negative biased plasma the velocity of rotation is much smaller compared with the positive biased case but still enough to be measured (asymmetry with respect to the polarity). The rotation measured with the Mach probe agrees with V_E using the calibration factor calculated previously.

As mentioned in Section 4.1.1 the same effect that causes the Mach probe to measure different currents depending of the velocity, acts on the Langmuir probe so that a decoupling of velocity and density is difficult to do. This effect is shown in Fig. 5.5 where a peak in density is observed at the same position as the maximum in speed occurs. The density drops to its non biased state values for small radii where the velocity drops to zero. The decrease in density observed at $r = 0.14$ m corresponds to the same position as one of the biased electrodes. This effect is attributed to the positive biased electrode, collecting current along the field lines and decreasing the electron density [38]. The small rotation achieved when the plasma is negative biased is not enough to affect the density measurements that show same values as the non rotating case.

In summary, the rotational speeds measured with the Mach probe agree with the electric drift V_E measured by the Langmuir probe for low applied voltages (< 200 V). The rotation presents asymmetry with respect to the polarity of the external bias, positive (negative) potentials yields high (low) rotational speeds. Langmuir probe data shows how high speeds obtained with

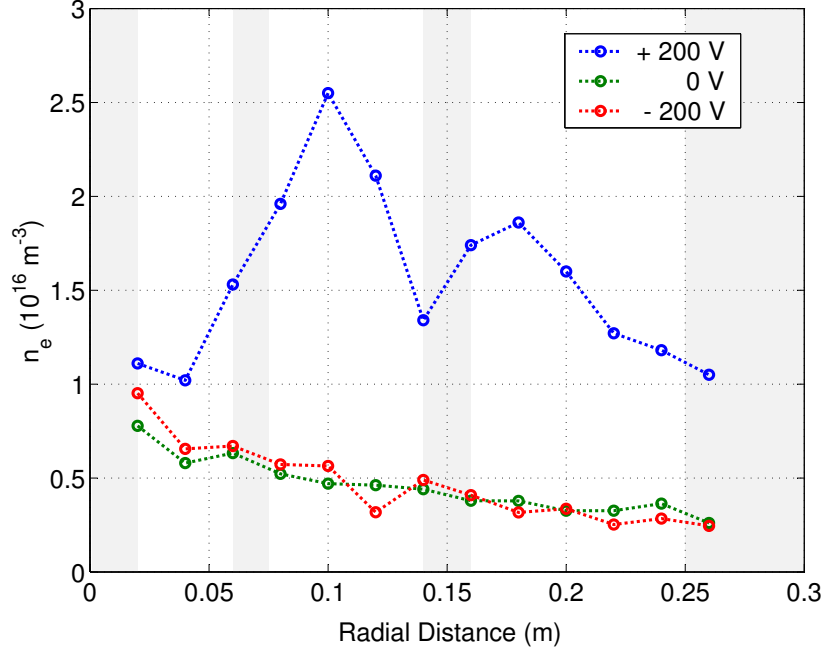


Figure 5.5: Non rotating plasma density profile affected by the rotation. In green the plasma is unbiased while in blue (red) is positively (negatively) biased with respect to the limiter and chamber. The electrode positions extrapolated to the midplane following the magnetic lines are shown in gray.

positive bias affect the density measurements.

5.3 Electrode Configurations

Different electrode configurations have been used as time went by with an increase in performance as shown in Section 3.5. The objective has been to achieve maximum potential penetration of the biasing voltage inside the

plasma and consequently a maximum rotational speed. The reason for the non perfect penetration or transfer from the biasing electrodes to the plasma bulk is the combined behavior of the electrodes sheaths and plasma dynamics. At the same time, it is desirable to control the shear profile for stability purposes [14]. Originally, without knowing the possible response of the plasma to the applied potentials, 1/2 in. stainless steel bolts were used as shown in Fig. 3.11 top left hand side. The purpose was to have the maximum flexibility to bias the plasma, radially as well as azimuthally in case it was needed or just as probes to measure plasma potential and density. The potentials measured at the equatorial plane with the Langmuir-Mach probe were small compared to the applied potentials (± 50 V) so that most of the drop happened at the electrode sheaths [4]. The currents were ~ 0.1 A (0.02 A) when the bolts were positive (negative) biased. The plasma potential was not affected much by the bolts which then behaved mostly as Langmuir probes.

In order to affect the plasma in a higher degree we used a hollow 1/2 in. stainless steel center rod instead as shown in Fig. 3.11 top right hand side. This type of configuration was successfully used in past experiments [9] and presently in the MCX experiment [8]. There is a big advantage of simplicity and at the same time a big disadvantage of non being able to control the potential in the radial direction inside the plasma and consequently the shear flow in the system. This is a fundamental point in MCX where the aim is to study centrifugal confinement for fusion conditions working under the appropriate shear flow to suppress undesired instabilities at high Mach numbers [15].

In the present scheme, the shear is controlled by the plasma dynamics rather than externally. In our case since we use microwaves launched on one side of the mirror to generate the plasma the center rod extended only to the equatorial plane rather than all the way through. In this way the perturbation to the microwaves is minimized. The electrode area has been increased 200 times compared to the bolts used in the previous configurations. The potential measured at the equatorial plane for a rod biased at ± 60 V against the grounded limiter and chamber is shown in Fig. 5.6 [32]. Similar to the bolts a

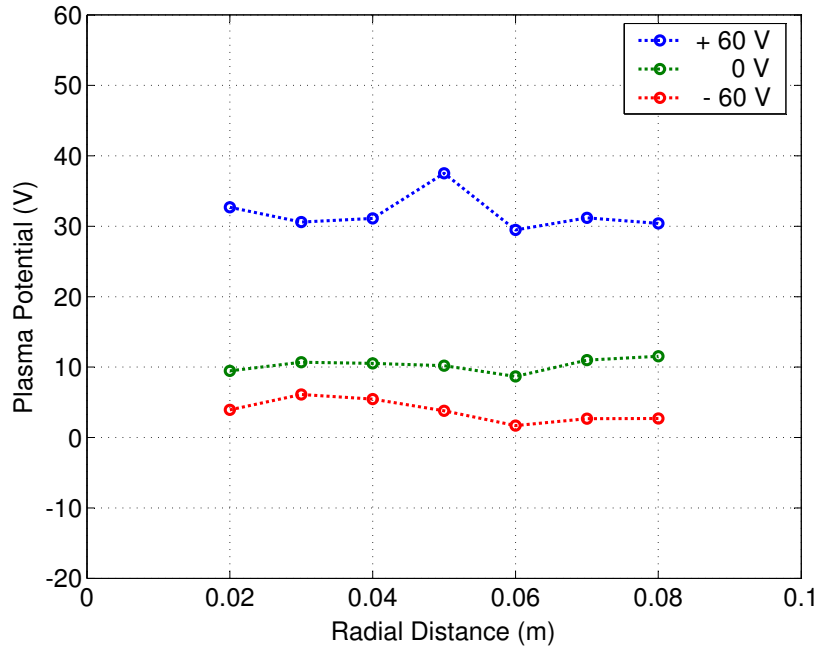


Figure 5.6: Potential measured at the equatorial plane using the center rod. In green the plasma is unbiased while in blue (red) it is positively (negatively) biased with respect to the limiter and chamber. The penetration of the potential is low.

large fraction of the biasing voltage drops at the electrode sheath so that the plasma is mostly non rotating. The current amplitudes are not much different than the bolt electrodes which suggests that the current is mostly function of the projection of the electrode surface onto the insulator. That is, the current that crosses the magnetic field surface that is connected to the base of the center rod (where the insulator is located) will be collected with the rod or with a bolt of the same area. The only difference is that in the first case the sheath is nearly parallel to the magnetic field and in the second case the sheath forms normal to the incident magnetic field. The plasma potential is slightly modified in this configuration and this type of electrode still behaves as a probe without affecting the plasma structure. The currents collected scale with the projection of the electrode area at the throat where the insulator is located.

Using the experience acquired with the previous electrode configurations we built a combination of center rod and rings as shown in Fig. 3.11 bottom left hand side with an increase in the collecting area by a factor of 15 per ring. The ring configuration has being used in other experiments [1, 38]. Typical potentials at the equatorial plane for total biased voltages of ± 150 V with respect to the limiter and chamber were shown in Fig. 5.4 [36]. Note that approximately 50 % of the applied potential has penetrated to the equatorial plane for positive bias, an improvement mostly due to the larger electrode areas. The bias on the rod penetrates slightly. The negative bias does not penetrate creating an asymmetry that will be discussed in Section 5.4. The

role of the limiter and chamber is more than important because they act as the return path for the electrode currents. To show this point explicitly we can bias both rings with respect to each other while completely disconnected from the limiter and chamber [35]. The potential at the equatorial plane is shown in Fig. 5.7 as red or green for each polarity. For comparison the potential achieved with the limiter used as the return path is shown in blue. There is

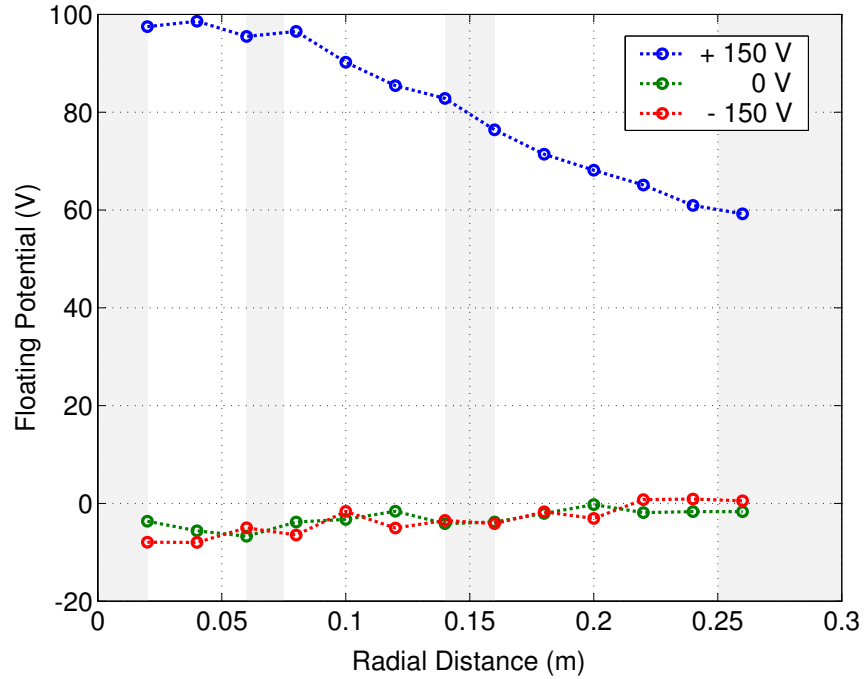


Figure 5.7: Comparison of the penetration of the potential when the electrode (red or green) or the limiter (blue) are used as return paths. The electrode positions extrapolated to the midplane following the magnetic lines are shown in gray. There is no penetration of the potential when an electrode is used as the current return path instead of the limiter.

no penetration of the potential with any polarity on the rings and at the same time the circulating currents drop from ~ 1 A using the limiter as the return path to ~ 0.04 A using only the electrodes. That is, the penetration decreases because the area collected decreases also.

The ability to control the potential profile is shown in Fig. 5.8. In blue

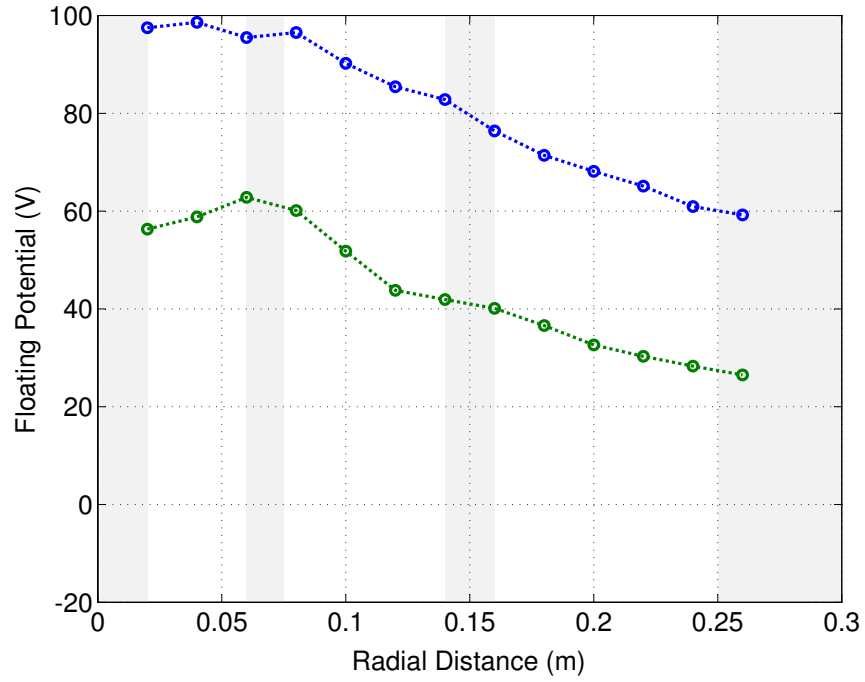


Figure 5.8: Ability to control the potential profile. In green the outer ring is non biased while in blue is biased. The overall potential shifts at the equatorial plane due to the addition of potential to the outer ring.

the outer ring, inner ring and center rod are bias with respect to the limiter at 50 V, 100 V and 150 V respectively while in green the outer ring is not

biased. The overall potential shifts at the equatorial plane due to the addition of potential to the outer ring. The control of the profile shape and shear flow will be discussed in Section 5.5.

In order to study the maximum penetration of the potential so that the highest rotational speeds can be obtained with a possible ionization process [2] we designed a fourth type of electrode. It is a simple plate as shown in Fig. 3.11 bottom right hand side that biases most of the magnetic field lines at the same potential. This does not necessarily mean that the plasma bulk will be equipotential because the penetration is not perfect as described in Section 5.5. A typical profile is shown in Fig. 5.9, where the neutral density is $4 \cdot 10^{-5}$ Torr, the magnetic field ~ 0.06 T on the axis at the equatorial plane and the biasing is ± 400 V. Under the same conditions and for comparison, we show the potential created by the inner ring electrode biased with respect to the limiter. The total biasing area has increased by a factor of 6 compared to a single ring. The penetration of the potential for negative bias improves by a factor of 2 reaching rotational speeds of 10^4 m/s together with an increase of ions collected. For positive bias the current increases compared to the ring electrodes but not more than a factor of 2. The penetration of the potential is only slightly improved. The limiting area when the plate is positive biased is the limiter and chamber as discussed later in Section 5.6. Overall this is the best configuration to reach high potential and rotational speeds in the plasma bulk, unfortunately loosing control of the shear profile.

Summarizing, the bigger the biasing electrode area, the better potential

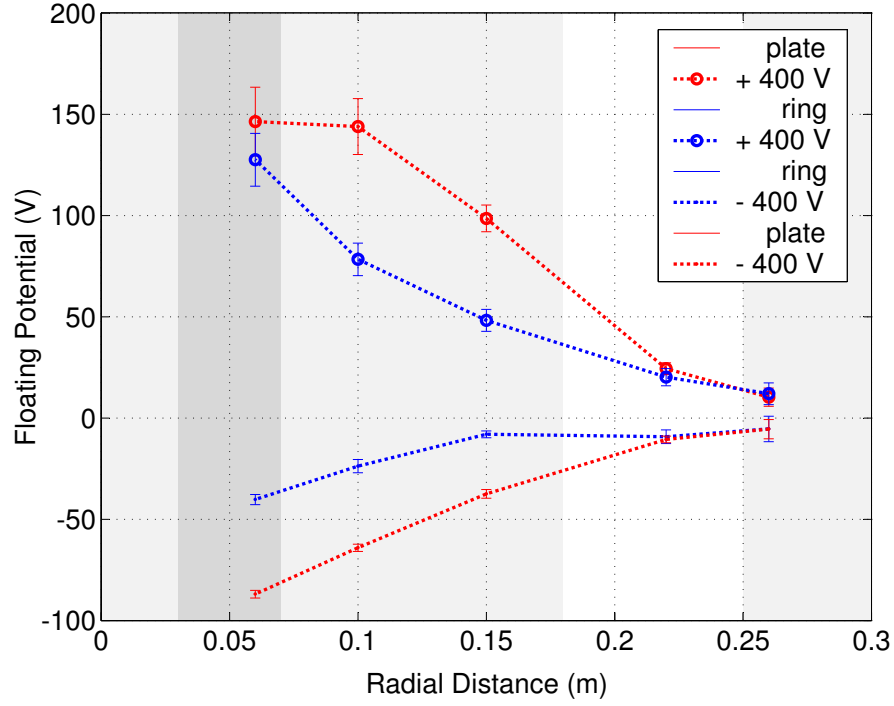


Figure 5.9: Potential measured at the equatorial plane for the plate (inner ring) electrode biased at ± 400 V shown in red (blue). The plate (inner ring) position extrapolated to the midplane following the magnetic lines is shown in light (dark) gray. The plate allows better penetration of the potential compared to the ring.

penetration and the faster rotational speeds are achieved. A ring type configuration is desired to achieve shear profile control. Then, the best configuration would be one where the whole insulator is mostly covered with concentric rings for maximum surface and shear control.

5.4 Current Asymmetry

The velocity profiles shown in Section 5.2 present asymmetry in the system with the applied external biasing voltage. The same behavior has been observed with all the different electrode configurations used (Section 5.3). In all the cases the rotation is clearly proportional not only to the polarity of the external voltage applied but also to the amount of current driven through the system. High rotational plasma speeds appear when the electrodes are positively biased with respect to the limiter and chamber as shown in Fig. 5.4. Electrode currents are ~ 3 A. In contrast, when the electrodes are negatively biased the rotation in the bulk of the plasma is minimal or absent. The electrode currents in this case are smaller when compared to the positive biased case and of the order of ~ 0.1 A. The current asymmetry with the potential applied is seen better when the voltage applied to the plasma is swept. Fig. 5.10 shows a typical behavior of the current for the inner biased ring with a neutral pressure of 0.1 mTorr and 800 A through the coils. The response resembles the $I - V$ characteristic curve of a Langmuir probe as shown in Fig. 4.2. As the electrode is negatively biased with respect to the limiter and chamber ions start being collected and a further increase in negative potential reaches a point where no extra ions are collected and a saturation of the current occurs (ion saturation current $I_{sat,i}$). When the electrode is positively biased ions are rejected while electrons are collected. As the potential increases so does the current that reaches a saturation (electron saturation $I_{sat,e}$) after which no more electrons can be collected. Even if the curve resembles an $I - V$

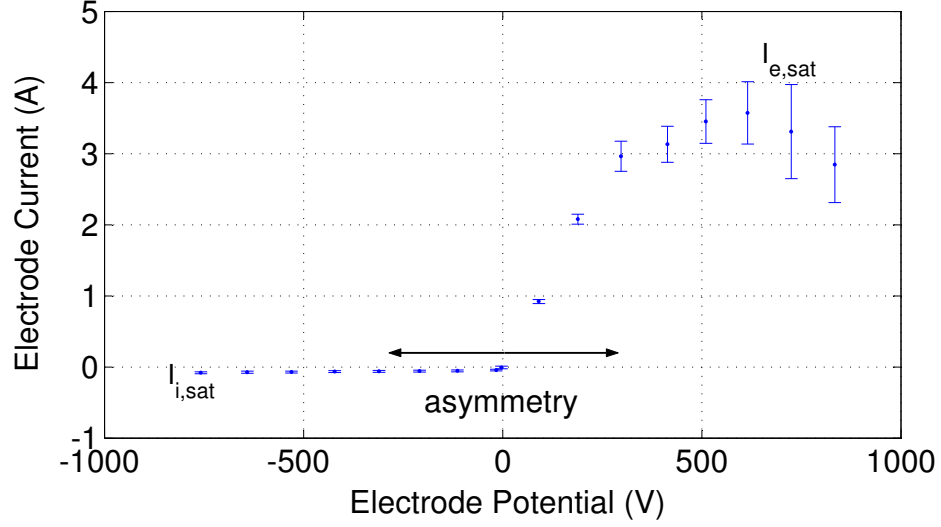


Figure 5.10: Asymmetry in the inner ring electrode current as function of the potential applied to it.

probe characteristic curve, there are three important differences. First, the area of the electrodes is much bigger than the area of typical probes. While Langmuir probe theory is designed for small perturbations to the plasma, the electrodes have an area comparable to the size of the machine so we do not expect the same results. Second, the change in potential to make the transition from ion saturation to electron saturation in a typical probe is a few T_e while it takes about $300 \text{ V} \sim 70 T_e(\text{V})$ when the electrodes are biased as seen in Fig. 5.10. Third, the saturation does not always occur as shown in Fig. 5.11 for a different set of plasma parameters, however the asymmetry in collected current is always present. The asymmetry could also be connected to the

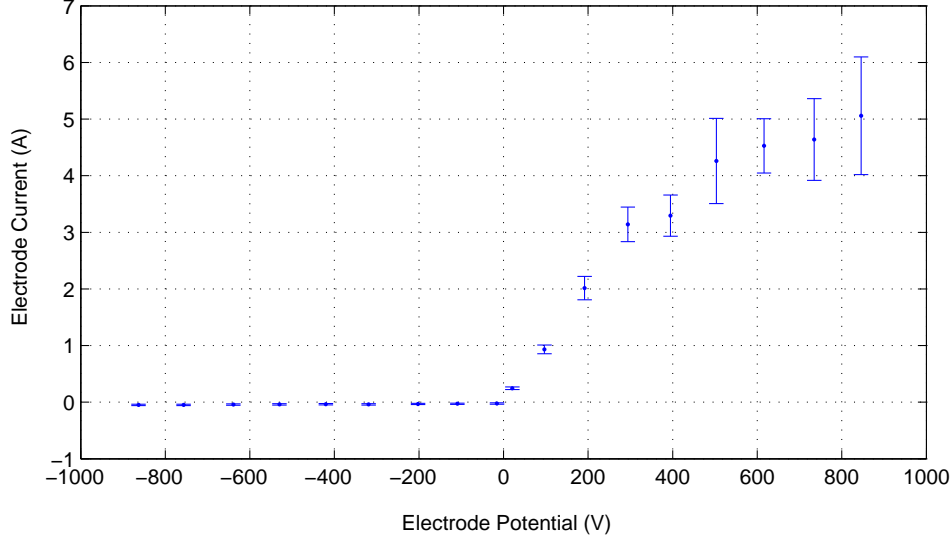


Figure 5.11: Asymmetry but no saturation of the current.

bulk of the plasma that responds differently to either bias polarity as seen in Section 2.2.3 when rotating plasma solutions were discussed.

The effect of asymmetry shown with one electrode ring can be extended to a two electrode system considering the polarity in the biasing voltage with respect to the plasma potential near the corresponding electrode instead of ground. A typical two electrode biased system is shown in Fig. 5.12 [33]. The outer ring (labeled as 1) is AC biased (± 330 V) at 60 Hz with respect to the limiter and chamber while the inner ring (labeled as 2) is DC scanned at voltages ranging from -500 V to 500 V. When the absolute value of the biased potentials are above 100 V the currents saturate for both electrodes.

For voltages less than this value there is an interplay between the electrodes. That is, the transition from ion to electron saturation is shifted by the different electrodes. This asymmetry happens for neutral pressures in the range of $4 \cdot 10^{-5}$ Torr to $8 \cdot 10^{-4}$ Torr and magnetic fields in the range 0.04 T to 0.06 T at the equatorial plane.

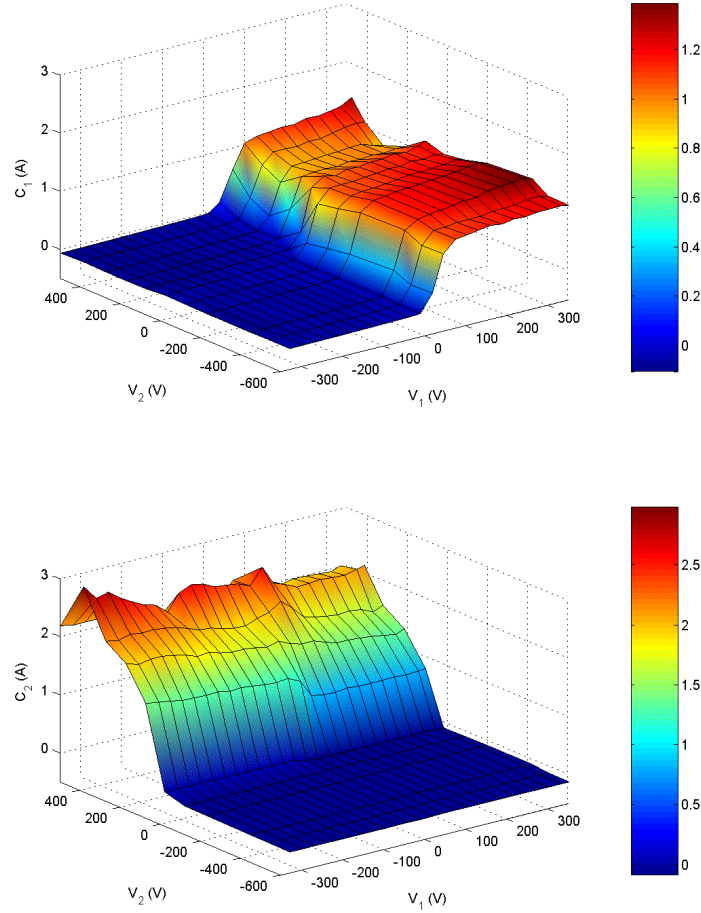


Figure 5.12: Asymmetry in the current C collected by two biased rings at potentials V . The subscript 1 (2) corresponds to the outer (inner) ring.

In summary, for the given range of neutral densities and magnetic fields there is an asymmetry in the response of the plasma with respect to the biasing voltage. The current asymmetry in the plasma resembles the $I - V$ characteristic curve of a Langmuir probe but with modifications.

5.5 Throat Potential Asymmetry

As seen previously in Sections 5.2-5.4 there is asymmetry in the response of the system to the applied external potential. The electrode currents resembles an $I - V$ Langmuir characteristic curve, while the rotational speeds, connected to the plasma potential, show an important difference depending on the polarity of the applied bias. In order to measure the amount of external potential that penetrates into the plasma, three floating probes are located 0.05 m away from the electrodes along the same magnetic field line as described in Section 4.1.2. Knowing the electrode potential, the drop at the electrode sheath can be calculated.

For the current asymmetry described in Fig. 5.10 with a inner ring electrode we show in Fig. 5.13 the potential measured at the probe facing the biased electrode following the magnetic lines. The potential follows the same trend as the asymmetry in the current. That is, for negative bias, low currents flow through the system and there is a large potential drop at the sheath. This leads to a small potential and electric field inside the plasma and a small rotation (through V_E). As the bias potential increases for positive polarities the plasma potential at the equatorial plane and the current also increase.

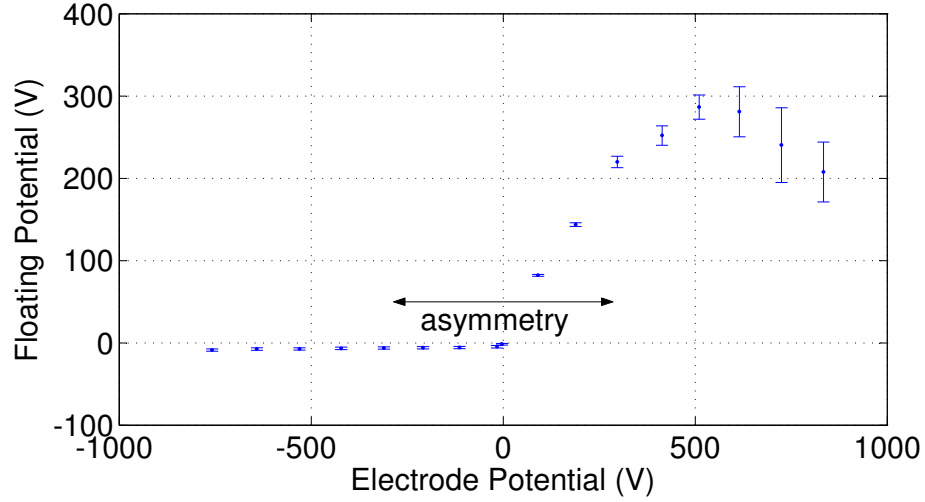


Figure 5.13: Asymmetry in the plasma potential facing the biased inner ring electrode as a function of its potential.

Thus, there is only a small potential drop in the sheath. This increases the rotational speed of the plasma. As the electrode reaches electron saturation current the potential in the plasma and the rotational speed saturate also. For higher applied voltages the current remains fairly constant, as well as the potential inside the plasma. That is, all the extra voltage applied to the electrode is dropped at the sheath and lost.

The physics becomes more interesting when two rings are biased in order to shape the rotational speed and shear flow. The asymmetry in the current is shown in Fig. 5.12. The measured floating potential at the two probes facing

the electrodes along the magnetic field lines is shown in Fig. 5.14. The plasma potential and electrode currents show similar behavior. The saturation regions appear as flat with different levels. The region where both electrodes are positive biased collecting electrons yields the highest penetration of the potential. There are steep transitions and lowering in the plasma potential when one of the electrodes is negative biased collecting ions. In this case, the electrode collecting electrons dominates the plasma potential. The inner ring affects more the plasma potential compared to the outer ring due to its higher currents. Finally, when both electrodes are negative biased collecting ions only slight penetration occurs. A particular potential profile and consequently shear flow can be obtained varying the electrode potentials however the control is not complete because there are ranges of potentials that cannot be selected.

In summary, the potential penetration are proportional to the electrode currents. Both current and potential profiles are similar. When the electrodes collect ions, the penetration of the potential is small while when the electrodes collect electrons at higher currents the penetration improves considerably. The control of a shear flow is partial and possible only when at least one electrode collects electrons. If an electrode collects ions the electrode collecting electrons dominates the plasma potential.

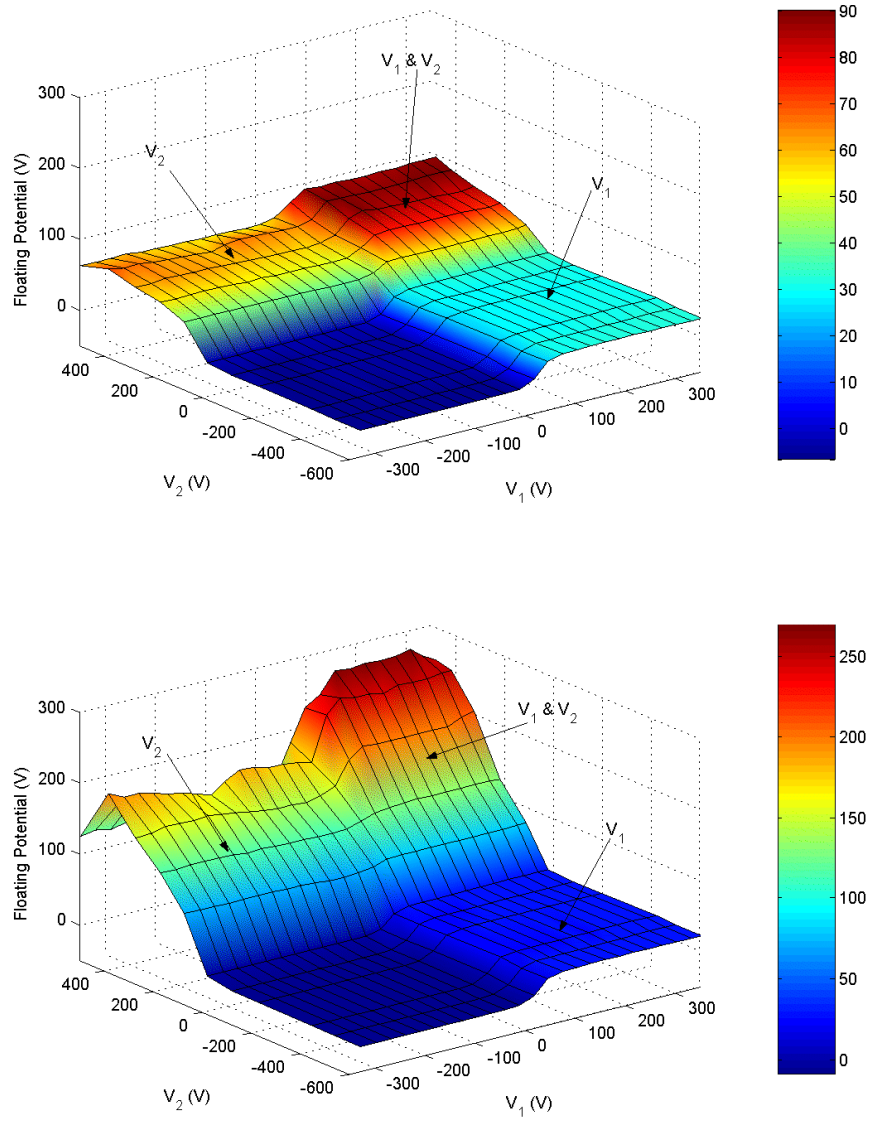


Figure 5.14: Asymmetry in the measured floating potential at the two probes facing the two biased ring electrodes. The top (bottom) corresponds to the plasma potential facing the outer (inner) ring that are labeled 1 (2) respectively.

5.6 Asymmetry Model

A simplified model for the asymmetry present in the plasma [34] is to consider the electrode, limiter and plasma as is shown in Fig. 5.15. The

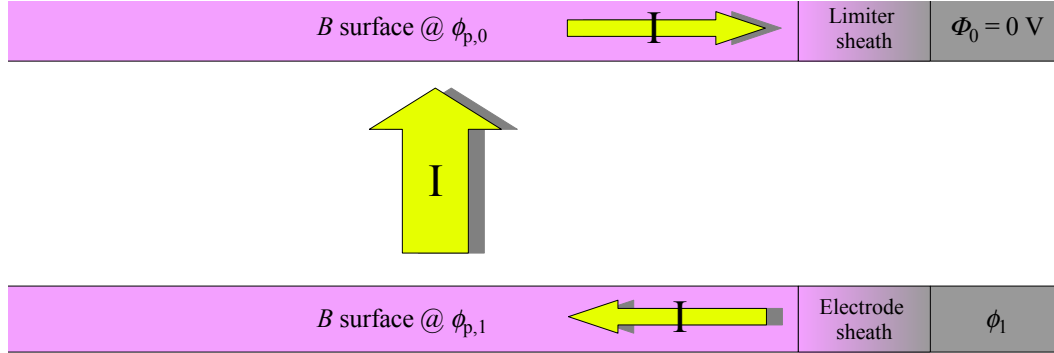


Figure 5.15: Diagram to model the plasma bulk, sheaths and electrodes.

electrode potential ϕ_1 is connected to the plasma potential $\phi_{p,1}$ through a sheath drop. The same assumption holds for the grounded limiter ($\phi_0 = 0$ volts) and the bulk plasma facing it ($\phi_{p,0}$). The equation governing both the plasma and the electrode sheath is [21]

$$I = \begin{cases} I_{e,sat} \cdot e^{\frac{\phi - \phi_p}{T_e}} - I_{i,sat} & \phi \leq \phi_p \\ (I_{e,sat} - I_{i,sat}) + (\phi - \phi_p)/\alpha & \phi > \phi_p \end{cases} \quad (5.1)$$

where $I_{e,sat}$ and $I_{i,sat}$ are the electron and ion saturation currents, T_e the electron temperature, and α is a resistance that accounts for non perfect saturation. The saturation currents are proportional to the area of the electrodes

being considered. The magnetic field lines in the bulk of the plasma are considered equipotentials while the plasma is assumed to have a perpendicular resistance R_{\perp} given in Section 2.3. Then, the current carried across the magnetic surfaces is related to the corresponding voltages by

$$\phi_{p,1} - \phi_{p,0} = R_{\perp} I \quad (5.2)$$

This system results in 3 equations (2 sheaths and 1 plasma bulk) and 3 unknowns ($I, \phi_{p,1}, \phi_{p,0}$) provided ϕ_1 is the given applied potential and T_e is taken from experimental measurements.

Typical electrode parameters taken from the data used in Figs. 5.10 and 5.13 are $I_{e,sat} = 3.2$ A and $I_{i,sat} = 0.1$ A. The grounded limiter and chamber are assumed to collect higher currents due to their much bigger area. The perpendicular resistance that fits the experimental data is $R_{\perp} \sim 100 \Omega$. This value is in close agreement with the average resistance obtained from charge exchange drag, $R_{\perp}^{cx} = \rho_{\perp}^{cx} l / A \sim 170 \Omega$ where ρ_{\perp}^{cx} is the perpendicular resistivity, l is the thickness of the plasma between the electrode and the limiter, $l \sim 0.1$ m, and A is the area of the magnetic surface, $A \sim 1 \text{ m}^2$, all average quantities. The perpendicular resistivity is calculated in Section 2.3 and to the lowest order is $\rho_{\perp}^{cx} \sim B^2 / (M n \nu_{i,n}^{cx})$. This expression is derived from the balance between $\mathbf{J} \times \mathbf{B}$ and the neutral drag $M n \nu_{i,n}^{cx} V_E \hat{\theta}$ where M is the ion mass and $\nu_{i,n}^{cx} \sim 6 \cdot 10^4$ Hz is the charge exchange collisional frequency for a plasma with ion temperature $T_i = 2$ eV and neutral density $n_0 = 3 \cdot 10^{-18} \text{ m}^{-3}$ [23]. The solutions for the floating potentials and the current as function of the applied potential to the electrode are shown in Fig. 5.16.

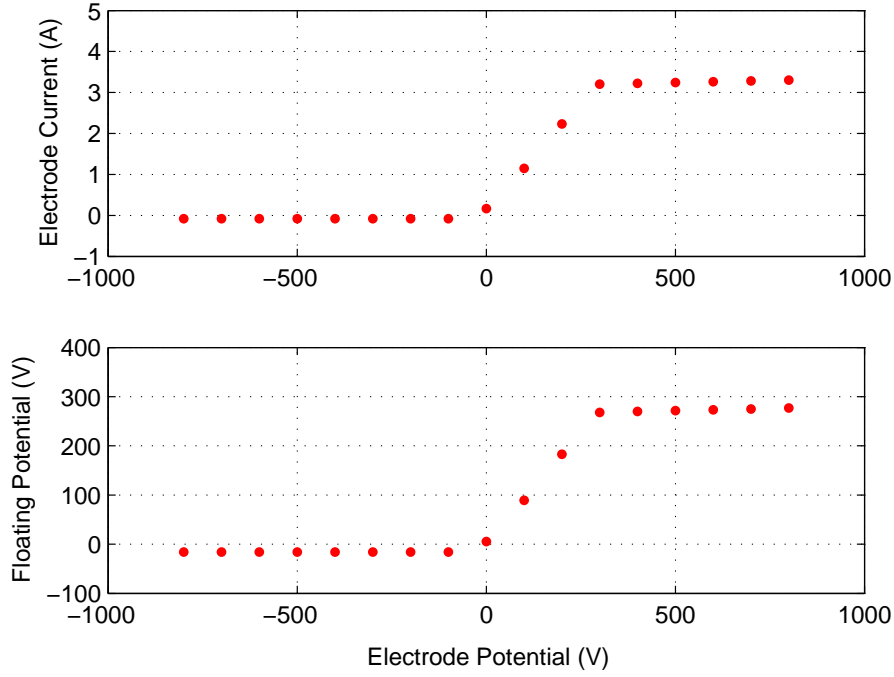


Figure 5.16: Asymmetry in current and floating potentials *vs.* applied electrode voltage described by the model.

We can solve the system of equations over the regions of experimental space. The solutions can be represented as operating points in both electrode/limiter sheath equation curves, and the bulk equation curve as shown in Fig. 5.17. As the electrode is positive biased with respect to ground (green circles), electrons are collected, the current rises, and a potential difference develops inside the bulk of the plasma due to $R_{\perp}I$ in Eq. (5.2). The potential drop at both sheaths is a couple of T_e , more as the current increases. The potential in the plasma follows the external bias as seen in Fig. 5.16. This

process can continue (yellow circle) until the current through the electrode reaches saturation $I_{sat,e}$ freezing the potential drop inside the plasma (orange circle), $\phi_{p,1} - \phi_{p,0} = R_{\perp} I_{sat,e}$. Any extra applied potential (red circles) drops at the electrode sheath, $\phi_1 - \phi_{p,1}$, with no extra penetration inside the plasma as shown in Fig. 5.16. A similar situation occurs as the electrode is negative biased (turquoise circles), however the maximum current is limited by $I_{sat,i}$ that is much smaller than $I_{sat,e}$. Then, the maximum potential difference inside the bulk of the plasma becomes $\phi_{p,1} - \phi_{p,0} = R_{\perp} I_{sat,i}$ (blue circles), reproducing the asymmetry seen in the data. Regarding the close correlation between the current and the plasma potential seen in Figs. 5.10 and 5.13 we can see that the current flowing through the system never reaches $I_{sat,e,i}$ on the limiter. Then its sheath potential drop is only a couple of T_e . That makes $\phi_{p,0}$ much smaller than the potentials applied and through Eq. (5.2), $\phi_{p,1} \sim R_{\perp} I$ as observed in the experimental data.

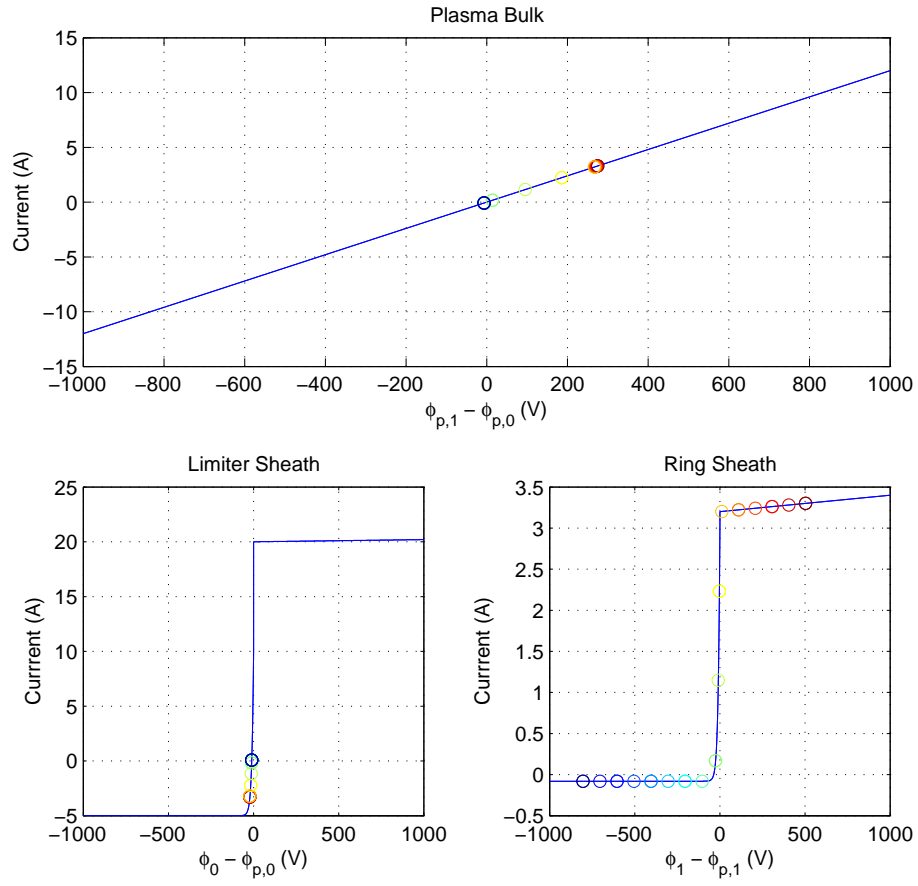


Figure 5.17: Operating points for different applied potentials to the electrode.

5.7 Potential at the Equatorial Plane and Centrifugal Confinement

In Section 5.5 we studied the penetration of the potential into the plasma near the magnetic field throat and consequently the electrode sheath potential drop. In this section we study the variation of the potential along the magnetic field lines from the throat into the equatorial plane. This can lead to clues if centrifugal confinement is achieved as predicted in Eq. (2.39) and 2-fluid effects are present as seen in Section 2.2.3. In order to study this effect, we compare the measurements obtained from the throat and equatorial floating probes described in Section 4.1.2.

Fig. 5.18 shows profiles for low voltages (< 200 V) and positive polarity applied to the ring (top) and plate (bottom) electrodes with neutral density .2 mTorr and a magnetic field at the center of the chamber of 0.065 T. The potentials measured with the throat floating probes are extrapolated to the equatorial plane following the magnetic field lines. The divergence of the lines as we move towards the equatorial plane is the reason for the increase in the extrapolated radial size of the throat probes and electrodes. The applied voltage penetrates into the plasma and from there into the bulk of the plasma at the equatorial plane.

Regardless of the potential sheath drop, at low voltages the magnetic field lines are equipotentials with an error of ± 10 V $\sim \pm 2 T_e$ (V). The overall speeds measured at the equatorial plane and throat are subsonic $\leq 2 \cdot 10^4$ m/s. At these speeds small centrifugal confining potential ~ 7 V are expected.

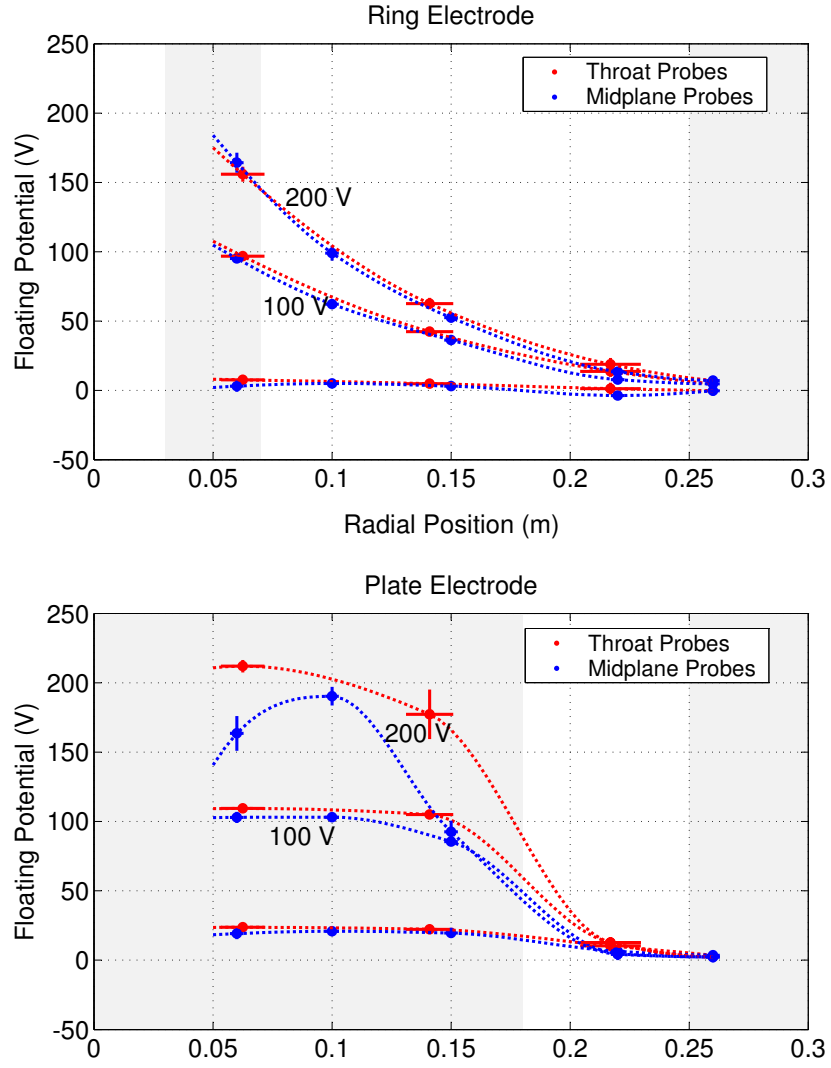


Figure 5.18: Floating potential for low biasing voltages (< 200 V) and positive polarity applied to the ring (top) and plate (bottom) electrode. The positions of the biased electrodes (gray), and the throat probes (red) are extrapolated to the midplane following the magnetic lines. For low voltages the biased magnetic lines are roughly equipotentials.

This situation changes when higher biasing potentials create faster rotational speeds. Fig. 5.19 shows typical profiles for high voltages (> 500 V) and positive polarity applied to the ring (top) and plate (bottom) electrodes. High penetration of the potential occurs with supersonic rotational speeds at the throat $\sim 4 \cdot 10^4$ m/s. The non biased magnetic lines behave as equipotentials with no centrifugal confinement seen within the errors. However, the biased magnetic lines present a potential drop from the throat to the equatorial plane of 400 V to 600 V. This drop is not associated with centrifugal confinement. As explained in Section 2.2.3 centrifugal confinement increases when moving from the throat to the equatorial plane (~ 60 V for the current conditions) which is opposite to what is observed. The potential drop along the lines limits the potential at the equatorial plane to 175 V and the overall speed of the plasma. This limitation of potential at the equatorial plane has been observed in most cases where those potentials are exceeded at the throat either using the ring or plate.

For negative bias voltages the sheath drop is large as shown in Section 5.5 and in the best case we find voltages of 100 V at the throat and equatorial plane with speeds of 10^4 m/s. The magnetic field lines behave as equipotentials within the experimental error as shown in Fig. 5.20.

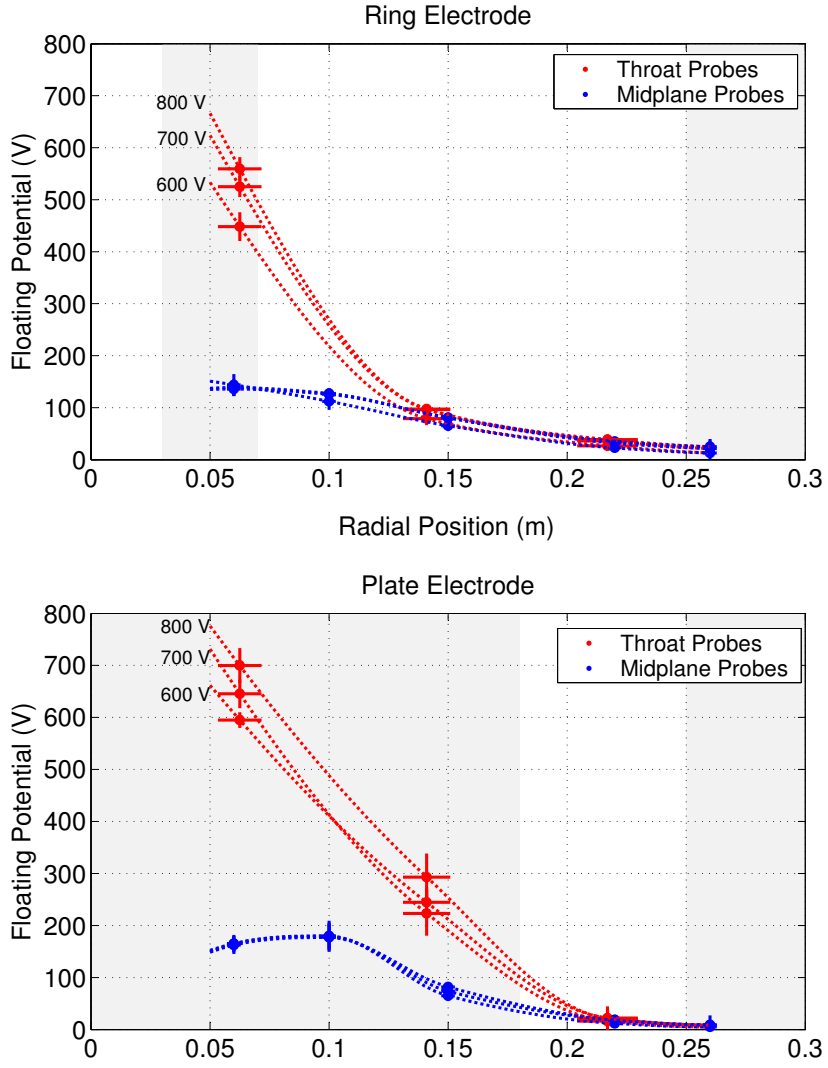


Figure 5.19: Floating potential for low biasing voltages (> 500 V) and positive polarity applied to the ring (top) and plate (bottom) electrode. The positions of the biased electrodes (gray), and the throat probes (red) are extrapolated to the midplane following the magnetic lines. For high voltages the biased magnetic lines are highly non equipotentials.

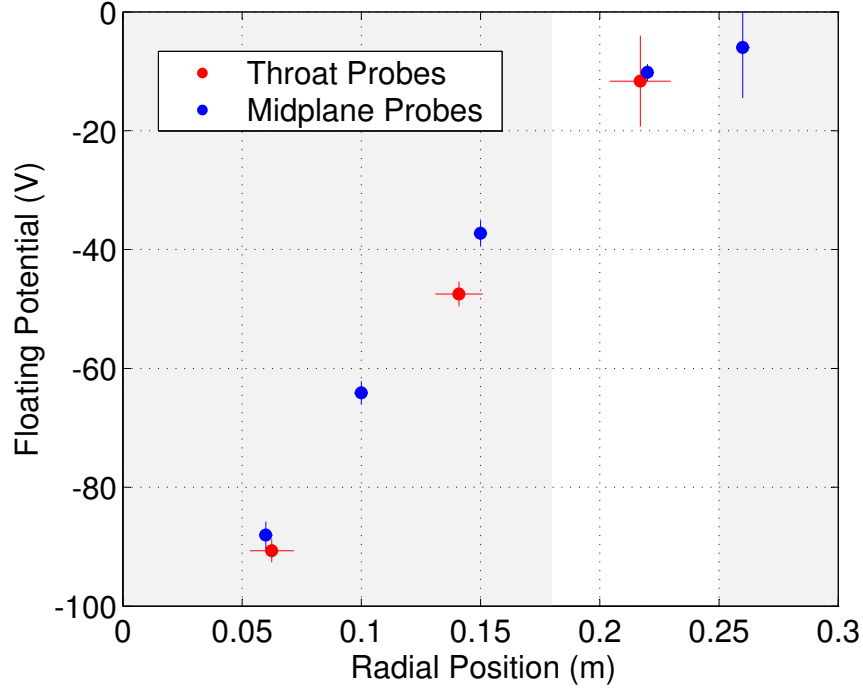


Figure 5.20: Floating potential for negative biasing voltages applied to the plate electrode. The position of the biased electrode (gray), and the throat probes (red) are extrapolated to the midplane following the magnetic lines. The biased magnetic lines are roughly equipotentials.

In summary, for potentials at the throat less than 200 V (including negative polarity) the magnetic field lines behave as equipotentials within the experimental error when connecting the throat and the equatorial plane in agreement with the small difference that would be obtained by centrifugal confinement. For higher biasing potentials the non biased magnetic lines remain equipotentials however the biased lines present a maximum in the potential

at the equatorial plane of ~ 200 V. Consequently when the penetration of the electrode potential into the throat is high, the biased magnetic lines present a drop in potential from the throat to the equatorial plane, $\sim 100 T_e(\text{V})$, that is opposite to what is expected in centrifugal confinement. This effect severely limits the rotation and shear flow obtained at the throat.

Different hypothesis have been considered to account for the drop in potential along the magnetic lines from the throat to the equatorial plane but non of them seem satisfactory.

- Instabilities: The plasma does not seem to present major instabilities that breaks the connection along the magnetic lines for frequencies lower than 25 kHz.
- High parallel resistivity: In order to have voltage drops of 500 V along the magnetic lines with currents on the order of 2 A, the parallel resistance of the magnetic shell should be at least 250Ω (corresponding to currents flowing along the lines and only flowing across at the equatorial plane). The electrode area is 20 cm^2 and the distance between the equatorial plane and the electrode is 50 cm. The parallel resistivity is $\rho \sim 1 \Omega\text{m}$. Then, the collisional frequency for the electrons should be $\nu_{col} = \rho e^2 n / m_e = 3 \cdot 10^8 \text{ Hz}$ that is 4 orders of magnitude higher than than the collisional frequency with neutrals or ions.
- Velocity cutoff: There could be enhancement of the perpendicular conductivity if the rotational speeds reached the velocity cutoff described

in Section 2.3. However, we have not measured these high speed values. It would be desirable to achieve higher rotational speeds with negative bias to rule out this hypothesis because the cutoff is not present in this polarity.

- Ionization: Speeds cannot exceed $5.5 \cdot 10^4$ m/s for hydrogen until full ionization of the plasma occurs (Section 5.8) [2]. This limit in speed would imply a limit in the potential at the equatorial plane. However, no increase in density has been observed.
- Sheath expansion: The high penetration at the throat could be due to sheath expansion. It would require an expansion of $0.1 \text{ m} \sim 600 \lambda_D$ to cover the distance from the electrodes to the throat probes. This is longer than predicted by usual theories [21, 25].
- Electron cyclotron resonance layer: The microwaves create a second resonance layer between the throat and the equatorial plane as described in Section 5.1. However, we do not have an explanation why the layer would affect the magnetic line connection only above 300 V.

In conclusion, the effect of non equipotential magnetic lines when they are biased has not been explained yet.

5.8 Ionization

Initially we generate the target plasma using microwaves. As shown in Section 5.1 the densities acquired are $\sim 10^{16}$ particles/m³ that causes the

system to be far away from magnetofluid states in parameter space (Section 2.2.1). As said in Section 3.4 it would be costly and difficult to achieve $5 \cdot 10^{18}$ particles/m³ using extra microwave power. Ionization using high voltage breakdown as in MCX has inconveniences. Our goal has been to increase the density using the rotation as the main ionizing mechanism. This method was discovered in early experiments [10] and analyzed [2]. Essentially, if a small degree ionized plasma is rotated and accelerated, the speed will increase with no ionization until it reaches the critical velocity where the energy of the ions is the same as the ionization potential of the neutral particles. A further increase in the input translates in more electrode currents that leads to an increase in ionization. Higher speeds can only occur after the plasma is fully ionized. In our experiment we believe we have reached this condition. Fig. 5.21 shows the floating potential profile (top) and the corresponding electric drift V_E (bottom) at the throat and equatorial plane for four different plate electrode potentials (500 V, 600 V, 700 V, 800 V) for a neutral pressure = 0.5 mTorr and coil current = 600A. The floating potentials and rotational velocities are extrapolated to the equatorial plane following the magnetic field lines. Fig. 2.9 shows that the speed is higher than V_E for a positive biased plasma due to the extra centrifugal force drift (Eq. (2.51)). In all the cases the maximum electric drifts at the throat (and at the equatorial plane for 700 V and 800 V) are above $5.5 \cdot 10^4$ m/s, however a large increase in density has not been observed and electrode currents remain low.

A different mechanism of ionization has to be considered to generate

higher densities. One choice considered is to add small plasma guns to the electrodes to generate a dense plasma in a small volume that will expand and fill up the chamber to be biased afterwards. Initial results for a single gun in a volume 0.005 m^3 show densities of $5 \cdot 10^{19} \text{ particles/m}^3$ [41]. Four of these guns would be necessary to reach the desired density in the chamber. This method will also allow shaping of the initial density profile.

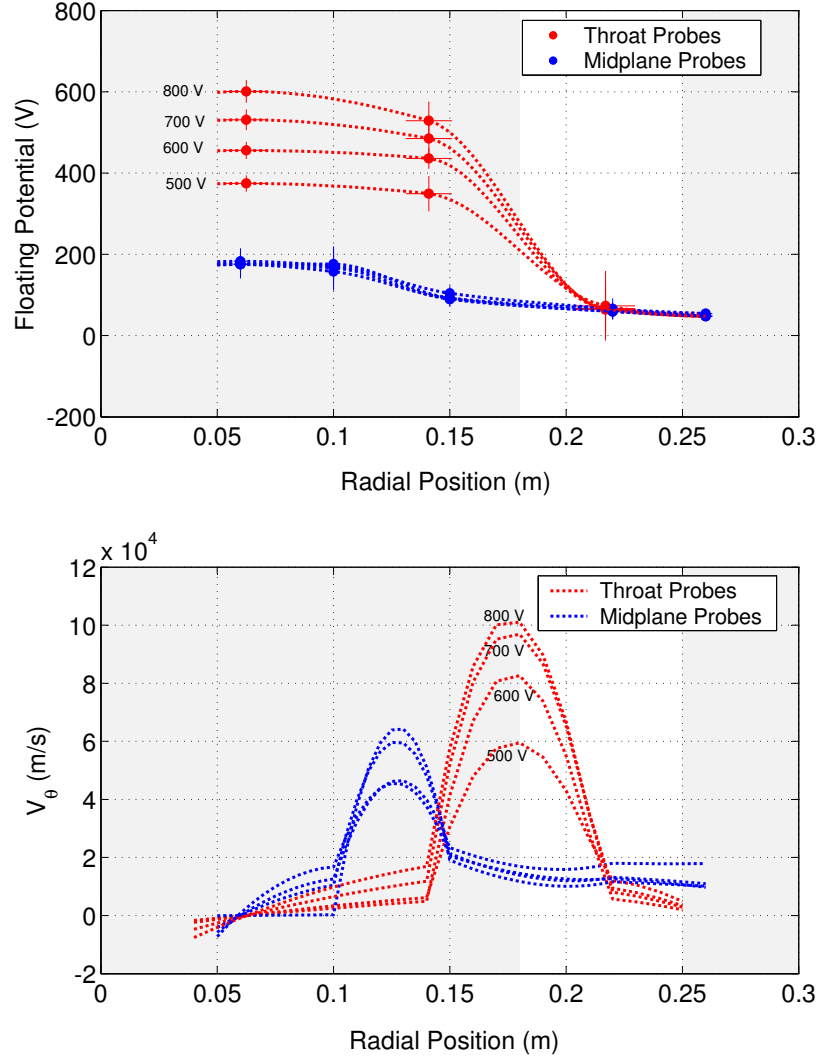


Figure 5.21: Floating potential profile (top) and the corresponding electric drift V_E (bottom) for four different plate electrode potentials (500 V, 600 V, 700 V, 800 V). The floating potentials, rotational velocities at the throat and biased electrode position are extrapolated to the equatorial plane following the magnetic field lines. The critical speed for hydrogen is reached but no extra ionization is observed.

Chapter 6

Summary

The goal of this dissertation has been twofold: 1) to generate supersonic rotating plasmas in order to take the first steps in the proposed path to create magnetofluid states in the lab, and 2) to contribute to the theoretical understanding of 2-fluid effects in rotating plasmas in connection with magnetofluid states. After constructing the basic experiment (a rotating plasma in a mirror magnetic field), we added different probes to diagnose the rotating plasma, installed a data acquisition system based on Labview software and set up an MDSplus archive system that can be accessed worldwide. The main results of this investigation are:

- We generated a low density supersonic rotating plasma after optimizing the electrode design required to maximize current collection area to achieve high penetration of the external applied potential. Alfvénic flows needed for a transition to magnetofluid states could not be reached because the initial plasma density was too low.
- Asymmetry in the current and the potential penetration with the polarity of the external bias follows an $I - V$ characteristic curve of a Langmuir probe but with modifications. This effect leads to constraints

in the rotational speed with the polarity as well as a partial control of the potential profile and shear flow. We presented a model to account for this asymmetry.

- At low bias low rotational speeds agree with the expected $\mathbf{E} \times \mathbf{B} / B^2$ while magnetic field lines behave as equipotential lines within the experimental error in agreement with the expected small centrifugal effects. For biased magnetic lines and supersonic speeds there are potential drops along the lines as high as 100 times the electron temperature; such large drops are opposite to the predictions of the theoretical model and centrifugal confinement. This effect limits considerably the plasma speed at the equatorial plane and it is still under investigation.
- Under certain conditions the plasma is bistable (for the same external conditions the system can be found in two or more states) in both AC and DC bias. The bistability reacts nonlinearly with control parameters of electron density and biasing.
- The collected data suggests that critical speeds for extra ionization were reached at the throat of the mirror magnetic field. However, no increase in density was observed. An alternative method is presented to increase the density in order to move to future conditions suitable for magnetofluid states.
- We found a region in parameter space where 2-fluid effects are important and magnetofluid states can exist. This led to the selection of a set of

parameters where MBX should run.

- We presented an analytic solution (rigid rotation) to a 2-fluid system for a rotating plasma embedded in an external magnetic field. This solution differs appreciably, due to the finite ϵ , from ideal MHD predictions. The new features involve a high increase in the plasma potential from the throats of the mirror magnetic field to the equatorial plane (of the order of the biasing potential applied externally to the system). This effect creates high asymmetry with respect to the polarity of the potential, high centrifugal confinement, and rotational speeds that differ from the usual electric drift. As the rotation reaches Alfvénic speeds the currents generated in the system create a self magnetic field that becomes comparable to the external magnetic field that can ultimately lead to a reconnection process and possibly the magnetofluid states.
- The inclusion of dissipative terms allowed us to compare the present experimental requirements for driving the system with the theory; it also helped us to calculate the requirements for the future conditions where MBX will operate.

The results in this dissertation show that supersonic low density plasma can be achieved which is the first step towards the quest of magnetofluid states. The next step is to reach the conditions for magnetofluid states to exist that implies an increase in density of ~ 500 compared to our present conditions. Considering that the density did not increase with plasma rotation

we propose the use of small plasma guns to generate the desired densities. Initial results show that 5 of these devices would be enough. This increase in density, according to our results, will increase the electrode currents and the potential penetration of the negative biasing potential. This polarity is desired at higher speeds because there is no velocity cutoff. Installation of magnetic and Rogowski probes could provide information on diamagnetic currents and reconnection. An interferometer would help to study centrifugal confinement measuring the densities at the throat and equatorial plane.

Bibliography

- [1] G. F. Abdrashitov, A. V. Beloborodov, V. I. Volosov, V. V. Kubarev, Yu. S. Popov, and Yu. N. Yudin. Hot rotating plasma in the psp-2 experiment. *Nucl. Fusion*, 31(7):1275, 1991.
- [2] H. Alfvén. Collision between a nonionized gas and a magnetized plasma. *Revs. Modern Phys.*, 32(4):710, 1960.
- [3] Oscar Anderson, William R. Baker, Alexander Bratenahl, Harold P. Furth, and Wulf B. Kunkel. Hydromagnetic capacitor. *J. Appl. Phys.*, 30(2):188, 1959.
- [4] Roger D. Bengtson, P. M. Valanju, S. M. Mahajan, R. D. Hazeltine, R. Chatterjee, H. J. Quevedo, and Evangelos Meintanis. An experiment to study sheared magnetofluids and bernoulli confinement. *Bull. Am. Phys. Soc.*, 45:7351, 2000.
- [5] S. I. Braginskii. *Transport processes in a plasma*, volume 1 of *Reviews of Plasma Physics*, page 205. Consultants Bureau, New York, 1965.
- [6] S. Chandrasekhar and P. C. Kendall. On force-free magnetic fields. *Astrophys. J.*, 126:457, 1957.

- [7] R. F. Ellis, A. Case, R. Elton, J. Ghosh, H. Griem, A. Hassam, R. Lunsford, S. Messer, and C. Teodorescu. Steady supersonically rotating plasmas in the maryland centrifugal experiment. *Phys. Plasmas*, 12:055704, 2005.
- [8] R. F. Ellis, A. B. Hassam, S. Messer, and B. R. Osborn. An experiment to test centrifugal confinement for fusion. *Phys. Plasmas*, 8(5):2057, 2001.
- [9] K. Boyer et al. Theoretical and experimental discussion of ixion, a possible thermonuclear device. In *Proceedings of the Second International Conference on the Peaceful Uses of Atomic Energy*, volume 31, page 319, New York, 1958. United Nations.
- [10] Ulf V. Fahlson. Experiments with plasma moving through neutral gas. *Phys. Fluids*, 4(1):123, 1961.
- [11] T. A. Flaim and P. D. Ownby. Observations on bayard-alpert ion gauge sensitivities to various gases. *J. Vac. Sci. Technol.*, 8(5):661, 1971.
- [12] J. Ghosh, R. Elton, H. Griem, C. Teodorescu, A. Case, and R. Ellis. Vacuum ultraviolet measurements on hydrogen resonance lines in the maryland centrifugal experiment. *Phys. Plasmas*, 12:034501, 2005.
- [13] J. P. Gunn, C. Boucher, P. Ďevynck, I. Duran, K. Dyabilin, J. Horaček, M. Hron, J. Stöckel, G. Van Oost, H. Van Goubergen, and F. Žáček. Edge flow measurements with gundestrup probes. *Phys. Plasmas*, 8(5):1995, 2001.

- [14] A. B. Hassam. Nonlinear stabilization of the rayleigh-taylor instability by external velocity shear. *Phys. Fluids B*, 4(3):485, 1992.
- [15] A. B. Hassam. Velocity shear stabilization of interchange modes in elongated plasma configurations. *Phys. Plasmas*, 6(10):3772, 1999.
- [16] R. D. Hazeltine, S. M. Mahajan, H. Quevedo, and P. M. Valanju. Equilibrium of a rotating mirror plasma - i. In *International Sherwood Fusion Theory Conference*, 2003.
- [17] Richard D. Hazeltine and François L. Waelbroeck. *The framework of plasma physics*. Perseus Books, 1st edition, 1998.
- [18] Rainer H. Hörlein. Characterization of bistable states in rotating mbx mirror plasmas. Master's thesis, The University of Texas at Austin, 2004.
- [19] Paul Horowitz and Winfield Hill. *The Art of Electronics*. Cambridge University Press, 2nd edition, 1989.
- [20] I. H. Hutchinson. Ion collection by a sphere in a flowing plasma: I. quasineutral. *Plasma Phys. Control. Fusion*, 44:1953, 2002.
- [21] I. H. Hutchinson. *Principles of Plasma Diagnostics*. Cambridge University Press, 2nd edition, 2002.
- [22] John David Jackson. *Classical Electrodynamics*. John Wiley & Sons, Inc., New York, 3rd edition, 1999.

- [23] R. K. Janev, W. D. Langer, K. Jr. Evans, and D. E. Post. *Elementary Processes in Hydrogen-Helium Plasmas: Cross Sections and Reaction Rate Coefficients*. Springer Verlag, 1987.
- [24] B. Lehnert. Rotating plasmas. *Nucl. Fusion*, 11:485, 1971.
- [25] Michael A. Lieberman and Alan J. Lichtenberg. *Principles of Plasma Discharges and Materials Processing*. John Wiley & Sons, Inc., New York, 1st edition, 1994.
- [26] S. M. Mahajan, R. Miklaszewski, K. I. Nikol'skaya, and N. L. Shatashvili. Formation and primary heating of the solar corona: Theory and simulation. *Phys. Plasmas*, 8(4):1340, 2001.
- [27] S. M. Mahajan and Z. Yoshida. Double curl beltrami flow: Diamagnetic structures. *Phys. Rev. Lett.*, 81(22):4863, 1998.
- [28] S. M. Mahajan and Z. Yoshida. A collisionless self-organizing model for the high-confinement (h-mode) boundary layer. *Phys. Plasmas*, 7(2):635, 2000.
- [29] Kenro Miyamoto. *Plasma Physics for Nuclear Fusion*. The MIT Press, 1980.
- [30] F. Paschen. *Wied. Ann.*, 37:69, 1889.
- [31] David M. Pozar. *Microwaves Engineering*. John Wiley & Sons, Inc., New York, 3rd edition, 2004.

- [32] H. J. Quevedo, Roger Bengtson, S. M. Mahajan, and P. M. Valanju. Sheared magnetofluids and bernoulli confinement. *Bull. Am. Phys. Soc.*, 46(8):276, 2001.
- [33] H. J. Quevedo, R. H. Hörlein, P. M. Valanju, and R. D. Bengtson. Study of the effects of high voltage potential applied to magneto bernoulli experiment (mbx). *Bull. Am. Phys. Soc.*, 49(8):170, 2004.
- [34] H. J. Quevedo, P. M. Valanju, and R. D. Bengtson. Asymmetry, potential penetration and supersonic speeds in mbx experiment at high voltage and medium power. Accepted in J. Fusion Energy, April 2006.
- [35] H. J. Quevedo, P. M. Valanju, and R. D. Bengtson. Centrifugal confinement in magneto bernoulli experiment (mbx). *Bull. Am. Phys. Soc.*, 48(7):122, 2003.
- [36] H. J. Quevedo, P. M. Valanju, and Roger D. Bengtson. Initial results of magneto-bernoulli experiment. *Bull. Am. Phys. Soc.*, 47(9):67, 2002.
- [37] C. J. Schrijver, A. M. Title, T. E. Berger, L. Fletcher, N. E. Hurlburt, R. W. Nightingale, R. A. Shine, T. D. Tarbell, J. Wolfson, L. Golub, J. A. Bookbinder, E. E. DeLuca, R. A. McMullen, H. P. Warren, C. C. Kankelborg, B. N. Handy, and B. De Pontieu. A new view of the solar outer atmosphere by the transition region and coronal explorer. *Solar Phys.*, 187(2):261, 1999.

- [38] Shunjiro Shinohara, Norikazu Matsuoka, and Toshiro Yoshinaka. Profile control and plasma rotation by biased electrodes in large diameter rf produced plasma. *Jpn. J. Appl. Phys.*, 38:4321, 1999.
- [39] William R. Smythe. *Static and Dynamic Electricity*. John Benjamins Publishing Co, 3rd edition, 1989.
- [40] Thomas Howard Stix. *Waves in Plasmas*. Springer-Verlag New York, Inc., 1992.
- [41] Harish Subbaraman. The design and construction of a high density plasma source. Master's thesis, The University of Texas at Austin, 2006.
- [42] J. B. Taylor. Relaxation of toroidal plasma and generation of reverse magnetic fields. *Phys. Rev. Lett.*, 33(19):1139, 1974.
- [43] J. B. Taylor. Relaxation and magnetic reconnection in plasmas. *Rev. Mod. Phys.*, 58(3):741, 1986.
- [44] P. M. Valanju, H. J. Quevedo, and S. M. Mahajan. Equilibrium, multistability, and chiral asymmetry in rotated mirror plasma. Accepted in *Phys. Plasmas*, June 2006.
- [45] F. Wagner and et. al. Regime of improved confinement and high beta in neutral-beam-heated divertor discharges of the asdex tokamak. *Phys. Rev. Lett.*, 49(19):1408, 1982.

- [46] L. Woltjer. A theorem of force-free magnetic fields. In *Proc. Natl. Acad. Sci. U.S.A.*, volume 44, page 489, 1958.
- [47] Z. Yoshida and S. M. Mahajan. Variational principles and self-organization in two-fluid plasmas. *Phys. Rev. Lett.*, 88(9):095001, 2002.
- [48] Z. Yoshida, S. M. Mahajan, and S. Ohsaki. Scale hierarchy created in plasma flow. *Phys. Plasmas*, 11(7):3660–3664, 2004.

Vita

Hernan Javier Quevedo was born in Buenos Aires, Argentina on July 15, 1972, the son of Miguel F. Quevedo and Susana I. Torandell Quevedo. He received the Licenciatura in Fisica from the Universidad de Buenos Aires in 1999. In the fall of that year, Hernan started graduate studies in The University of Texas at Austin. In the following year, Hernan joined Dr. Roger Bengtson, Dr. Prashant Valanju and Dr. Swadesh Mahajan and started working in the Magneto Bernoulli eXperiment.

Permanent address: 11901 Hobby Horse Ct. Apt. 1633
Austin, Texas 78758

This dissertation was typeset with L^AT_EX[†] by the author.

[†]L^AT_EX is a document preparation system developed by Leslie Lamport as a special version of Donald Knuth's T_EX Program.